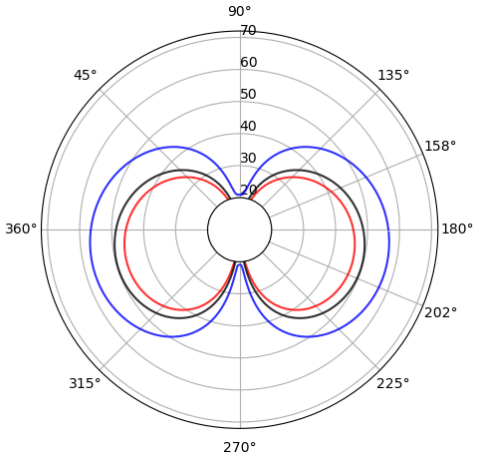

Urban Air Vehicle implementation and limitation

Development of a new acoustic tool for the noise prediction

Gabriele Bossotto

Thesis to obtain the Master of Science Degree in

Aerospace Engineering

Supervisors: Prof. Fernando José Parracho Lau
Prof. Frederico José Prata Rente Reis Afonso

Examination Committee

Chairperson: Prof. Filipe Szolnoky Ramos Pinto Cunha
Supervisor: Prof. Fernando José Parracho Lau
Member of the Committee: Prof. Pedro Da Graça Tavares Álvares Serrão

November 2021

”The important thing
is to never stop
questioning.”

Albert Einstein

Acknowledgments

First of all i want to thank my family for supporting me along all these years of studying and for having believed in me without hesitation, even in the difficult moments, specially in these moments i would say, they helped me in all my decisions and doubts, making me to keep going. I would like to thank Silvia for supporting me in this last year of Erasmus that gave me the possibility to live a wonderful experience in a beautiful country, helping me in a personal and academic growth.

I would like to thank my thesis supervisors professors Fernando Lau and Frederico José Prata Rente Reis Afonso for all their teachings and guidance throughout the development of this thesis.

Abstract

This work presents the prediction and the optimization study of noise produced by rotors of a new concept of transport: UAV (Urban Air Vehicle). This project of UAM (Urban Air Mobility) evolved in the recent years due to the overcrowding of the cities' roads; this is a solution that at the same time brought up to light different issues and one of these, main theme of this document, is the noise pollution. However, the ability to rapidly assess the performance of these new generation of vertical lift vehicles, with sufficient fidelity, is a current weakness of this nascent industry. For this reason, the intention of this study is the prediction of the noise produced by the rotor itself, the study of minimization and optimization of the noise sources. For this purpose, is adopted an open-source suite of mixed-fidelity aerodynamics and aeroacoustics (FLOWUnsteady) simulations. This latter is able to fully characterize induced velocities across the stable region flow, where blade element momentum theory (BEMT) operates. This method is coupled with an aeroacoustics solver for tonal (FW-H code PSU WOP-WOP based on Farassat 1-A formulation) and broadband noise predictions (Brooks, Pope, and Marcolini (BPM) equations). To validate the data produced through this simulation and prediction program the thesis is divided in into a computational and an experimental part. In the first part wings, body and rotating blades are modelled through a combination of panel, vortex lattice, lifting line, and blade elements. Meanwhile, the second part is the analysis of the same model elaborated by the software in an anechoic chamber, in order to validate the data. This comparison allowed to confirm the high fidelity of the computational method adopted and affirm the studied noise optimization method with the objective to guarantee the use of this new concept of transport in the classic city routine.

Keywords: UAM, Rotor noise, Noise prediction, Noise optimization

Contents

List of Tables

List of Figures

Nomenclature

Greek symbols

α	Angle of attack.
β	Angle of side-slip.
$\delta(f)$	Dirac delta function.
δ_{ij}	Kronecker delta.
Γ_n	Vortex filament strength.
κ	Thermal conductivity coefficient.
μ	Molecular viscosity coefficient.
$\nabla\cdot$	Divergence.
$\nabla\times$	Rotational.
ω	Angular velocity.
Φ	Inflow angle.
ρ	Density.
σ	Solidity factor.
τ	Vector of external torques.
τ_e	Emission time.

Roman symbols

C_D	Coefficient of drag.
C_L	Coefficient of lift.
C_M	Coefficient of moment.
C_n	Coefficient of local normal force.
C_T	Coefficient of thrust.

C_t	Coefficient of local tangential force.
dM	Elemental Torque.
dT	Elemental Thrust.
M	Torque.
T	Thrust.
$\bar{T_{ij}}$	Lighthill's stress tensor.
$\Box$	D'Alembert operator.
$\vec{G_{m,n}}$	Influence coefficient.
a	Axial induction factor.
a'	Angular induction factor.
B	Number of blades.
d	Local drag force.
F_D	Linear friction.
f_c	Center frequency.
f_{HL}	High frequency limit.
f_{LL}	Low frequency limit.
g	Gravity acceleration.
$H(f)$	Heaviside function.
I	Inertia matrix.
l	Local lift force.
p	Pressure.
p'	Acoustic pressure.
p'_L	Loading pressure.
p'_T	Thickness pressure.
p_N	Local normal force.
p_T	Local tangential force.
p_{ij}	Compression stress tensor.
R	Rotation matrix.

St Strouhal number.

V Induced velocity.

$\mathbf{u}$ Velocity vector.

$\hat{i}, \hat{j}, \hat{k}$ Cartesian axis indices.

M Mach number.

r_e Emission distance between source and observer.

u, v, w Velocity Cartesian components.

y_e Emission position.

Subscripts

$\infty, 0$ Free-stream condition.

i, j, k Computational indexes.

max Maximum value.

n Normal component.

ret Retarded time.

x, y, z Cartesian components.

ref Reference condition.

Superscripts

* Adjoint.

ˆ Vector.

T Transpose.

Chapter 1

Introduction

Airbus and other companies have declared that by 2030, 60 % of the world's population will be urban [1]. In fact, the recent significant population growth is expected to create a real need for innovative mobility options as ground infrastructure becomes increasingly congested. The solution that leverages the airspace above cities could be safe, sustainable and convenient. For this reason, the classical way of transport, especially in the congested urban areas, need to be substituted through the development of new and innovative technologies, such as Urban Air Vehicles (UAV). This latter are intended to be safe and efficient automated aircraft that will operate and transport passengers or cargo at lower altitudes within urban and suburban areas. The history can indeed testify that since the birth of the first commercial helicopter air transportation company in 1953, that carried passenger to and from New York City's three major airports, there was an accelerate increasing of needs of this innovation for the common use. For this reason, these companies, which provided connecting services between major airports or between airports and nearby city centers, saw an exponential increase of operations in few years: from under 155,000 annual helicopter passengers in 1957 to over 1.2 million passengers in 1967 [2]. Following in figure 1.1, it is possible to observe the concept of Urban Air Mobility (UAM) operations in 70's.

Figure 1.1: New York Airways, circa 1977, from https://thepointsguy.com/news/when-helicopters-landed-on-manhattan-skyscrapers-all-the-time/

UAM is composed of an ecosystem that considers the evolution and safety of the aircraft, the framework for operation, access to airspace, infrastructure development and community engagement.

This initial increase of the amount of passengers and incredible success of helicopter airlines was interrupted due to safety issues and economic challenges, most of them were forced to reduce or terminate services [2]. But the Government interest in military applications of Vertical Take-Off and Landing (VTOL) aircraft and airline interest in sub-regional air transportation rekindled the development that was interrupted in the 1970s. In few years, from studies conducted in the 1980s and 1990s , the tiltrotor aircraft was proposed for civil purpose as an alternative to the helicopter that benefitted from higher cruise speeds and longer range [3]. This envelope leads to the drafting of a circular by Federal Aviation Administration (FAA) in 1991 specifically for vertiport design, with dedicated locations in the city for take-off and landing of a VTOL aircraft. In figure 1.2 a future concept of vertiport is presented.

Figure 1.2: Future concept of vertiport, from https://www.cndenglish.com/others/travel-technology/embraer-comes-urban-air-mobility-unit

Unfortunately, the creation of new infrastructure was perceived as a critical scaling requirement for CTR and, for this reason, the project did not emerge to provide passenger services. Meanwhile, numerous helicopter charter companies operated at various scales around the U.S. and the world. In parallel to the development of CTR aircraft and operations, NASA pursued the development of a small aircraft transportation system (SATS) from 2000 to 2005 that aimed to provide people a service of transport on-demand, anywhere and anytime for both personal and business travel [4]. Due to the 2008 financial crisis this project was ceased, but, anyway, a variety of commuter airlines thrived in the U.S offering private or ride-sharing helicopter charter operations [3]. In addiction to this emerging innovation, at the beginning of 2010 NASA presented a vision for an ”On-Demand Mobility” (ODM) system that relied upon small, electric aircraft and autonomy to conduct UAM operations in proximity to a metropolitan area [3].

Moreover, in the same way, also in Europe there was a large development of this new technology, that led to the birth of several projects for the urban ODM: in Germany the Lilium prototype was created by a startup based in Munich, the first all-electric jet, which is a five-seater air taxi that may connect Manhattan and Kennedy International Airport in just 10 minutes [5]. In figure 1.3a is possible to observe this new model of air taxi.
Other companies, based in Germany, are working to make short-distance air travel a reality in the coming years, and the Volocopter startup was the first one to get the ‘Design Organisation Approval’ from the

(a) Lilium prototype

(b) VoloCity prototype

Figure 1.3: Lilium prototype from https://www.theextravagant.com/lifestyle/tech/future-electric-lilium/ on the left and VoloCity prototype from https://www.businessinsider.nl/volocopter-vliegende-taxi/ on the right

European Aviation Safety Authority (EASA). Its concept is called VoloCity, which is its fouth-generation eVTOL (electric Vertical Take-off and Landing) aircraft. This vehicle has 18 rotors and can ferry two passengers as shown in figure 1.3b [5]. Meanwhile, Airbus is involved in the development of two electric UAM vehicles to provide short-haul flights across major cities that are congested and for commutes between suburbs and city centres at a more competitive price than road transport [5]. In fact, Airbus developed its first autonomous eVTOL aircraft called Vahana, illustrated in figure 1.4a. This self-piloted air taxi is thought to ferry a single passenger in a forward-facing cockpit. The company is working on a second aerial taxi called CityAirbus, which is under testing. This latter project is an all-electric multicopter eVTOL vehicle with four seats [6]. In figure 1.4b, it is possible to see a prototype of this VTOL aircraft.

(a) Vahana prototype

(b) Airbus Urban Air Vehicle

Figure 1.4: On the left the Vahana prototype from https://www.airbus.com/newsroom/stories/vahana-marks-a-major-milestone-with-successful-full-transition-flight.html, on the right Airbus Urban Air Vehicle from [1]

This emerging concept of an air taxis will provide on-demand transportation for individual needs. They will give the opportunity to connect important transportation nodes, such as airports and city centers, as well as providing quick transfers between train stations or a convenient option for crossing water basins. Like aforementioned, it is envisaged that air taxis will operate between dedicated locations in the city, called ”Vertiports” (or droneports or skyports). A typical approach for aviation administrations is to bundle such routes in corridors to keep air taxi traffic separated from other airspace users [7]. However, following this vision, the noise problem will not only exist in the vicinity of vertiports, where vehicles take-off and land, but also for citizens living or working below these corridors, which will be at an altitude between 500 and 1500 feet [8]. The Horizon 2020 research program on smart, green and integrated

transport identified two key criteria to achieve sustainable UAM: decreasing the overall environmental footprint, and controlling the noise and visual pollution [9]. These objectives have not yet been reached, but it is reasonable to think that these aims will be satisfied, approximately, around 2030 [9].

In figure 1.5 is possible to compare the distance traveled by a car and by an innovative UAV in the city of Paris for the same travel time and perceive the advantages that are related to the use this new concept of transport.

Figure 1.5: In the time it takes to drive 20 km in a congested city, you could fly 150 km in an air taxi, [10]

An electric VTOL air taxi could transport passengers from Charles de Gaulle Airport in Paris to Orleans, 160 kilometers by road or 133 km by air, in about 35 minutes instead of the two hours it takes by car today. [10]

1.1 Motivation

Noise generated by UAM has been identified as a critical factor in its development. Even though initial reactions among residents to well-controlled urban flight trials have been neutral or even positive [11], opposition to the full-scale onset of UAM is likely to occur once several thousand flights daily take place in a single city.

Nevertheless, in a field study conducted in September 2019, when the first air taxi flight took place in an European city, the participants in this study (N=1203) could not just see or hear the volocopter flying, but these participants also took a seat in the volocoptor on ground to get familiar with this new type of mobility service. When asked whether they would use the air taxi in autonomous flight, 37.9% answered “most likely” and another 28.9% “likely”, which adds up to 67% overall acceptance [8]. However, among all concerns, those related to noise are the ones deemed more concerning by the participants, who showed the least acceptance. For this reason, it is reasonable to think this type of innovative transport could only be accepted and used by most of the world population if acceptable values of noise pollution are provided. In 2004 the International Civil Aviation Organization (ICAO) came up with a document outlining a balanced approach [12], which aims to limit or reduce the number of people affected by significant aircraft noise. Noise limitations for aircraft operated close to people were announced: “To provide citizens with high level of environmental protection, it is necessary to limit the noise emissions to the greatest possible extent”.

1.2 State-of-the-art

Aircraft noise prediction methods are still developing, and the developers have made progress in different directions, leading in several tools. Noise prediction methods are subdivided into two broad groups: best practice methods and theoretical methods. Best practice methods rely mostly on measurement databases. On the other hand, theoretical methods rely on physical models to calculate the noise production and propagation [13]. Best practice methods are geared towards providing fast estimates of the noise impact from aircraft operations in an airport and its surroundings over long time frames. These tools are used by national authorities to predict noise contours in their jurisdictions and there are many variations. AEDT (Aviation Environmental Design Tool) is one of the most used and has been continuously improved for decades serving as a base for many other solutions [13]. Since the long-term noise impacts are outside the scope of this work are mainly discussed the theoretical methods. Around the end of 60's were done several advances in rotor noise prediction, thanks to the publication of the paper "Sound Generation by Turbulence and Surfaces in Arbitrary Motion" by Ffowcs Williams and Hawkings [14], based on the Lighthill's acoustic analogy approach [15], that was generalized to include effects of general types of surfaces and motions. In this paper, the Navier-Stokes's equation was rearranged, by Ffowcs Williams and Hawkings, into the form of an inhomogeneous wave equation with a monopole and dipole sources on the body surface and a quadrupole sources in the volume surrounding the body, known as FW-H equation. FW-H equation is particularly fit for applications in aeroacoustics since the three sources' terms are independent and can be computed separately. A decade later, thanks to the efforts driven by the Federal Aviation Administration (FAA) and NASA [16, 17] to predict noise for single fly-over events, was developed the first computer code ANOPP (or NASA Langley's noise prediction program). In this computer program, the aircraft flight dynamics is integrated with semi-empirical models for noise propagation and generation for individual sources, like fan, compressor, jet, wing, landing gear, and so on [18–21]. By the 1980s, US helicopter industry was forced to project fewer annoying helicopters since the introduction of the first noise regulations. With this purpose the four major US helicopter manufactures cooperated with NASA in the NASA/AHS Rotorcraft Noise Reduction Program. Simultaneously, several acoustic tests were conducted in the German-Dutch wind tunnel DNW (Duits-Nederslandse Windtunnel) [22]. Both programs led to several advances in rotor noise prediction, mostly concentrated on rotor noise in steady flight. In the last decade of 20^{th} century several codes were implemented thanks to the development of computational fluids dynamics (CFD): Brentner developed a new code of rotor noise prediction that contributed to great advances in this area, thanks to the arise of the Farassat's Formulation 1 and 1A [23, 24] and the progress in the computational capability; this code was the precursor of several other numerical algorithms [25–27]. In fact, in those years some upgrades have been applied to the ANOPP code leading to a second-generation model, ANOPP2, which partly uses computationally intensive higher fidelity methods [28]. At the same time, the improvement of computer power allowed the development of more accurate and sophisticated noise prediction tools. In fact, in addiction to the tools for existing aircraft, there was a need for high fidelity noise models within a multidisciplinary framework of designing unconventional conceptual aircraft. One objective for such

effort is to design aircraft with radical noise reductions, particularly the airframe noise. This approach was undertaken by the Silent Aircraft Initiative (SAI). The project aimed at making aircraft noise inaudible outside a typical airport perimeter [29, 30]. Other software tools have also been developed by NASA such as Advanced Subsonic and Supersonic Propeller Induced Noise prediction program (ASSPIN), focused on propeller noise, which is based on Farassat's formulations [31], and MUTE [32], that is a cutting-edge methodology with the objective to predict in detail the rotorcraft noise at the expense of great computational resources. Moreover, it is also possible to mention the development of an aircraft noise computer program FLIGHT, at the University of Manchester [33, 34]. It contains an acoustics branch where the acoustics emissions rely mostly on source modelling. However, the tool possesses several extra features such as shielding effects (by jets and, in a simplified way, by the fuselage), noise contours around airports and wind effects per example. This tool has been used for instance to study the impact of modified landing procedures [35].

1.3 Objectives and Deliverables

The development of this new type of transportation is being impelled by the objective of reducing the congestion in urban areas, among other advantages, but at the same time there are some disadvantages that must be addressed before UAM market enters in service, such as footprint, pollution and noise. This latter, as discussed before, is one of the most important reasons for people rejecting UAM. For this reason, an accurate prediction of the level of generated noise is of utmost importance. The rotor noise is one of the most annoying sources of noise in the UAV and its prediction is a complex and computationally demanding task. Therefore, the present work aims at developing a methodology for the noise prediction that addresses the following characteristics:

1. Accurately measures the thickness and loading noise generated by the rotors at any microphone position(s);
2. Predicts the noise generation in steady flight and maneuvering flight;
3. Is prepared to analyze different configurations: the user can choose the number of desired rotors and blades, as well as the hinge position of each blade;
4. Returns outputs in a format which allows the user to understand what happened during the simulation in terms of noise generation;
5. Finds a configuration of rotors and airfoils that minimize the noise pollution using an optimization tool;
6. Returns the advantages obtained adopting the optimized configurations instead of the original ones.

The main contribution of this work, compared to others, is the use of a new open-source of mixed-fidelity aerodynamics and aeroacoustics (FLOWUnsteady) simulations with its flexibility and low computational cost. In fact, the noise prediction can be performed to several vehicle configurations and flight

conditions, moreover, the use of solvers for tonal (PSU-WOPWOP also called PSW) and broadband (BPM) noise allow to reach a complete prediction of the noise produced. The new code will be validated through the comparison with experimental values in order to ensure the reliability of the results.

1.4 Thesis Outline

This project of thesis will follow the following structure:

- *Chapter 1*: Introduction to the aerodynamic noise problem and work developed in this thesis;
- *Chapter 2*: Overview of the theory to the base of the noise prediction and main equations used;
- *Chapter 3*: Structure of the software used for the prediction and user approach;
- *Chapter 4*: Overview of the experimental setup, data acquisition system employed, validation of the computational results with the comparison with experimental ones and parametric study and respective assessment;
- *Chapter 5*: Introduction to the optimization framework and optimized results;
- *Chapter 6*: Conclusion of the thesis with the last considerations about future improvement.

Chapter 2

Background

This second chapter addresses the theoretical concepts used in the present work, thus facilitating the comprehension of their application in the computational code. For this reason are introduced all the formulation and equations at the base of the computational solvers used in this research.

2.1 Noise Source Mechanisms

The most common and identifiable sources of rotors noise can be broadly divided into discrete-frequency (deterministic) and broadband noise components (non-deterministic) [36]. The discrete-frequency noise contains the deterministic components [37]:

- **Thickness noise:** noise due to displacement of fluid by rotor blade;
- **Loading noise:** noise due to force exerted on the fluid by the rotor blade surface;
- **Blade vortex interaction noise (BVI):** impulsive loading noise due to a tip vortex impacting a following blade;
- **High-speed impulsive noise (HSI):** in-plane noise associated with high advancing tip speeds (transonic noise).

Broadband noise is the result of turbulent flow interactions on or near the blade surface and its current prediction methods are semi-empirical, so it depends on measured data to find the constants required in the model. The non-deterministic loading noise sources are [37, 38]:

- **Turbulence ingestion noise** [39] : unsteady loading noise due to ingestion of atmospheric turbulence into the rotor;
- **Blade wake interaction noise** [40] : noise caused by blade interactions with rotor wake turbulence;
- **Blade self noise** [41, 42] : noise produced by scattering of turbulent flow over the blade trailing edge.

Thickness noise, since it is generated by the fluid displacement originated by the blade motion, it is governed by the rotor speed and the airfoil thickness distribution. Thickness noise propagates along the rotor disk plane. Meanwhile Loading noise, resulted from non-impulsive loading sources, propagates in a direction below the rotor disk and it is usually the dominant source of rotor noise. BVI noise is a specific type of loading noise generated by a very fast oscillation of the aerodynamic force on the blade surface as the result of an interaction between a shed tip vortex with the following blades. The BVI noise is the most significant noise source in approaching flight (low-speed descent or fly-over conditions) and propagates in an oblique direction below the rotor disk, as it is shown in figure 2.1 relatives to all the different sources of noise [37].

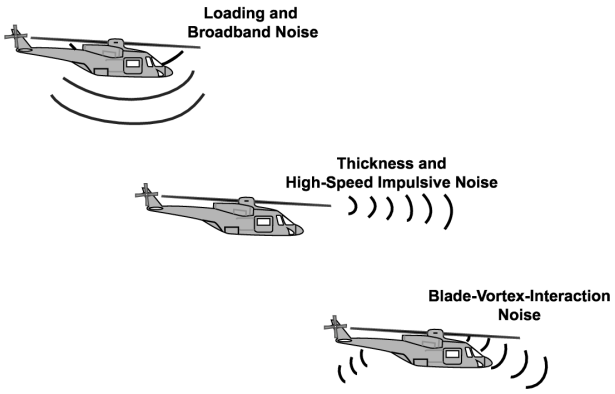

Figure 2.1: Primary rotor aerodynamic noise sources and associated directionalities for modern-day, full-scale helicopters, [38]

In case of high speed forward flight another source of noise could be the HSI noise, in particular when the rotor blade tips are at a Mach number higher than 0.85. HSI noise is significant with the occurrence of shocks and transonic flow on the advancing side of the rotor and it is propagated in the same direction as the thickness noise.

2.2 Aeroacoustic Computational Chain

The acoustic analysis and optimization of UAV rotors is a complex process, and generally it involves several different methods, as represented in figure 2.2.

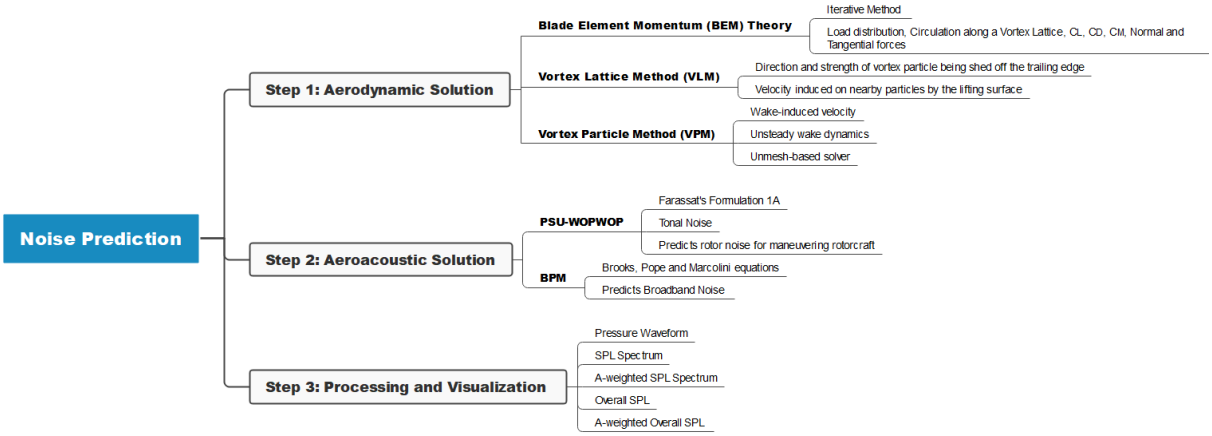

Figure 2.2: Model of aeroacoustic computational chain for the UAV rotor noise prediction

The first step of this computational chain is the calculation of the Aerodynamic loads through the implementation and cohesion of different methods:

- **Blade Element Momentum Theory (BEMT)** [43]: this iterative method is used to calculate the load distribution and for deriving the circulation along a vortex lattice representing the lifting surface;
- **Vortex Lattice Method (VLM)** [43]: used to elaborate the direction and strength of vortex particle being shed off the trailing edge and the velocity induced on nearby particles by the lifting surface;
- **Vortex Particle Method (VPM)** [43]: it is an unmesh-based solver well suited for the the calculation of the wake-induced velocity and for the analysis of the unsteady wake dynamic.

The aerodynamic results of this first step are used as inputs for the second one, regarding the aeroacoustic analysis, which implements two different tools:

- **PSU-WOPWOP (PSW)** [44]: this tool, based on the Farasat's Formulation 1A, is used to analyse and predict tonal noise (deterministic);
- **Brooks, Pope and Marcolini (BPM)** [44]: it studies the broadband noise capturing noise from turbulent boundary layer edge, separation stall, tip vortex formation, laminar boundary layer vortex shedding, and trailing edge bluntness vortex shedding.

Finally, in the last step the data obtained previously are processed and plotted, in order to be displayed by the user.

Before starting to describe in detail the computational tools, used in this work for the prediction and optimization of the noise produced by UAV rotors, it is necessary to briefly introduce the methods aforementioned and the basic governing equations.

2.3 Blade Element Momentum Theory (BEMT)

The Blade Element Momentum (BEM) theory is a model used to evaluate the performance of a propelling or extracting turbine based on its mechanical and geometric parameters as well as the characteristics of the interacting flow. This model results from the combination of two theories: the Blade Element Theory and the Momentum Theory. The Momentum Theory, also known as Disk Actuator Theory or Axial Momentum Theory, was introduced by William J. M. Rankine in 1865 [45] and is, unlike the Blade Element Theory, a global

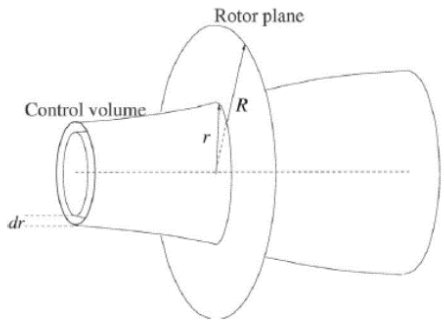

Figure 2.3: Control volume shaped as an annular element to be used in the BEM model

theory that adopts a macroscopic point of view to
model the behavior of a column of fluid passing through a turbine. This approach was later taken up independently by Frederick W. Lanchester [46], Albert Betz [47] and Nikolay Joukowsky [48, 49], to formulate Betz's Law, which gives the theoretical optimal efficiency of a thin rotor [50]. Meanwhile the Blade Element Theory is a local approach that, as suggested by its name, cuts the turbine blade into sections, the blade elements, each one of them being approximated by a planar model. This approach results in expressions of the forces exerted on the blade element, as functions of the flow characteristics and blade geometry. Each blade element is independent from the others since the model does not consider the interactions between blade elements. A combination of these two approaches was carried out in 1926 by Hermann Glauert [51], who also refined the Momentum Theory by considering the rotation of the fluid rings induced by its interaction with the turbine. In this way, Glauert's model couples two descriptions: a global macroscopic model that describes the evolution of fluids rings crossing the turbine, and a local one, that summarizes in 2D the behaviour of a section of a blade, a blade element, under the action of the fluid. It is the purpose of the blade element momentum method to compute the induction factors a and a' and thus the steady loads and thus also the thrust and power for different settings of wind speed, rotational speed and pitch angle. The streamtube shown in figure 2.3 is discretized into N annular elements of height dr applying the boundary conditions of no flow across the elements.

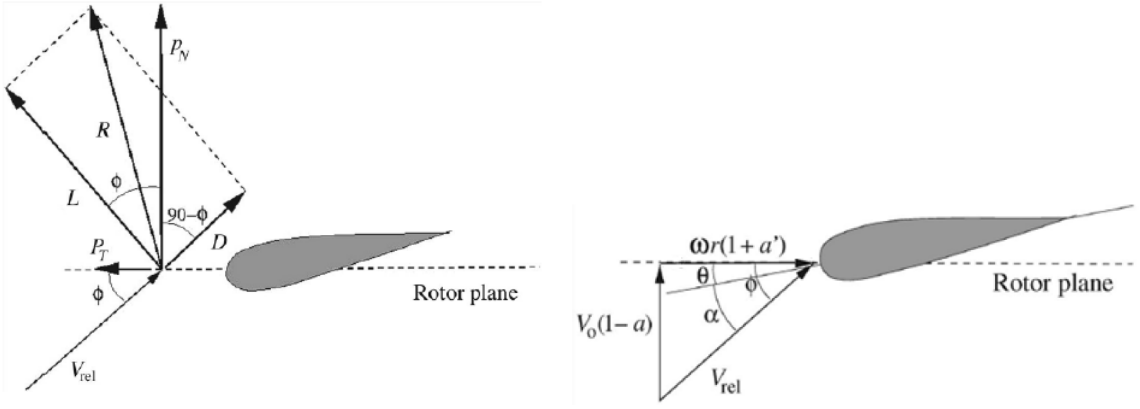

(a) Local loads on a blade; R is the vector sum of the lift and the drag. p_N and p_T are the normal and tangential components of R, respectively

(b) Velocities at the rotor-plane

Figure 2.4: Blade of the classical blade element momentum method

In the BEM model is assumed for the annular elements:

- No radial dependency, so what happens at one element cannot be felt by the others;
- The force from exercised by each annular element on the flow is constant

The thrust from the disc on this control volume can thus be found from the integral momentum equation since the cross section area of the control volume at the rotor plane is $2\pi r dr$:

$$dT = (V_0 - u_1)d\dot{m} = 2\pi r\rho u(V_0 - u_1)dr = 4\pi r\rho V_0^2 a(1-a)dr \tag{2.1}$$

where V_0 is the free-stream velocity, u_1 is the axial velocity in the wake, $u_1 = (1-2a)V_0$, and r is the radial position of the control volume. The torque dM on the annular element is found using the integral moment of momentum equation on the control volume and setting the rotational velocity upstream of the rotor to zero:

$$dM = 4\pi r^3 \rho V_0 \omega (1-a) a' dr \tag{2.2}$$

The left-hand sides of equations 2.1 and 2.2 are found from the local flow around the blade. Considering the single section of the blade, as shown in figure 2.4, it is possible to get the forces per length:

$$\begin{cases} l = \frac{1}{2}\rho V_{rel}^2 c C_l \\ d = \frac{1}{2}\rho V_{rel}^2 c C_d \\ p_N = l cos\Phi + d sin\phi \\ p_T = l sin\Phi - d cos\Phi \end{cases} \tag{2.3}$$

Normalizing the aforementioned equations respect to $\frac{1}{2}\rho V_{rel}^2 c$ and considering the definition of the coefficients C_n and C_t it is gotten the following system:

$$\begin{cases} C_n = C_l cos\Phi + C_d sin\Phi \\ C_t = C_l sin\Phi - C_d cos\phi \\ C_n = \frac{p_N}{\frac{1}{2}\rho V_{rel}^2 c} \\ C_t = \frac{p_T}{\frac{1}{2}\rho V_{rel}^2 c} \end{cases} \tag{2.4}$$

Using the velocity triangle of figure 2.4b it is possible to see that

$$V_{rel} = \frac{V_0(1-a)}{sin\Phi} \tag{2.5}$$

and

$$V_{rel} = \frac{\omega r}{(1+a')cos\Phi} \tag{2.6}$$

The normal force and the torque on the control volume of thickness dr is, since p_N and p_T are forces per length:

$$dT = B p_N dr \tag{2.7}$$

and

$$dM = r B p_T dr \tag{2.8}$$

where B is the number of blades.

Using equation 2.4 for p_N and equation 2.5 for V_{rel}, equation 2.7 becomes

$$dT = \frac{1}{2}\rho B \frac{V_0^2(1-a)^2}{sin\Phi^2} cC_n dr \tag{2.9}$$

equalizing this last equation with the previous one relatives to dT, 2.1, it is possible to define the axial induction factor a as:

$$a = \frac{1}{\frac{4sin\Phi^2}{\sigma C_n} + 1} \tag{2.10}$$

where σ is the solidity factor, $\sigma(r) = \frac{c(r)B}{2\pi r}$, and $c(r)$ is the local chord value.

In the same way, using the equation 2.4 for p_T and equations 2.5 and 2.6 for V_{rel}, equation 2.8 becomes

$$dM = \frac{1}{2}\rho B \frac{V_0(1-a)\omega r(1+a')}{sin\Phi cos\Phi} cC_t r dr \tag{2.11}$$

equalizing this last equation with the previous one relatives to dM, 2.2, it is possible to define the angular induction factor a' as:

$$a' = \frac{1}{\frac{4sin\Phi cos\Phi}{\sigma C_t} - 1} \tag{2.12}$$

2.4 Vortex Lattice Method (VLM)

The vortex lattice method, VLM, is one of the most practical approaches for the comprehensive analysis of the rotary and fixed wing systems. It is capable of accurately calculating the aerodynamic loads on the rotor blades operating in incompressible flow with affordable computational costs. The VLM is based on the fluid surrounding the body surface that is assumed to be of inviscid, incompressible ($\nabla \cdot \mathbf{V} = 0$) and irrotational ($\nabla \times \mathbf{V} = 0$) over the entire domain. It represents the lifting surface as an area on which a grid of horseshoe vortices is superimposed, in particular case the rotor blades are regarded as lifting surface without thickness which is divided into quadrilateral singularities containing the constant strength vortex ring elements. For each horseshoe is elaborated the velocities induced at a specific control point using the law of Biot-Savart. A summation is performed for all control points on the lifting surface to produce a set of linear algebraic equations for the horseshoe vortex strengths that satisfy the boundary condition of no flow through the lifting surface. The vortex strengths are related to the surface circulation and the pressure differential between the upper and the lower part. The pressure differentials are integrated to yield the total forces and moments.

In order to present the method, the case of wing surface that is approximated by a finite number of discrete horseshoe vortices, is illustrate in figure 2.5.

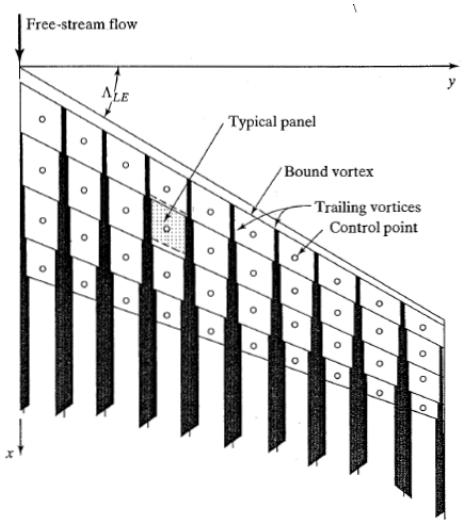

Figure 2.5: Elemental panels and horseshoe vortices for a typical wing planform in the vortex lattice method, from [52]

The individual horseshoe vortices are placed in trapezoidal panels (also called finite elements or lattices). The vortex lattice panels are located on the mean camber surface of the wing and when the trailing vortices leave the wing they follow a curved path. In the linearized approach, the trailing vortices are aligned either parallel to the free stream or parallel to the vehicle axis and the control point of each panel is centered spanwise on the three-quarter-chord line midway between the trailing-vortexes. Applying the boundary condition of tangent flow to the wing surface at the control point of each of the $2N$ panels is possible to provide a set of simultaneous equations in the unknown vortex circulation strengths. Following the law of Biot-Savart the velocity induced by a vortex filament of strength (Γ_n) and a length of dl is:

$$d\vec{V} = \frac{\Gamma_n(\vec{dl} \times \vec{r})}{4\pi r^3} \tag{2.13}$$

Referring to the sketch of figure 2.6, the magnitude of the induced velocity is

$$dV = \frac{\Gamma_n sin\theta dl}{4\pi r^2} \tag{2.14}$$

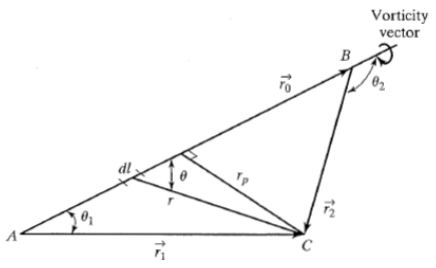

Figure 2.6: Nomenclature for calculating the velocity induced by a finite-length vortex segment, from [52]

Using the previous equation is possible to calculate the contribute of each segment separately. Let AB be such a segment, with the vorticity vector directed from A to B and C be a point in space whose normal distance from the line AB is r_p; it is possible to integrate between A and B to find the magnitude of the induced velocity:

$$V = \frac{\Gamma_n}{4\pi r_p} \int_{\theta_1}^{\theta_2} sin\theta d\theta = \frac{\Gamma_n}{4\pi r_p}(cos\theta_1 - cos\theta_2) \tag{2.15}$$

Let r_0, r_1 and r_2 designate the vectors AB, AC and BC, respectively, then:

$$r_p = \frac{|\vec{r_1} \times \vec{r_2}|}{r_0} \qquad cos\theta_1 = \frac{\vec{r_0} \cdot \vec{r_1}}{r_0 r_1} \qquad cos\theta_2 = \frac{\vec{r_0} \times \vec{r_2}}{r_0 r_2}$$

In this case if the vector quantity is written without the superscript arrow, the symbol represents the magnitude of the parameter. Also, the $|\vec{r_1} \times \vec{r_2}|$ represents the magnitude of the vector cross product. Substituting these expressions into equation 2.15 and noting that the direction of the induced velocity is given by the unit vector

$$\frac{\vec{r_1} \times \vec{r_2}}{|\vec{r_1} \times \vec{r_2}|}$$

yields

$$\vec{V} = \frac{\Gamma_n}{4\pi} \frac{\vec{r_1} \times \vec{r_2}}{|\vec{r_1} \times \vec{r_2}|^2} \left[\vec{r_0} \cdot \left(\frac{\vec{r_1}}{r_1} - \frac{\vec{r_2}}{r_2}\right)\right] \tag{2.16}$$

This is the basic expression for the calculation of the induced velocity by the horseshoe vortices in the VLM. Hence, the equation 2.16 can be used to compute the velocity that is induced to a general point in space (x,y,z) by the horseshoe vortex represented in figure 2.7. As already aforementioned the segment AB represents the bound vortex portion of the horseshoe system and coincides with the quarter-chord line of the panel element. The total induced velocity is elaborated by considering the influence of each of the elements.

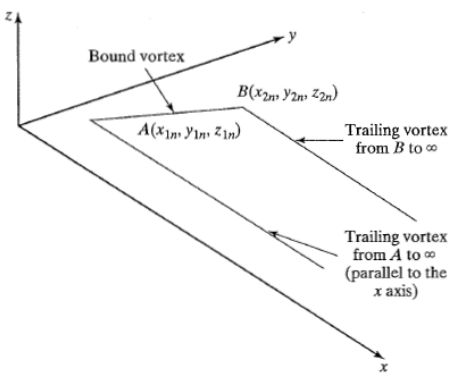

Figure 2.7: Horseshoe vortex, from [52]

The equation 2.16 can be rewritten as

$$\vec{V_{AB}} = \frac{\Gamma_n}{4\pi}\{Fac1_{AB}\}\{Fac2_{AB}\} \tag{2.17}$$

where

$$\begin{aligned}
\{Fac1_{AB}\} &= \frac{\vec{r_1} \times \vec{r_2}}{|\vec{r_1} \times \vec{r_2}|^2} \\
&= \{[(y-y_{1n})(z-z_{2n}) - (y-y_{2n})(z-z_{1n})]\hat{i} \\
&- [(x-x_{1n})(z-z_{2n}) - (x-x_{2n})(z-z_{1n})]\hat{j} \\
&+ [(x-x_{1n})(y-y_{2n}) - (x-x_{2n})(y-y_{1n})]\hat{k}\} \\
&/\{[(y-y_{1n})(z-z_{2n}) - (y-y_{2n})(z-z_{1n})]^2 \\
&+ [(x-x_{1n})(z-z_{2n}) - (x-x_{2n})(z-z_{1n})]^2 \\
&+ [(x-x_{1n})(y-y_{2n}) - (x-x_{2n})(y-y_{1n})]^2\}
\end{aligned}$$

and

$$\begin{aligned}
\{Fac2_{AB}\} &= \left(\vec{r_0} \cdot \frac{\vec{r_1}}{r_1} - \vec{r_0} \cdot \frac{\vec{r_2}}{r_2}\right) \\
&= \{[(x_{2n}-x_{1n})(x-x_{1n}) + (y_{2n}-y_{1n})(y-y_{1n}) + (z_{2n}-z_{1n})(z-z_{1n})]/ \\
&\sqrt{(x-x_{1n})^2 + (y-y_{1n})^2 + (z-z_{1n})^2} \\
&- [(x_{2n}-x_{1n})(x-x_{2n}) + (y_{2n}-y_{1n})(y-y_{2n}) + (z_{2n}-z_{1n})(z-z_{2n})]/ \\
&\sqrt{(x-x_{2n})^2 + (y-y_{2n})^2 + (z-z_{2n})^2}\}
\end{aligned}$$

In order to calculate the velocity induced by the filament that extends from A to ∞ it is necessary first elaborate the velocity induced by the collinear, finite-length filament that extends from A to D.

$$\vec{V_{AD}} = \frac{\Gamma_n}{4\pi}\{Fac1_{AD}\}\{Fac2_{AD}\}$$

where

$$\{Fac1_{AD}\} = \frac{(z-z_{1n})\hat{j} + (y_{1n}-y)\hat{k}}{[(z-z_{1n})^2 + (y_{1n}-y)^2](x_{3n}-x_{1n})}$$

and

$$\{Fac2_{AD}\} = (x_{3n} - x_{1n})\Bigg\{\frac{x_{3n} - x}{\sqrt{(x - x_{3n})^2 + (y - y_{1n})^2 + (z - z_{1n})^2}} + \frac{x - x_{1n}}{\sqrt{(x - x_{1n})^2 + (y - y_{1n})^2 + (z - z_1 n)^2}}\Bigg\}$$

Letting x_3 go to ∞, the first term of $\{Fac2_{AD}\}$ goes to 1.0. Therefore, the velocity induced by the vortex filament which extends from A to ∞ in a positive direction parallel to the x axis is given by

$$\vec{V_{A\infty}} = \frac{\Gamma_n}{4\pi}\left\{\frac{(z - z_{1n})\hat{j} + (y_{1n} - y)\hat{k}}{[(z - z_{1n})^2 + (y_{1n} - y)^2}\right\}\left[1.0 + \frac{x - x_{1n}}{\sqrt{(x - x_{1n})^2 + (y - y_{1n})^2 + (z - z_{1n})^2}}\right] \tag{2.18}$$

Similarly, the velocity induced by the vortex filament that extends from B to ∞ is a positive direction parallel to the x axis is given by

$$\vec{V_{B\infty}} = \frac{\Gamma_n}{4\pi}\left\{\frac{(z - z_{2n})\hat{j} + (y_{2n} - y)\hat{k}}{[(z - z_{2n})^2 + (y_{2n} - y)^2}\right\}\left[1.0 + \frac{x - x_{2n}}{\sqrt{(x - x_{2n})^2 + (y - y_{2n})^2 + (z - z_{2n})^2}}\right] \tag{2.19}$$

So, the totally velocity induced at some point of coordinates (x,y,z) by the horseshoe vortex representing one of the surface elements is the sum of the components given in equation 2.17, 2.18 and 2.19. Considering the different panels in which the lifting surface is divided and a point (x,y,z) of the m_{th} panel, the velocity induced at this point by the vortex representing the n_{th} panel will be designated as $\vec{V_{m,n}}$:

$$\vec{V_{m,n}} = \vec{G_{m,n}}\Gamma_n \tag{2.20}$$

Where the influence coefficient $\vec{G_{m,n}}$ depends on the geometry of the n_{th} horseshoe and its distance from the control point on the m_{th} panel. Through the linearity of the governing equations it is possible to evaluate the velocities induced on the m_{th} control point adding together the $2N$ vortices:

$$\vec{V_m} = \sum_{n=1}^{2N} \vec{G_{m,n}}\Gamma_n \tag{2.21}$$

Anyway, in order to elaborate the resultant induced velocity at any point in space it is necessary to know the strength of the $2N$ horseshoe vortices (Γ_n), and for this reason it is used the boundary condition that the surface is a streamline. This means that the resultant flow is tangent to the wing at each and every control point. If the flow is tangent to the wing, the component of the induced velocity normal to the wing at the control point balances the normal component of the free-stream velocity. Applying the instantaneous zero normal flow boundary condition on the control point of each element, a set of algebraic equations for the unknown strength of vortices can be established

$$\begin{pmatrix} G_{1,1} & \dots & G_{1,j} & \dots & G_{1,n} \\ \vdots & \ddots & & & \\ G_{i,j} & & G_{i,j} & & \\ \vdots & & & \ddots & \\ G_{m,1} & & & & G_{m,n} \end{pmatrix} \begin{pmatrix} \Gamma_1 \\ \vdots \\ \Gamma_j \\ \vdots \\ \Gamma_n \end{pmatrix} = \begin{pmatrix} -V_{\infty 1} \\ \vdots \\ -V_{\infty i} \\ \vdots \\ -V_{\infty m} \end{pmatrix} \tag{2.22}$$

$$\mathbb{G}\Gamma = \mathbb{V}_{\hat{n}}$$

$$\Rightarrow \Gamma = \mathbb{G}^{-1}\mathbb{V}_{\hat{n}}$$

Where the matrix G is regarded the influence coefficient, and the V elements are referred to the normal components of the free-stream velocity [52].

2.5 PSU-WOPWOP (PSW)

PSU-WOPWOP is a complete rewrite of the original WOPWOP code, written at the Pennsylvania State University, utilizing object-oriented design principles and focusing on the prediction of the noise of maneuvering rotorcraft or any other moving body. It uses a different calculation algorithm than the original WOPWOP code; it is in general much more flexible, both in terms of input and output than the previous version. The theoretical background of the new code PSU-WOPWOP is the same of the original one. In this chapter is analysed the underlying theory [53].

2.5.1 The Ffowcs Williams-Hawkings Equation

Almost all actual rotor noise prediction tools, and also the one used in this study, are based on time-domain integral formulations of the Ffowcs Williams-Hawkings (FW-H) equation. The FW-H equation is based on the Lighthill's acoustic analogy and it is an exact rearrangement of the continuity equation and the Navier-Stokes (N-S) equations into the form of an inhomogeneous wave equation [14].

The equations of mass and momentum conservation are the basis of the aerodynamic generation of sound. It is possible to combine these two equations considering a closed surface, obtaining an inhomogeneous wave equation that governs the propagation of the sound waves in a region exterior to the closed internal surface.

These equations of mass continuity and momentum are merely valid for fluid flow with discontinuities, so the mathematical model, used to divide into regions the unbounded fluid, must conserve these discontinuities inducing mass and momentum sources. These sources act as sound generators. The moving surface is described by $f(\bar{x}, t) = 0$ and is defined such that $\nabla f = \vec{n}$, the unit outward normal vector to the surface; it encloses the noise generation region of the flow. In addition, it is assumed that $f > 0$ in the exterior of the surface and $f < 0$ in the interior, as shown in figure 2.8.

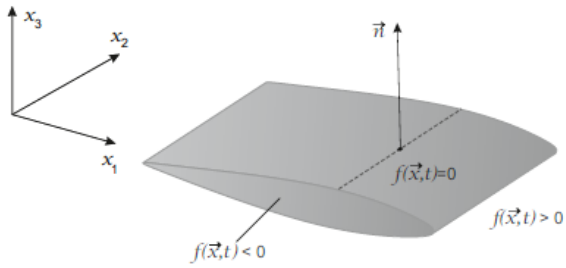

Figure 2.8: Definition of the moving surface, from [54]

The mass and momentum conservation equations in the area outside the surface, within the fluid ($f > 0$), neglecting the viscous shear force over the blade surface acting on the fluid, are given by:

$$\frac{\partial \rho}{\partial t} + \frac{\partial}{\partial x_i}(\rho u_i) = 0 \tag{2.23}$$

$$\frac{\partial}{\partial t}(\rho u_i) + \frac{\partial}{\partial x_j}(\rho u_i u_j + p_{ij}) = 0 \tag{2.24}$$

Where ρ is the fluid density, ρu_i is the component of the fluid momentum, $p_{ij} = p'\delta_{ij}$ is the compression stress tensor and δ_{ij} is the Kronecker delta.

As aforementioned, these conservation laws change in presence of the artificial discontinuity introduced by the surface $f = 0$ and the normal derivatives must be replaced by generalized derivatives. A brief explanation about generalized derivatives is given here.
Considering $q(\vec{x})$, function of $\vec{x} = (x_1, x_2, x_3)$ with a discontinuity across the surface $f(\vec{x}) = 0$, its partial generalized derivative in order to x_i is obtained through this equation:

$$\frac{\overline{\partial} q}{\partial x_i} = \frac{\partial q}{\partial x_i} + \Delta q \frac{\partial f}{\partial x_i}\delta(f) \tag{2.25}$$

Here Δq is the difference of $q(\vec{x})$ across $f = 0$: $\Delta q = q(f = 0^+) - q(f = 0^-)$, $\delta(f)$ is the Dirac delta function. The partial derivative $\frac{\overline{\partial} q}{\partial x_i}$ represents the derivative of the function $q(\vec{x})$ with discontinuities, while $\frac{\partial q}{\partial x_i}$ represents the partial derivative of the continuous and derivable function without gap.

Applying this rule to the the equation 2.23 and 2.24 is possible to obtain:

$$\frac{\overline{\partial}\rho}{\partial t} + \frac{\overline{\partial}}{\partial x_i}(\rho u_i) = \frac{\partial \rho}{\partial t} + \Delta\rho\frac{\partial f}{\partial t}\delta(f) + \frac{\partial}{\partial x_i}(\rho u_i) + \Delta(\rho u_i)\frac{\partial f}{\partial x_i}\delta(f) \tag{2.26}$$

$$\frac{\overline{\partial}}{\partial t}(\rho u_i) + \frac{\overline{\partial}}{\partial x_j}(\rho u_i u_j + p_{ij}) = \frac{\partial}{\partial t}(\rho u_i) + \Delta(\rho u_i)\frac{\partial f}{\partial t}\delta(f) + \frac{\partial}{\partial x_j}(\rho u_i u_j + p_{ij}) + \Delta(\rho u_i u_j + p_{ij})\frac{\partial f}{\partial x_j}\delta(f) \tag{2.27}$$

The stress tensor p_{ij} has its mean value $p_0\delta_{ij}$ in both regions, thus the constant p_0 disappears from the equation 2.27 and the symbol p_{ij} can have a different interpretation, representing the difference between tensor and its mean value. For this reason, the interior condition is $p_{ij} = 0$. Moreover, it's assumed that the surface is impermeable, for this reason, in the exterior region, $u_n = v_n$ because the

normal velocity of the fluid is equal to the normal velocity of the surface. In this case $v_n = u_i n_i$ is the local fluid velocity in the normal direction to the surface, since $u_n = v_n = -\frac{\partial f}{\partial t} = -(\frac{\partial f}{\partial x_i})(\frac{\partial x_i}{\partial t})$, with $\frac{\partial f}{\partial x_i} = n_i$ and $\frac{\partial x_i}{\partial t} = u_i$.

Applying these last conditions to the equations 2.26 and 2.27 and remembering that the difference $\Delta\rho$ is equal to $(\rho_0 - \rho)$ and $\Delta(\rho u_i)$ to ρu_i, it is possible to obtain the following equations:

$$\begin{aligned}\overline{\frac{\partial \rho}{\partial t}} + \frac{\overline{\partial}}{\partial x_i}(\rho u_i) &= \frac{\partial \rho}{\partial t} + \frac{\partial}{\partial x_i}(\rho u_i) + (\rho - \rho_0)(-v_n)\delta(f) + (\rho u_n)\delta(f) \\ &= \rho_0 v_n \delta(f) + \rho(u_n - v_n)\delta(f) \\ &= \rho_0 v_n \delta(f)\end{aligned} \tag{2.28}$$

$$\begin{aligned}\frac{\overline{\partial}}{\partial t}(\rho u_i) + \frac{\overline{\partial}}{\partial x_i}(\rho u_i u_j + p_{ij}) &= \frac{\partial}{\partial t}(\rho u_i) + \frac{\partial}{\partial x_i}(\rho u_i u_j + p_{ij}) + \rho u_i(-v_n)\delta(f) + \rho u_i u_n + p_{ij} n_j \delta(f) \\ &= \rho u_i(u_n - v_n)\delta(f) + p_{ij} n_j \delta(f) \\ &= p_{ij} n_j \delta(f)\end{aligned} \tag{2.29}$$

At this point the equation 2.29 is subtracted from equation 2.28. Subsequently, $\frac{\partial p'}{\partial x_i \partial x_j}$ is subtracted from the resulting equation, giving:

$$(\frac{\partial^2}{\partial t^2} - c^2 \frac{\partial^2}{\partial x_i^2})(\overline{\rho - \rho_0}) = \frac{\partial}{\partial t}[\rho_0 v_n \delta(f)] - \frac{\partial}{\partial x_i}[p_{ij} n_j \delta(f)] + \frac{\partial^2 \overline{T_{ij}}}{\partial x_i \partial x_j} \tag{2.30}$$

In this equation $\overline{T_{ij}}$ is a generalized function equal to Lighthill's stress tensor, that is equal to $T_{ij} = \rho u_i u_j + p_{ij} - c^2(\rho - \rho_0)\delta_{ij}$ outside any surfaces and equal to zero inside them.
From the expression 2.30 it is possible to notice that the sound is generated by three different sources distributions:

- The first term is a monopole source frequently associated to the thickness noise;
- The second term is a dipole source associated to the loading noise;
- The last term is the quadrupole source, associated to the HSI noise propagation, of strength density T_{ij} distributed along the whole exterior volume of the surface. It models the non-linearity from local sound speed variation and finite fluid velocity in the region near the surface.

2.5.2 Formulation 1A of Farassat

An integral form of the FW-H solution was developed by Farassat which neglects the quadrupole terms because volume integrals are computationally expensive and PSU-WOPWOP neglets them; for subsonic noise generation the surface source terms (the monopole and dipole) are the most significant. In this section the derivation of Formulation 1 of Farassat will be presented, but just as intermediate step to achieve of the Formulation 1A.

Firstly, the equation 2.30 can be rewritten, in order to simplify the operations throughout the derivation, as:

$$\Box^2 p' = \frac{1}{c^2}\frac{\partial^2 p'}{\partial t^2} - \nabla^2 p' = \frac{\partial}{\partial t}[\rho v_n \delta(f)] - \frac{\partial}{\partial x_i}[l_i \delta(f)] + \frac{\partial^2}{\partial x_i \partial x_j}[H(f) T_{ij}] \tag{2.31}$$

Where $\Box$ is the D'Alembert operator given by $\Box^2 = (\frac{1}{c^2})(\frac{\partial^2}{\partial t^2}) - \nabla^2$, l_i is equivalent to $p_{ij} n_j$ and $H(f)$ is the Heaviside function, which is defined by:

$$H(f) = \begin{cases} 0 & f < 0 \\ 1 & f > 0 \end{cases} \tag{2.32}$$

As aforementioned, also on the right hand side of the equation 2.31 it is possible to distinguish the monopole, the dipole and quadrupole terms, respectively, due to their mathematical structure. In fact, the first two terms involve the Dirac delta function $\delta(f)$, and, for this reason, they act on the surface where $f = 0$. On the other side, the quadrupole source acts on the volume surrounding the surface given the presence of the Heaviside function ($H(f)$).

This latter requires volume integration and an accurate prediction of the flow field , which involves a large computational cost. For this reason, the quadrupole terms has been neglected in the solution proposed by Farassat. Moreover, the contribution of the quadrupole term is not significant in many subsonic applications. So, the formulation 1A describes the acoustic pressure fluctuation produced by an acoustic data surface (ADS) as a sum of two terms, monopole (thickness) p'_T and dipole (loading) p'_L. Consequently, the objective is to find the solution of the following two wave equations:

$$\Box^2 p'_T = \frac{\partial}{\partial t}[\rho_0 v_n \delta(f)] \tag{2.33}$$

$$\Box^2 p'_L = -\frac{\partial}{\partial x_i}[l_i \delta(f)] \tag{2.34}$$

Both equations are written in the same form of the following one:

$$\Box^2 p' = Q(x,t)\delta(f) \tag{2.35}$$

The integral representation of the solution of the above equation can be found using the Green's function:

$$G(x,t;y,\tau) = \begin{cases} 0 & \tau > t \\ \frac{\delta(\tau - t + \frac{r}{c})}{4\pi r} & \tau \leq t \end{cases} \tag{2.36}$$

Here $r = |x - y|$ and $(x,t),(y,\tau)$ are the observer and the source space-time variables, respectively. The term $\tau - t + \frac{r}{c}$ is frequently referred as g.

The solution of the equation 2.35 is, consequently, given by:

$$4\pi p' = \int Q(y,\tau)\delta(f)\frac{\delta(g)}{r} dy d\tau \tag{2.37}$$

The x-frame and y-frame are fixed to the undisturbed medium, so the Lagrangian coordinates η must be introduced because it is easier to specify the strength in a coordinate system moving with the surface. The Lagrangian coordinates are related to the fixed system by:

$$y = \eta + \int^{\tau} cM(\eta, \tau) d\tau \tag{2.38}$$

Where cM is the source convection velocity. In this way, y depends from η and τ and the inverse transformation is given by:

$$\eta = \eta(y, \tau) \tag{2.39}$$

The transformations are isometric since they involved just translation and rotation; hence, the Jacobian of both is unitary:

$$\det(\frac{\partial y}{\partial \eta}) = 1 \tag{2.40}$$

$$\det(\frac{\partial \eta}{\partial y}) = 1 \tag{2.41}$$

Firstly, it is considered the transformation $y \to \eta$:

$$\begin{aligned} 4\pi p' &= \int Q(y, (\eta, \tau), \tau) \delta(f) \frac{\delta(g)}{r \left|\det(\partial \eta / \partial y)\right|} d\eta d\tau \\ &= \int Q(\eta, \tau) \delta(f) \frac{\delta(g)}{r} d\eta d\tau \end{aligned} \tag{2.42}$$

Before considering the transformation $\tau \to g$ it is necessary to take into account some algebraic consideration:

$$\frac{\partial g}{\partial \tau} = \frac{\partial}{\partial \tau}(\tau - t + r/c) + \frac{1}{c} \frac{\partial r}{\partial y_i} \frac{\partial y_i}{\partial \tau} = 1 - \frac{\hat{r_i} v_i}{c} = 1 - M_r \tag{2.43}$$

Where M_r is the Mach number of the point η in the radiation direction at time τ, $\hat{r_i}$ is the component of unit radiation vector, $(x - y)/r$, and $v_i = \partial y_i / \partial \tau$ is the component of the velocity v of the point η with respect to the y-frame.

Combining the equations 2.42 and 2.43 is possible to write:

$$\begin{aligned} 4\pi p' &= \int Q(\eta, \tau) \delta(f) \frac{\delta(g)}{r \left|\partial g / \partial \tau\right|} d\eta d\tau \\ &= \int_{\mathbb{R}^3} \left(\frac{Q(\eta, \tau)}{r \left|1 - M_r\right|} \delta(f) \right)_{g=0} d\eta \end{aligned} \tag{2.44}$$

The observer space-time variables are kept fixed and the surface $g = 0$ can be visualized as:

$$g = \tau - t + r/c = 0 \Rightarrow |r| = |x - y| = c(t - \tau) \tag{2.45}$$

This function, with source space-time variables, is a sphere with centre at x and radius equal to $c(t - \tau)$, as illustrated in figure 2.9.

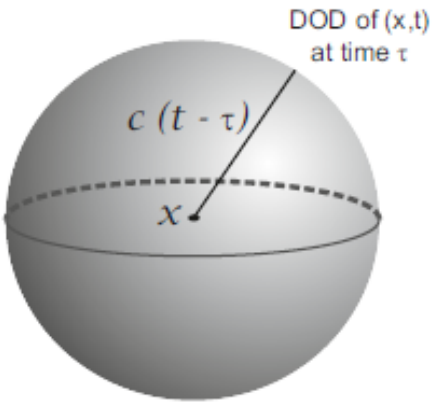

Figure 2.9: Visualization of the surface g=0, from [54]

As aforementioned in the equation 2.36 , the Green's function is nonzero when $\tau < t$ and the radius of the sphere ranges in a large set of values: from an infinetly large number for $\tau = -\infty$ to zero for $t = \tau$. This is the reason why this sphere is called Collapsing sphere.

For a further simplification it is possible to write $\tau_e = \tau(x, t; \eta)$ and $y_e = y(\eta, \tau_e)$, then:

$$r_e = |x - y_e| = c(t - \tau_e) \tag{2.46}$$

Where r_e is the emission distance of the source in η to the observer in x, y_e is the emission position and τ_e is the emission time. Using these new definitions, the equation 2.44 can rewritten as:

$$4\pi p' = \int_{\mathbb{R}^3} \frac{Q(\eta, \tau_e)}{r_e(1 - M_{r_e})} \delta(f) d\eta \tag{2.47}$$

This integral in the space $\mathbb{R}^3$ for a generic function $q(y)$ can be expressed as:

$$\int_{\mathbb{R}^3} q(y)\delta(f)dy = \int_{f=0} q(y)dS \tag{2.48}$$

Where S is the surface defined by $f(x, t) = 0$.

These results can be combined, converting the equation 2.47 in the following equation:

$$4\pi p' = \int_{f=0} \left[\frac{Q(y, \tau)}{r(1 - M_r)} \right]_{ret} dS \tag{2.49}$$

Where the subscript ret refers to the retarded time.

Formulation 1 of Farassat is now derived. The thickness noise part of the formulation can be achieved through the solution of the equation 2.35:

$$4\pi p'_T(x, t) = \frac{\partial}{\partial t} \int_{f=0} \left[\frac{\rho_0 v_n}{r(1 - M_r)} \right]_{ret} dS \tag{2.50}$$

The order of the derivative has been changed using the Leibniz rule of differentiation under an integral

sign:

$$\frac{\partial}{\partial t}\int Q(y,\tau)\delta(f)\frac{\delta(g)}{r}dyd\tau = \int Q(y,\tau)\delta(f)\frac{\partial}{\partial t}\left(\frac{\delta g}{r}\right)dyd\tau \tag{2.51}$$

In order to derive the Loading noise term, the solution of the equation 2.34 is rewritten using the free-space Green's function:

$$\begin{aligned} 4\pi p'_L(x,t) &= -\frac{\partial}{\partial x_i}\int l_i\delta(f)\frac{\delta(g)}{r}dyd\tau \\ &= -\int l_i\delta(f)\frac{\partial}{\partial x_i}\left(\frac{\delta(g)}{r}\right)dyd\tau \end{aligned} \tag{2.52}$$

Where:

$$\frac{\partial}{\partial x_i}\left(\frac{\delta(g)}{r}\right) = -\frac{1}{c}\frac{\partial}{\partial t}\left(\frac{\hat{r_i}\delta(g)}{r}\right) - \frac{\hat{r_i}\delta(g)}{r^2} \tag{2.53}$$

In this way:

$$\begin{aligned} 4\pi p'_L(x,t) &= \frac{1}{c}\int l_i\delta(f)\frac{\partial}{\partial t}\left(\frac{\hat{r_i}\delta(g)}{r}\right)dyd\tau + \int l_i\delta(f)\hat{r_i}\frac{\delta(g)}{r^2}dyd\tau \\ &= \frac{1}{c}\frac{\partial}{\partial t}\int l_i\delta(f)\hat{r_i}\frac{\delta(g)}{r}dyd\tau + \int l_i\delta(f)\hat{r_i}\frac{\delta(g)}{r^2}dyd\tau \end{aligned} \tag{2.54}$$

Now it is possible to define the Loading noise contribution in the Formulation 1:

$$4\pi p'_L(x,t) = \frac{1}{c}\frac{\partial}{\partial t}\int\left[\frac{l_r}{r(1-M_r)}\right]_{ret}dS + \int\left[\frac{l_r}{r^2(1-M_r)}\right]_{ret}dS \tag{2.55}$$

Where $l_r = l_i\hat{r_i}$ and $l_i = p_{ij}n_j$.

The speed and accuracy of the elaboration of the Thickness and Loading noise improve if the numerical differentiation is eliminated. For this reason, it is necessary to proceed to the derivation of the Formulation 1A of Farassat.

Through the definition of the surface $g = 0$ it is possible to obtain the following results:

$$g = \tau - t + r/c \Rightarrow \left(\frac{\partial\tau}{\partial t}\right)_{x,\eta} - 1 + \frac{1}{c}\left(\frac{\partial r}{\partial t}\right)_{x,\eta} = 0 \tag{2.56}$$

Where

$$\left(\frac{\partial r}{\partial t}\right)_{x,\eta} = \left(\frac{\partial r}{\partial\tau}\right)_{x,\eta}\left(\frac{\partial\tau}{\partial t}\right)_{x,\eta} \tag{2.57}$$

$$\left(\frac{\partial r}{\partial\tau}\right)_{x,\eta} = \frac{\partial r}{\partial y_i}\left(\frac{\partial y_i}{\partial\tau}\right)_{x,\eta} = -v_i\hat{r_i} = -v_r \tag{2.58}$$

v_r is the velocity of the point η in the radiation direction.

In this way, from equation 2.56 it is possible to obtain:

$$\left(\frac{\partial \tau}{\partial t}\right)_{x,\eta} = \frac{1}{1-M_r} \tag{2.59}$$

Replacing this latter expression in equation 2.55, the Loading noise contribution is given by:

$$4\pi p'_L(x,t) = \frac{1}{c}\frac{1}{1-M_r}\frac{\partial}{\partial t}\int_{f=0}\left[\frac{l_r}{r(1-M_r)}\right]_{ret} dS + \int_{f=0}\left[\frac{l_r}{r^2(1-M_r)}\right]_{ret} dS \tag{2.60}$$

In the same manner, the Thickness noise is obtained:

$$4\pi p'_T(x,t) = \frac{1}{1-M_r}\frac{\partial}{\partial \tau}\int_{f=0}\left[\frac{\rho_o v_n}{r(1-M_r)}\right]_{ret} dS \tag{2.61}$$

In order to obtain the last form of the formulations the following derivatives are used:

$$\frac{\partial r}{\partial y_i}\frac{\partial y_i(\eta,\tau)}{\partial \tau} = -\hat{r_i}\cdot v_i = -v_r \tag{2.62}$$

$$\frac{\partial \hat{r_i}}{\partial \tau} = \frac{\hat{r_i}v_r - v_i}{r} \tag{2.63}$$

$$\frac{\partial M_i}{\partial r}\cdot \hat{r_i} + M\frac{\partial \hat{r_i}}{\partial \tau} = \frac{1}{c}\left[\dot{v_i}\hat{r_i} + v_i\left(\frac{\hat{r_i}v_r - v_i}{r}\right)\right] = \hat{r_i}\dot{M_i} + c\frac{(M_r^2 - M^2)}{r} \tag{2.64}$$

Hence, for the Thickness noise:

$$\begin{aligned}
4\pi p'_T(x,t) &= \frac{1}{1-M_r}\int_{f=0}\left[\frac{1}{r(1-M_r)}\frac{\partial}{\partial\tau}(\rho v_n) - \frac{\rho v_n}{r^2(1-M_r)^2}\frac{\partial}{\partial\tau}[r(1-M_r]\right]_{ret} dS \\
&= \int_{f=0}\left\{\frac{\rho_0 \dot{v_n}}{r(1-M_r)^2} - \frac{\rho_0 v_n}{r^2(1-M_r)^3}\left[r\frac{\partial}{\partial\tau}(1-M_r) + (1-M_r)\frac{\partial r}{\partial\tau}\right]\right\}_{ret} dS \\
&= \int_{f=0}\left\{\frac{\rho_0 \dot{v_n}}{r(1-M_r)^2} + \frac{\rho_0 v_n}{r^2(1-M_r)^3}\left[r(\hat{r_i}\dot{M_i} + c\frac{(M_r^2-M^2)}{r} + (1-M_r)(v_r)\right]\right\}_{ret} dS \\
&= \int_{f=0}\left[\frac{\rho_0 \dot{v_n}}{r(1-M_r)^2} + \frac{\rho_0 v_n}{r^2(1-M_r)^3}(r\hat{r_i}\dot{M_i} - cM^2 + cM_r)\right]_{ret} dS \\
&= \int_{f=0}\left[\frac{\rho_0 \dot{v_n}}{r(1-M_r)^2}\right]_{ret} dS + \int_{f=0}\left[\frac{\rho_0 v_n}{r^2(1-M_r)^3}[r\dot{M_r} + c(M_r - M^2)]\right]_{ret} dS
\end{aligned} \tag{2.65}$$

And for the Loading noise, using the equation 2.60:

$$
\begin{aligned}
4\pi p'_L(x,t) &= \frac{1}{c}\frac{1}{1-M_r}\frac{\partial}{\partial\tau}\int_{f=0}\left[\frac{l_r}{r(1-M_r)}\right]_{ret}dS + \int_{f=0}\left[\frac{l_r}{r^2(1-M_r)}\right]_{ret}dS \\
&= \frac{1}{c}\frac{1}{1-M_r}\int_{f=0}\left[\frac{1}{r(1-M_r)}\frac{\partial}{\partial\tau}(l_i\cdot\hat{r_i}) - \frac{l_r}{r^2(1-M_r)^2}\frac{\partial}{\partial\tau}[r(1-M_r)]\right]_{ret}dS \\
&+ \int_{f=0}\left[\frac{l_r}{r^2(1-M_r)}\right]_{ret}dS \\
&= \frac{1}{c}\frac{1}{1-M_r}\int_{f=0}\left[\frac{1}{r(1-M_r)}\left(\hat{r_i}\frac{\partial l_i}{\partial\tau} + l_i\frac{\partial\hat{r_i}}{\partial\tau}\right) - \frac{l_r}{r^2(1-M_r)^2}\left((1-M_r)\frac{\partial r}{\partial\tau} - r\frac{\partial M_r}{\partial\tau}\right)\right]_{ret}dS \\
&+ \int_{f=0}\left[\frac{l_r}{r^2(1-M_r)}\right]_{ret}dS \\
&= \frac{1}{c}\frac{1}{1-M_r}\int_{f=0}\left[\frac{\dot{l_r}}{r(1-M_r)} + \frac{l_i}{r(1-M_r)}\left(\frac{\hat{r_i}v_r - v_i}{r}\right) + \frac{l_r}{r^2(1-M_r)^2}[cM_r + r\hat{r_i}\dot{M_i} - cM^2]\right]_{ret}dS \\
&+ \int_{f=0}\left[\frac{l_r}{r^2(1-M_r)}\right]_{ret}dS \\
&= \frac{1}{c}\frac{1}{1-M_r}\int_{f=0}\left[\frac{\dot{l_r}}{r(1-M_r)} + \frac{l_r v_r}{r^2(1-M_r)} - \frac{l_M c}{r^2(1-M_r} + \frac{l_r\hat{r_i}\dot{M_i}}{r(1-M_r)^2} + \frac{l_r c(M_r-M^2)}{r^2(1-M_r)^2}\right]_{ret}dS \\
&+ \int_{f=0}\left[\frac{l_r}{r^2(1-M_r)}\right]_{ret}dS \\
&= \frac{1}{c}\int_{f=0}\left[\frac{\dot{l_r}}{r(1-M_r)^2} + \frac{l_r M_r c}{r^2(1-M_r)^2} - \frac{l_M c}{r^2(1-M_r)^2} + \frac{l_r\dot{M}_r r + l_r c(M_r-M^2)}{r^2(1-M_r)^3} + \frac{l_r c}{r^2(1-M_r)}\right]_{ret}dS \\
&= \frac{1}{c}\int_{f=0}\left[\frac{\dot{l_r}}{r(1-M_r)^2}\right]_{ret}dS + \frac{1}{c}\int_{f=0}\left[\frac{l_r(r\dot{M}_r + cM_r - cM^2)}{r^2(1-M_r)^3}\right]_{ret}dS + \int_{f=0}\left[\frac{l_r - l_M}{r^2(1-M_r)^2}\right]_{ret}dS
\end{aligned}
\tag{2.66}
$$

where l_M is the component of the normal load of the section in the Mach number direction, which can be expressed as follows:

$$
l_M = l_i M_i = l_i\frac{v_i}{c} \tag{2.67}
$$

So, the final result that describes the acoustic pressure fluctuation produced by an acoustic data surface is given by the sum of the two contributions (thickness p'_T and loading p'_L):

$$
p'(x,t) = p'_T(x,t) + p'_L(x,t) \tag{2.68}
$$

Where the thickness p'_T and loading p'_L contributions are calculated from:

$$
\boxed{4\pi p'_T(x,t) = \int_{f=0}\left[\frac{\rho_0\dot{v_n}}{r(1-M_r)^2}\right]_{ret}dS + \int_{f=0}\left[\frac{\rho_0 v_n}{r^2(1-M_r)^3}[r\dot{M}_r + c(M_r-M^2)]\right]_{ret}dS} \tag{2.69}
$$

$$
\boxed{4\pi p'_L(x,t) = \frac{1}{c}\int_{f=0}\left[\frac{\dot{l_r}}{r(1-M_r)^2}\right]_{ret}dS + \frac{1}{c}\int_{f=0}\left[\frac{l_r(r\dot{M}_r + cM_r - cM^2)}{r^2(1-M_r)^3}\right]_{ret}dS + \int_{f=0}\left[\frac{l_r - l_M}{r^2(1-M_r)^2}\right]_{ret}dS} \tag{2.70}
$$

As it has already been seen in the previous equations 2.65 and 2.66.

In this formulation, integral terms with $1/r$ dependence are far-field terms since, for large r, their strength is relatively higher than those terms that include a factor of $1/r^2$, which are near-field terms. A Doopler factor $(1 - M_r)^{-1}$ is present in each term of Formulation 1A; this is raised to either 2^{nd} or 3^{rd} power depending on the term. The terms which include the highest power are dominant for cases where $(1 - M_r) \to 0$.

As aforementioned, the equation will be implemented in the computational analysis elaborating the integrals as discrete sums while derivatives are calculated using differential equations. The terms in the Formulation 1A are evaluated at the retarded/source time, as denoted by the ret subscript in each integral. The integrals are obtained by summing the contributions of all the sources/nodes on the acoustic data surface at a particular observer time.

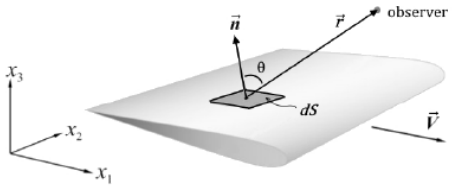

Figure 2.10: Farassat 1A formulation surface representation, from [55]

2.5.3 Fast Fourier Transforms (FFT) and Inverse FFT

To analyse and manipulate the information contained in a signal is necessary a manual or mechanical operation called signal processing. In this case a signal is considered as an evolution of a phenomenon over time or space, which can be continuous or discrete, as illustrated in the figure 2.11.

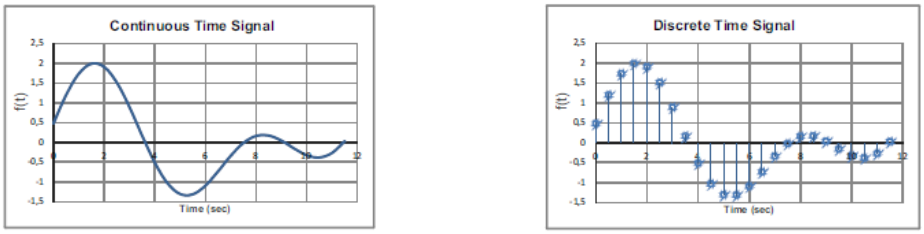

Figure 2.11: Continuous-time signal and Discrete-time signal

A signal contains one or more frequencies, and it can be considered in the time domain (how a signal changes over time) or in the frequency domain (how much of the signal lies within each frequency band); the conversion from time domain to the frequency domain is usually done using the Fourier Transform. In this study case, the signal is the acoustic pressure sampled over a finite time interval, so, it will be used a Discrete Fourier Transform (DFT),that can be defined as:

$$X_p = \sum_{n=0}^{N-1} x_n e^{-j\frac{2\pi}{N}np} \qquad , p \in 0, 1, ..., N-1 \tag{2.71}$$

Where, N is the number of samples in time history, x is the discrete signal in the time domain and X is the signal in the frequency domain. Here, a sequence of N numbers $x_0, x_1, ..., x_{N-1}$ is transformed into a N-periodic sequence of complex numbers $X_0, X_1, ..., X_{N-1}$. Through this formulation the number of operation necessary to compute the Fourier transformation is in the order of N^2. For this reason, this computational cost can be adequate for a small number of points, but when the signal contains a larger number of elements it is necessary to adopt another method: Fastest Fourier Transform (FFT). This latter was presented by Cooley and Tukey in 1965 [56] as an alternative to the classical method. The FFT is an efficient algorithm for computing the DFT, in fact it only requires $N\log_2(N)$ arithmetic operations, instead of the previous N^2, which is an obvious advantage. Moreover, thanks to the lower number of computations and, so, less round-off error the FFT results to be more precise. The basic idea of this algorithm is the realization of DFT for a sequence of N points as two DFT of length $N/2$. In this way the summation of the expression 2.71 is divided in two parts: one for the even n and another for odd n.

$$\begin{aligned} X_p &= \sum_{n=0}^{\frac{N}{2}-1} x_{2n} e^{-j\frac{2\pi}{N}(2n)p} + \sum_{n=0}^{\frac{N}{2}-1} x_{2n+1} e^{-j\frac{2\pi}{N}(2n+1)p} \\ &= \sum_{n=0}^{\frac{N}{2}-1} x_{2n} e^{-j\frac{2\pi}{(N/2)}np} + \sum_{n=0}^{\frac{N}{2}-1} x_{2n+1} e^{-j\frac{2\pi}{(N/2)}np} \\ &= A_p + W^p B_p \end{aligned} \tag{2.72}$$

Where:

$$A_p = \sum_{n=0}^{\frac{N}{2}-1} x_{2n} e^{-j\frac{2\pi}{(N/2)}np} \tag{2.73}$$

$$B_p = \sum_{n=0}^{\frac{N}{2}-1} x_{2n+1} e^{-j\frac{2\pi}{(N/2)}np} \tag{2.74}$$

$$W^p = e^{-j\frac{2\pi}{N}} \tag{2.75}$$

A_p and B_p are themselves DFTs with length $N/2$: A_p is the DFT of a sequence $\{x_{2n}\} = \{x_0, x_2, ..., x_{N-4}, x_{N-2}\}$ and B_p of $\{x_{2n+1}\} = \{x_1, x_3, ..., x_{N-3}, x_{N-1}\}$. Due to the periodicity properties, the outputs for $N/2 \leq p < N$ are identical to the outputs of $0 \leq p < N/2$, hence it is only necessary to compute $N/2$ outputs.

In conclusion, it is possible to declare that the FFT is an recursive algorithm that rearranges the problem into two simpler problems with half the size. In particular, the FFT library, that PSU-WOPWOP uses, is a package called FFTW (Fastest Fourier Transform in the West). When is sent a 1-D array of real numbers, x, this library returns a 1-D aray of complex numbers, X, according to the equations 2.76-2.78.

$$X_p = \sum_{n=1}^{N} x_n e^{-j2\pi \frac{np}{N}} \qquad 2 \leq p \leq \frac{N}{2} \tag{2.76}$$

$$X_1 = \sum_{n=1}^{N} x_n \tag{2.77}$$

$$X_{N/2+1} = \sum_{n=1}^{N} x_n e^{-j\pi n} \tag{2.78}$$

The default minimum frequency in a spectrum created by FFTW is equal to zero. The successive bins are then equally spaced by Δf. The corresponding maximum frequency is known as Nyquist frequency and is equal to $N/2\Delta f$. The Nyquist frequency is the highest frequency bin in a spectrum needed to fully recreate the original signal. Therefore, the FFTW discards all the frequencies values above the Nyquist frequency from X_p without losing any required data. Notice the result of FFTW produces a real result in the fisrt frequency bin.

The result of FFTW is used to calculate a complex pressure at each frequency bin according to the equations 2.79 and 2.80.

$$(P_c)_p = X_p \frac{2\Delta t}{T} \qquad 2 \leq p \leq \frac{N}{2} + 1 \tag{2.79}$$

$$(P_c)_1 = X_1 \frac{2\Delta t}{T} \qquad 1 \leq p \leq \frac{N}{2} + 1 \tag{2.80}$$

The subscript p in equation 2.79 indicates that this quantity must be calculated for each p_{th} point of the FFTW result. The real number and imaginary arts of any $(P_c)_p$ are used to calculate the mean-square pressure and phase in the p_{th} frequency bin. The units of complex pressure is Pascals.

2.5.4 Sound Pressure Levels (SPL)

The very small fluctuation in atmospheric pressure of the sound waves are the sources of noise received by human ear. The sound pressure is measured in a logarithmic scale called the decibel (dB) scale; this latter is defined by comparing sounds to a reference pressure of $P_0 = 20 \times 10^{-6} N/m^2$, value assigned to a SPL of 0.0 dB. SPL can be evaluated for individual frequency bins, a specific frequency range, octave bands, or for an entire spectrum.

The first value needed to calculate any sound pressure level is the mean-square pressure of the signal in the desired range :

$$\left[\bar{p}^2\right] = \frac{1}{2} \sum_{p} |(P_c)_p|^2 \tag{2.81}$$

for every p_{th} bin contained in the frequency range. The units of equation 2.81 are $\left[Pa^2\right]$ if it is calculated from a pressure time history. The mean-square pressure is found for every frequency range.
The corresponding SPL in dB is computed by:

$$SPL(dB) = 10\log_{10}\left[\frac{\left[p^2\right]}{(20\times10^{-6})^2}\right] \tag{2.82}$$

Each frequency range, either an octave band or an entire spectrum has a single SPL value associated with it. If the entire spectrum is sampled, the SPL returned is the overall sound pressure level (OASPL).

However, the level of generated noise is subjective, so it is necessary to take into account the human ear, which is more sensitive in the range from 1 kHz to 5 kHz. To overcome this problem A-weighting decibel (dBA) was created, whose correction can be applied to all the individual SPLs and OASPL.

$$\mathcal{W}_{A_m} = \frac{\mathcal{W}_{C_m}K_3 f_m^4}{(f_m^2+f_2^2)(f_m^2+f_3^2)} \tag{2.83}$$

$$\mathcal{W}_{C_m} = \frac{K_1 f_m^4}{(f_m^2+f_1^2)^2(f_m^2+f_4^2)^2} \tag{2.84}$$

Notice that $\mathcal{W}_A$ incorporates $\mathcal{W}_C$. f_m is the frequency which the weighting is calculated for. The constants are:

$$K_1 = 2.243\times10^{16}s^{-4}$$

$$K_3 = 1.562$$

$$f_1 = 20.599Hz$$

$$f_2 = 107.653Hz$$

$$f_3 = 737.862Hz$$

$$f_4 = 12194.220Hz$$

A-weighted sound pressure levels is the most common type of weighting. The A-weighted mean-square pressure, and the resulting A-weighted SPL (dBA) are calculated as follows:

$$\left[\bar{p}^2\right]_A = \frac{1}{2}\sum_m (\mathcal{W}_A)_m |(P_c)_p|^2 \tag{2.85}$$

$$SPL(dBA) = 10\log_{10}\left[\frac{\left[\bar{p}^2\right]_A}{(20\times10^{-6})^2}\right] \tag{2.86}$$

2.5.5 Octave Bands

It is important to specify the need of the division of the frequency range into a set of frequencies, denominated bands due to the impracticability to analyze the signal frequency by frequency. Each one of those bands covers a range of frequencies, creating a scale of octave or one-third octave bands. It is possible to divide the frequency range in two ways: in constant absolute bandwidth bands or in constant relative bandwidth bands. The first way divides the spectrum continuum in bands whose frequency

range is constant for all bands; this method is the least used. While, constant relative bandwidth bands separation of the spectrum is an appropriate way to present the frequency distribution of the signal because it results to be easier to interpret thanks to the linear distribution in the logarithmic scale [57]. An octave band is a specific frequency range in a spectrum, and a sound pressure level can be calculated for any octave band in a spectrum. PSU-WOPWOP uses a base-2 scheme of octave band filtering. Each octave band is characterized by a low frequency limit f_{LL}, a center frequency f_c, and an high frequency limit f_{HL}. The lowest octave band in a spectrum covers the smallest range of frequencies, and the highest band covers the largest range. Each successive octave band is larger than the one preceding it. Center frequencies are found by the following method for any 1/N octave filter:

$$(f_c)_i = 1000.0 \cdot R^{i/N} \tag{2.87}$$

$(f_c)_i$ is the center frequency of the i_{th} octave band and i is an integer representing the octave band number.

When $i = 0$, $f_0 = 1.0kHz$, which is the reference frequency. For frequencies below the reference frequency, i is negative. For frequencies above the reference frequency, i is positive. The value of R depends on whether or not the user requests PSU-WOPWOP to approximate the octave band center frequencies to more rounded numbers.

$$\begin{aligned} If \quad octaveApproxFlag = .true., \quad R = 2(10^{0.3} \approx 2) \\ If \quad octaveApproxFlag = .false., \quad R = 10^{0.3} = 1.9953 \end{aligned}$$

In PSU-WOPWOP, the default value of the approximation flag is set equal to true; then, the upper and lower limits for each band are found by:

$$\begin{aligned} f_{LL} &= \frac{f_c}{factor} \\ f_{HL} &= f_c \cdot factor \\ factor &= R^{1/(2N)} \end{aligned}$$

The default value of N in PSU-WOPWOP is set equal to 3 in order to divide each octave band into three bands again with equal bandwidth. The full table of the $1/3$ octave bands frequencies is given in Appendix A.

2.5.6 Computational Algorithms

The integrals in the equations 2.69 and 2.70 have to be calculated using a numerical algorithm. As already mentioned before, the Formulation 1A of Farassat is referred to retarded-time; considering the generic retarded-time formulation for the wave equation:

$$4\pi p'(x,t) = \int_{f=0} \left[\frac{Q(y,\tau)}{r\,|1 - M_r|} \right]_{ret} dS \tag{2.88}$$

where r, M_r and S are defined previously, the condition $f = 0$ describes the integration surface and Q is a known source strength described as a function of the source's position y and the retarded time τ. This integral is solved numerically using one of these methods: Mid-panel Quadrature, High-Accurancy Quadrature or Source Time-Dominant Algorithm [58]. In these first two methods the observer time is set and from it the retarded time is obtained through the already known expression $\tau = t - r/c$. The second method is a refinement of the Mid-panel Quadrature method, since the evaluation of the integral at the panel center is replaced with more points, but at the same time the computational cost increases. Moreover, since the source function Q is only known at discrete emission times this implies that the input surface data must be interpolated. An alternative to these methods is the selection of the source time and the correspondent observer time is computed for each source panel and the result is one observer reception time for each panel and for every emission time; this latter method is the Source Time-Dominant Algorithm. In this case, the retarded time is known in advance and so the interpolations of the input data are avoided; for this reason, it was chosen as the method to solve the retarded time integral. In order to obtain the signal in the time domain, all panel pressure contributions must be summed, doing this process all the pressure values have to be interpolated at the same observer times:

$$4\pi p'(x,t^*) \approx \sum_{i=1}^{N} I[K_i(t), t^*] \tag{2.89}$$

Where t is the travel time of a sound from one source to the observer, $I[\cdot, t^*]$ is the interpolation operator to one time t^*, that is the desired observer time determined by the choice of y_i and τ. $K_i(t)$ is the contribution from panel i, which is calculated by approximating the integral in equation 2.88:

$$K_i(t) = \frac{Q(y_i,\tau)}{r_i\,|1 - M_r|_i} \Delta S_i \tag{2.90}$$

2.5.7 PSU-WOPWOP Structure

The core of PSU-WOPWOP is an object called "patch" which stores the surface geometry and flow data for a single surface. Fundamentally, any surface which generates noise is modeled by a discrete number of panels over which the integration quantities are assumed constant. At their most basic, each patch stores a grid representing the integration surface and the necessary data at each of the grid points. Each patch can store many different types of data: chordwise-compact loading vectors, surface loading vectors, surface

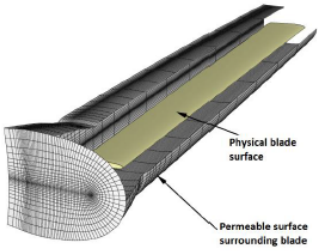

Figure 2.12: A cut-away view of a permeable acoustic data surface surrounding a helicopter rotor blade, from [59]

pressure, permeable surface data (for high-speed impulsive noise prediction), etc. At a minimum a patch must store some type of surface geometry to enable the calculation of thickness noise, which requires the position, normal vector, and associated area of each point on a patch at each time. The next level of complexity is to include the surface pressure as well, enabling the calculation of the loading noise.

As aforementioned in the previous sections, the quadrupole source term is absent from Formulation 1A; the reasons are the following:

- The volume integral necessary to compute the term is computationally demanding;
- The quadrupole contribution can be captured through manipulation of the terms found in Formulation 1A.

Mathematically, there is no reason why a quadrupole term is needed. The acoustic analogies made by Lighthill describe the influence of acoustic sources using source distributions equivalent to the real sources, but not necessarily identical. The influence of the quadrupole term can be captured by the monopole and dipole terms if the boundaries of the ADS surround the volume in which the quadrupole acts. The boundaries of such an ADS are permeable, with a non-zero normal flow velocity on its surface. A model of acoustic data surface is shown in figure 2.12.

A permeable ADS allow to eliminate the need to take volume integrals, which are necessary to compute the quadrupole term, but, at the same time, it involves an higher computational cost in order to allocate all the acoustic sources inside the ADS and study the flow field accurately (including the acoustic propagation) outside to the ADS.

2.5.8 PSU-WOPWOP Observers

Observers represent microphone or listener positions: they store and post-process the data calculated by patches. Observers can be specified in several different ways in PSU-WOPWOP, and there is no limit to the number of observers a case can have. So, Observers are responsible for storing and post-processing the pressure time-histories calculated by the patches. The integration process begins with a loop over the observers, then over the patches stored in the container tree. At each patch, a loop over the source time begins. For each source time and each point on the integration surface, patch coordinates with the observer to determine the observer location and the observer time corresponding to the source position and time. The incremental contribution to the noise from a particular source point at a particular observer location is placed in an array within the observer object. As each point from each patch is calculated an acoustic pressure time history is built by summing up the individual contributions. This is done by forming an array of observer time and integrand pairs for each point. The observer times in this array do not, in general, correspond to the desired observer times, so the data is then linearly interpolated onto the final observer time array as it is summed. Once the contributions from all patches have been summed for that observer the process repeats for the next observer, continuing until a pressure time-history has been calculated for each observer location. Once the integration is complete the

post-processing routines are called for each observer. This may be as simple as writing a single acoustic pressure time history to a file, or as complex as a Fast Fourier Transform to calculate the Overall Sound Pressure Level, any octave filtered spectrum, or some other complicated noise metric. The results can be output at individual observer locations or on a grid of observers. The observers can also output phase and decibel amplitude plots at individual points, or on entire grids of observer locations [53].

2.6 Brooks, Pope and Marcolini (BPM)

This model was developed by Brooks Pope and Marcolini in 1989 for the prediction of the self-generated noise of an airfoil blade encountering smooth flow. Prediction methods for individual self-noise mechanisms are semi-empirical and are based on previous theoretical studies and the most comprehensive self-noise data set available. The BPM model includes five self-noise mechanisms for airfoil immersed in a flow due to the specific boundary-layer phenomena: boundary-layer turbulence passing the trailing edge (TBL-TE), separated-boundary-layer and stalled-airflow flow, vortex shedding due to laminar-boundary-layer instabilities, vortex shedding from blunt trailing edges, and the turbulent vortex flow existing near the tips of lifting blades. The predictions are matched with the data base from NACA 0012 airfoil blade sections of different sizes (chords from 2.5 to 61 cm) tested at wind tunnel speed up to Mach 0.21 (Reynolds number based on chord up to $3 \cdot 10^6$) and at angles of attack from 0° to 25.2° [60].

2.6.1 Turbulent Boundary Layer – Trailing Edge

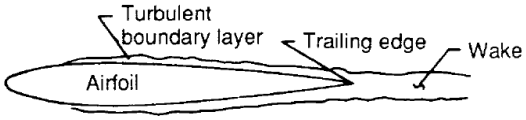

Figure 2.13: Turbulent-boundary-layer-trailing-edge noise, from [61]

Airfoils immersed in a flow develop a boundary layer that can be turbulent at high Reynolds number, as shown in figure 2.13; when this turbulence passes over the trailing edge, noise is generated. This latter is called TBL-TE in [61] and it is a relevant source of aeroacoustics noise. The SPL of the TBL-TE noise in the BPM model is made from three contributions:

$$SPL_{TBL-TE} = 10\log_{10}\left(10^{\frac{SPL_p}{10}} + 10^{\frac{SPL_s}{10}} + 10^{\frac{SPL_\alpha}{10}}\right) \tag{2.91}$$

where the subscript p, s and α refer to the contributions of pressure side, suction side and angle of attack, respectively. The equations that describe the three contributions (SPL_p, SPL_s and SPL_α) are studied in detail in section $5.1.2$ of document [61], and are just summarized here.

For the cases of $\alpha \leq \alpha_*$:

$$SPL_p = 10\log_{10}\left(\frac{\delta_p^* M^5 d\bar{D}_h}{r_e^2}\right) + A(\frac{St_p}{St_1}) + (K_1 - 3) + \Delta K_1 \tag{2.92}$$

$$SPL_s = 10\log_{10}\left(\frac{\delta_s^* M^5 d\bar{D}_h}{r_e^2}\right) + A(\frac{St_s}{St_1}) + (K_1 - 3) \tag{2.93}$$

$$SPL_\alpha = 10\log_{10}\left(\frac{\delta_s^* M^5 d\bar{D}_h}{r_e^2}\right) + B(\frac{St_s}{St_2}) + K_2 \tag{2.94}$$

and for cases of $\alpha \geq \alpha_*$:

$$SPL_p = -\infty \tag{2.95}$$

$$SPL_s = -\infty \tag{2.96}$$

$$SPL_\alpha = 10\log_{10}\left(\frac{\delta_s^* M^5 d\bar{D}_h}{r_e^2}\right) + A'(\frac{St_s}{St_2}) + K_2 \tag{2.97}$$

where δ^* is the boundary layer displacement thickness on either side of the airfoil, St is the Strouhal number based on δ^*, r_e is the effective observer distance, α_* is the stall angle of attack, and A, A', B, ΔK_1, K_1 and K_2 are empirical functions based on St.

As it is possible to see from equation 2.97 when the angle of attack (α) is above the stall point, the angle-of-attack contribution is different and in the same way also SPL_p and SPL_s are set equal to $-\infty$.

2.6.2 Laminar Boundary Layer – Vortex Shedding

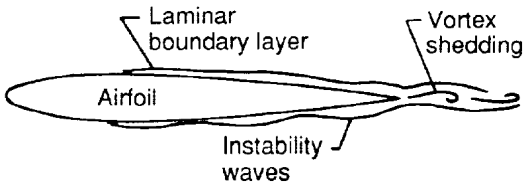

Figure 2.14: Laminar-boundary-layer-vortex-shedding noise, from [61]

Another source of self-noise included in the BPM model is the noise generated by a feedback loop between vortices being shed at the trailing edge and instability waves in the laminar boundary layer, as illustrated in figure 2.14. This noise occurs when the boundary layer of the airfoil remains laminar. The formula used to estimate the noise spectrum in a one-third-octave presentation is:

$$SPL_{LBL-VS} = 10\log_{10}\left(\frac{\delta_p^* M^5 d\bar{D}_h}{r_e^2}\right) + G_1\left(\frac{St'}{St'_{peak}}\right) + G_2\left[\frac{Re_c}{(Re_c)_0}\right] + G_3(\alpha_*) \tag{2.98}$$

where G represents empirical functions, in particular G_1 is the contribution to self-noise one-third-octave spectra, G_2 specifies the curve shape and G_3 is defined as $G_3(\alpha_*) = 171.0 - 3.03\alpha_*$. St'_{peak} is the peak of Strouhal number function of Re_c, which is the Reynolds number at chord, c_i. The subscript 0 refers to a reference Reynolds number that is function of the angle of attack [61].

2.6.3 Tip Vortex

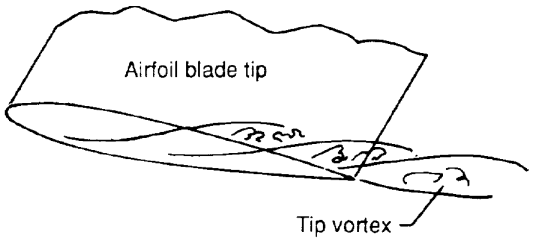

Figure 2.15: Tip vortex formation noise, from [61]

The vortices generated at blade tips are another source of noise predicted by BPM. This source of noise is illustrated in figure 2.15. The sound pressure level is estimated as:

$$SPL_{Tip} = 10\log_{10}\left(\frac{M^2 M_{max}^2 l^2 \bar{D}_h}{r_e^2}\right) - 30.5(\log_{10} St" + 0.3)^2 + 126 \tag{2.99}$$

where $M_{max} = M_{max}(\alpha_{tip})$ is the maximum Mach number measured near the blade tip within the separated flow region that is assumed to depend on α_{tip}, which is the angle of attack at the tip; l is the spanwise extent of the separation one; $St"$ is the Strouhal number based on l. For a round shape of the tip, l is estimated as $l = c_i 0.008\alpha_{tip}$. Anyway, α_{tip} is not a reliable output of standard aeroelastic models and the impossibility to determine α_{tip} weakens the formulation of the tip vortex noise [60].

2.6.4 Trailing-Edge Bluntness – Vortex Shedding

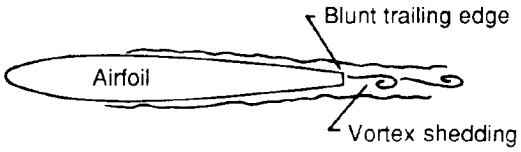

Figure 2.16: Trailing-edge-bluntness-vortex-shedding noise, from [61]

The frequency and amplitude of this noise source depends on the geometry of the trailing edge and is typically characterized by a tonal nature. This source is llustuted in figure 2.16. The adoption of flatback and truncated airfoils far outboard along the blade could strengthen this noise source. In order to predict this noise source is necessary to know the distribution along the blade span of the blunt thickness of the trailing edge, h, and the solid angle between the suction and pressure sides of the airfoil, Ψ, as shown in figure 2.17. The BPM solver is very sensitive to these two parameters, which, however, are often not easily evaluable [60].

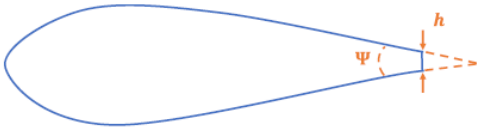

Figure 2.17: Geometric parameters Ψ and h the trailing-edge bluntness, from [60]

h and Ψ are inputs to the following equation describing this noise source:

$$SPL_{TBE-VS} = 10log_{10}\left(\frac{\delta_p^* M^5 d\bar{D}_h}{r_e^2}\right) + G_4\left(\frac{h}{\delta_{avg}^*}, \Psi\right) + G_5\left(\frac{h}{\delta_{avg}^*}, \Psi, \frac{St"}{St"_{peak}}\right) \tag{2.100}$$

δ_{avg}^* is the average displacement thickness for both sides of the airfoil.

2.6.5 Directivity

The directivity term, $\bar{D}$, corrects the SPL depending on the relative position of the observer to the source of the noise. The position is described by the spanwise directivity angle, Φ_e, and by the chordwise directivity angle, Θ_e, which are schematically represented in figure 2.18.

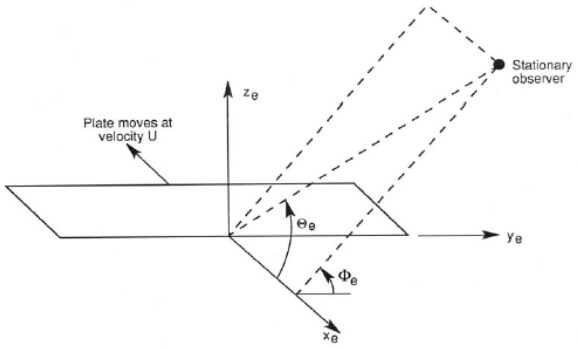

Figure 2.18: Angles used in the directivity function, from [61]

Moreover, they can be defined as follow:

$$\Phi_e = atan\left(\frac{z_e}{y_e}\right) \tag{2.101}$$

$$\Psi_e = atan\left(\frac{y_e \cdot cos(\Psi_e) + z_e \cdot sin(\Psi_e)}{x_e}\right) \tag{2.102}$$

Given the angles Θ_e and Φ_e, at high frequency, $\bar{D}$ takes the expression:

$$\bar{D}_h(\Theta_e, \Phi_e) = \frac{2sin^2\left(\frac{\Theta_e}{2}\right)sin^2\Psi_e}{(1 + Mcos\Theta_e)(1 + (M - M_c)cos\Theta_e)^2} \tag{2.103}$$

where M_c represents the Mach number past the trailing edge. At low frequency the equation is expressed as:

$$\bar{D}_l(\Theta_e, \Phi_e) = \frac{sin^2\Theta_e sin^2\Psi_e}{(1 + Mcos\Theta_e)^4} \tag{2.104}$$

2.6.6 A-Weighting

As already seen in the theory of PSU-WOPWOP 2.5.4, also for the BPM it is possible to evaluate the aeroacoustics outputs by A-weighted. The A-weight, $A_{\mathcal{W}}$, is computed as:

$$A_{\mathcal{W}} = \frac{10\log\left(1.562339\frac{f^4}{(f^2+107.65265^2)(f^2+737.86223^2)}\right)}{\log 10} + \frac{10\log\left(2.422881e16\frac{f^4}{(f^2+20.598997^2)^2(f^2+12194.22^2)^2}\right)}{\log 10} \tag{2.105}$$

The A-weighted is a function of frequency and is added to the values of sound pressure levels:

$$SPL_{A_{\mathcal{W}}} = SPL + A_{\mathcal{W}} \tag{2.106}$$

Chapter 3

Implementation

This chapter will be dedicated to the description of the software, developed in Julia language, used for the aerodynamic and noise prediction. As aforementioned in the previous section 2.2, the process is divided in steps, as observed in figure 3.1.

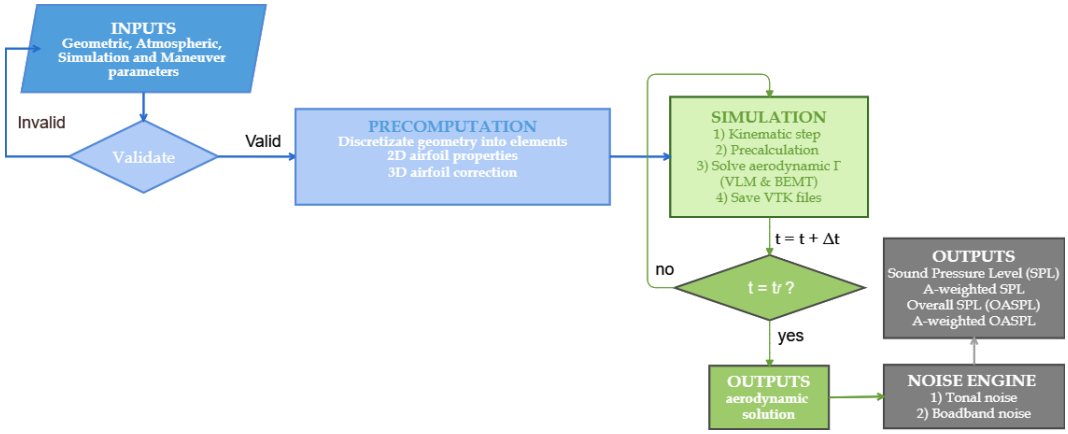

Figure 3.1: Computation diagram of FLOWUnsteady engine

Before plunging in the simulation steps, it is necessary to model and re-create the geometry that is studied in FLOWUnsteady, that uses spatial state variables. The generation of the 3D model requests different inputs from the user; that will be analysed in following section.

3.1 Inputs

The objective of this section is to provide information about the input data that a hypothetical user have to introduce in the program; for doing that it will be considered a hypothetical case of a single rotor study. The geometry input specifications are defined through comma separated value (CSV) files that describe the airfoil, blade and rotor characteristics. CSV is simple format for representing a rectangular array (matrix) of numeric and textual values separated by a delimiter, which acts as a database table or a intermediate form of a database table. Each line should contain the same number of fields. An optional

header line may appear as the first line of the file with the same format as normal record lines. This header will contain names corresponding to the fields in the file and should contain the same number of fields as the records in the rest of the file. CSV commonly employs US-ASCII as character set, but other character sets are permitted. In other words, a CSV file is a set of database rows and columns stored in a text file such that the rows are separated by a new line while the columns are separated by a semicolon or a comma. A CSV file is primarily used to transport data between two databases of different formats through a computer program.

An example of CSV file used in this research is shown in figure 3.2.

property	file	description
Rtip	0.12	(m) Radius of blade tip
Rhub	0.00624	(m) Radius of hub
B	2	Number of blades
blade	DJI9443_blade.csv	Blade file

Figure 3.2: Example of DJI 9443 CSV file used to describe a rotor model

For a whole definition of the geometry it is necessary a precise description of the structure. Taking into account the case of a single rotor model, it is request to the user to define as input the number of blades, radius of the tip and hub, chord distribution, pitch distribution, height of the leading edge with respect to the top face of the hub, sweep distribution, and the airfoil distribution from the root to the tip of the single blade. Together with the CSV geometric parameters, the hypothetical user is request to define atmospheric parameters (density, air dynamic viscosity, speed of sound and the free-stream velocity) , simulation parameters (number of lattice elements, number of revolutions in the simulation, number of steps for each revolution, total time) and maneuver parameters (RPM trend, angle of tilting systems trend, velocity and angles of the whole vehicle trend).

3.2 Precomputation

These files and all the linked ones establish the input used by the software for realizing the three-dimensional geometry that will be studied. The figure 3.3 illustrates how the CSV file defined is used.

```
# ------------ PARAMETERS --------------------------------------------------
# Rotor geometry
rotor_file      = "DJI9443.csv"        # Rotor geometry
data_path       = uns.def_data_path    # Path to rotor database
pitch           = 0.0                  # (deg) collective pitch of blades
n               = 50                   # Number of blade elements
CW              = true                 # Clock-wise rotation
xfoil           = true                 # Whether to run XFOIL
```

Figure 3.3: Example of DJI9443 CSV file used as an input for the FLOWUnsteady three-dimensional geometry

The characteristics handled in the defined CSV files are used by the software XFoil, a 2D simulation code based on panel method developed by Mark Drela in MIT, in order to precompute the two-dimensional aerodynamic characteristics of each blade element at the corresponding local Reyolds number (considering rotational and freestream velocity) [62]. Subsequently, a Prandtl-Glauert compressibility

correction is applied to lift curves, capturing compressibility effects. Both lift and drag curves are then treated to capture three-dimensional drag and stall-delay effects encountered in rotor blades [63] and the Viterna method [64] is applied to obtain post-stall $\pm 180^{\circ}$ extrapolations of these curves [65]. Moreover, following the different distribution defined in the CSV files, FLOWUnsteady is able to create the 3D geometry and generate the Vortex Lattice Method model, where each blade will be discretized into n horseshoes, as already seen in the section 2.4. FLOWUnsteady uses the generated three-dimensional geometry of the vehicle as spatial state variables (referred as G), along with the velocity of the vehicle V and angular velocity ω [66]. At this point the elements created are grouped into a system that defines the whole vehicle; in the case taken into consideration the vehicle is define by the single rotor, however it can be composed by wings and rotors. In this study, each blade of the propeller is modeled as a rotary lifting surface where the physics of interest have been broken down into three aspects: load distribution, blade-induced velocity, and wake-induced velocity. The load distribution is calculated through BEM theory and used for deriving the circulation along a vortex lattice representing the lifting surface. In turn, the vortex lattice is used as a framework for manipulating the rotating geometry, calculating the direction and strength of vortex particles being shed off the trailing edge, and calculating the velocity that the lifting surface induces on nearby particles. Since the vehicle is defined using just BEM theory and VLM, the wakes are assume quasi-steady. This means that at every time step of the simulation the wakes of VLM models are represented as rigid, semi-infinite filaments as represented in figure 3.4, and wakes of BEM models are obtained from a conservation of momentum assumptions. This quasi-steady approach allows to consider VLM-on-VLM and VLM-on-BEM wake interaction. A quasi-steady solver assumes that perturbations at the source of a wake-shedding surface immediately affect the entirety of the wake. Therefore, wings are solved with the vortex lattice method while shedding a rigid semi-infinite wake. Rotors are solved through blade element momentum theory, without attempting to model the effects of wake interactions.

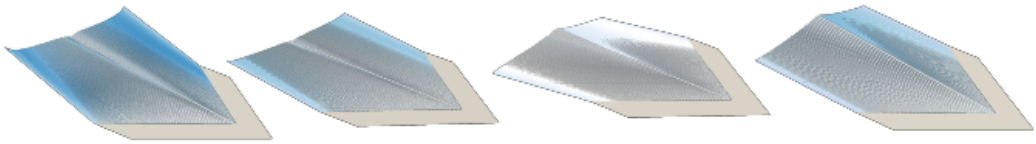

Figure 3.4: Heaving wing simulation with quasi-steady solver

After the creation and discretization of the vehicle, the maneuver inputs, defined by the user, are implemented in order to create the maneuver desired that will be analysed during the simulation. The default maneuver used by FLOWUnsteady is kinematic, which means that RPM of the rotor system, angles of tilting systems, velocity and angles of the whole vehicle are defined through a function in time. In order to give the possibility at the hypothetical user to implement a dynamic maneuver a colleague of mine and I worked on the realization of a module in Julia language, that will be described in the next section.

3.3 Dynamic Maneuver

In order to discuss about the dynamic maneuver implementation a quadcopter model with rotors arranged at the corners of a square body will be taken into consideration. This quadcopter will operate into two frames: the inertial frame and the body frame. The inertial frame is defined by the ground, since it is solidary with the Earth, with the gravity pointing in negative z direction. The body frame is defined by the orientation of the quadcopter, with the rotor axis pointing in the positive z direction and the arms pointing in x and y directions, as it is shown in figure 3.5.

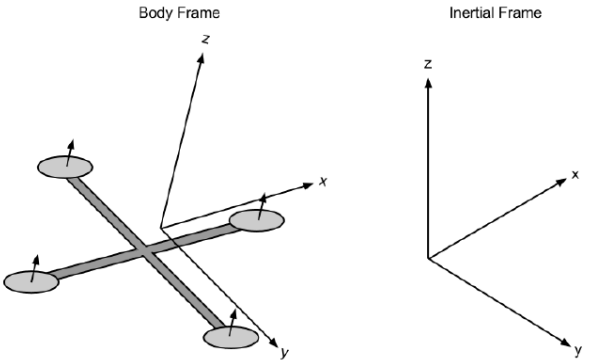

Figure 3.5: Quadcopter Body and Inertial frame

Before delving into the physics of the motion of quadcopter, it is necessary to define the position and the velocity of the model in the inertial and body frames, and the relation between them. In the inertial frame the position and the velocity are defined as $x = (x, y, z)^T$, $\dot{x} = (\dot{x}, \dot{y}, \dot{z})^T$, respectively. Similarly, the roll, pitch, and yaw angles are defined in the body frame as $\theta = (\phi, \Theta, \psi)^T$, with corresponding angular velocities equal to $\dot{\theta} = (\dot{\phi}, \dot{\theta}, \dot{\psi})^T$. However, the angular velocity, ω, is different from $\dot{\theta}$ because ω is a vector pointing along the axis of rotation, while $\dot{\theta}$ is just the time derivative of roll, pith and yaw angles. For converting the angular velocities into the angular velocity vector, the following relation is defined:

$$\omega = \begin{bmatrix} 1 & 0 & -sin\theta \\ 0 & cos\phi & cos\theta sin\phi \\ 0 & -sin\phi & cos\theta sin\phi \end{bmatrix} \dot{\theta} \tag{3.1}$$

where ω is defined in the body frame. As already done for the angular velocities, it is possible to relate the body and the inertial frames by a rotation matrix, R, which allows to go from the body frame to inertial frame [67].

$$R = \begin{bmatrix} cos\phi cos\psi - cos\theta sin\phi sin\psi & -cos\psi sin\phi - cos\phi cos\theta sin\psi & sin\theta \sin\psi \\ cos\theta cos\psi sin\psi + cos\phi sin\psi & cos\phi cos\theta cos\psi - sin\phi sin\psi & -cos\psi sin\theta \\ sin\phi sin\theta & cos\phi sin\theta & cos\theta \end{bmatrix} \tag{3.2}$$

So, for a generic given vector $\vec{V}$ in the body frame, the corresponding vector in the inertial frame is given by $R\vec{V}$.

This developed dynamic code is merged with FLOWUnsteady code to use the forces and torques that are elaborated by applying BEMT and VLM to the model during the simulation. Moreover, it is necessary to take into consideration that adjacent propellers are rotated in opposite direction, i.e.: if a propeller is spinning clockwise, then the other two adjacent ones will be spinning counter-clockwise. In this module, several advanced effects that contribute to the highly nonlinear dynamics of quadcopter have been ignored: the rotational drag forces (our rotational velocities are relatively low), blade flapping (since the blades are considered rigid elements and not made of flexible materials) and the surrounding fluid velocities (wind speed) is ignored since it is considered low. With these considerations it is now possible to write out the dynamics of the quadcopter [67].

3.3.1 Equations of Motion

In the inertial frame, the acceleration of quadcopter is due to the thrust vector (T_B), gravity (g), and linear friction (F_D). As aforementioned, thanks to the merging with the FLOWUnsteady code, the thrust and linear friction are given by BEM theory and VLM implementation. For this reason, it is just necessary to apply the rotation matrix, R, in order to map the thrust from the body frame to the inertial frame. Hence, the linear motion can be summarized as

$$m\ddot{x} = \begin{bmatrix} 0 \\ 0 \\ -mg \end{bmatrix} + RT_B + F_D \tag{3.3}$$

where $\ddot{x}$ is the acceleration of the quadcopter and m is equal to the total mass of the model. While it is more convenient to have the linear equations of motion in the inertial frame, the rotational equation is useful in the body frame, such that it is possible to express rotations about the center of the quadcopter instead of about its inertial center. The rotational equation of motion is derived from the Euler's equations for rigid body dynamics. These Euler's equations are expressed in vector form

$$I\dot{\omega} + \omega \times (I\omega) = \tau \tag{3.4}$$

where ω, as already mentioned, is the angular velocity vector, I is the inertia matrix of the vehicle, and τ is a vector of external torques. It is possible to rewrite this equation as

$$\dot{\omega} = \begin{bmatrix} \dot{\omega_x} \\ \dot{\omega_y} \\ \dot{\omega_z} \end{bmatrix} = I^{-1}(\tau - \omega \times (I\omega)) \tag{3.5}$$

Modelling the quadcopter as two thin uniform rods crossed at the origin with a point mass (motor) at the end of each, it is clear that the inertia matrix has the following structure:

$$I = \begin{bmatrix} I_{xx} & 0 & 0 \\ 0 & I_{yy} & 0 \\ 0 & 0 & I_{zz} \end{bmatrix} \tag{3.6}$$

Therefore, it is possible to get the final result for the body frame rotational equations of motion:

$$\dot{\omega} = \begin{bmatrix} \tau_\phi I_{xx}^{-1} \\ \tau_\theta I_{yy}^{-1} \\ \tau_\psi I_{zz}^{-1} \end{bmatrix} - \begin{bmatrix} \frac{I_{yy}-I_{zz}}{I_{xx}} \omega_y \omega_z \\ \frac{I_{zz}-I_{xx}}{I_{yy}} \omega_x \omega_z \\ \frac{I_{xx}-I_{yy}}{I_{zz}} \omega_x \omega_y \end{bmatrix} \tag{3.7}$$

Knowing the value of $\dot{\omega}$ it is possible to elaborate the angular velocity vector ω and consequently the angular velocity θ through the relation defined in equation (3.1). Thanks to the equation (3.3) the acceleration vector $\ddot{x}$ is defined, so the velocity vector is calculated as $\dot{x} = \dot{x}_{prev} + dt \cdot \ddot{x}$, where dt is the time step, and $\dot{x}_{prev}$ is the previous value of the velocity vector; and through $\dot{x}$ is possible to compute the position of the quadcopter in each time step.

In figure 3.6 is shown an application of the dynamic code for a double rotor vehicle in its vertical climb movement. In this way, the hypothetical user can select the values of the RPMs with respect to time and the equations of motion, as already aforementioned, are used to obtain the position trend of the vehicle.

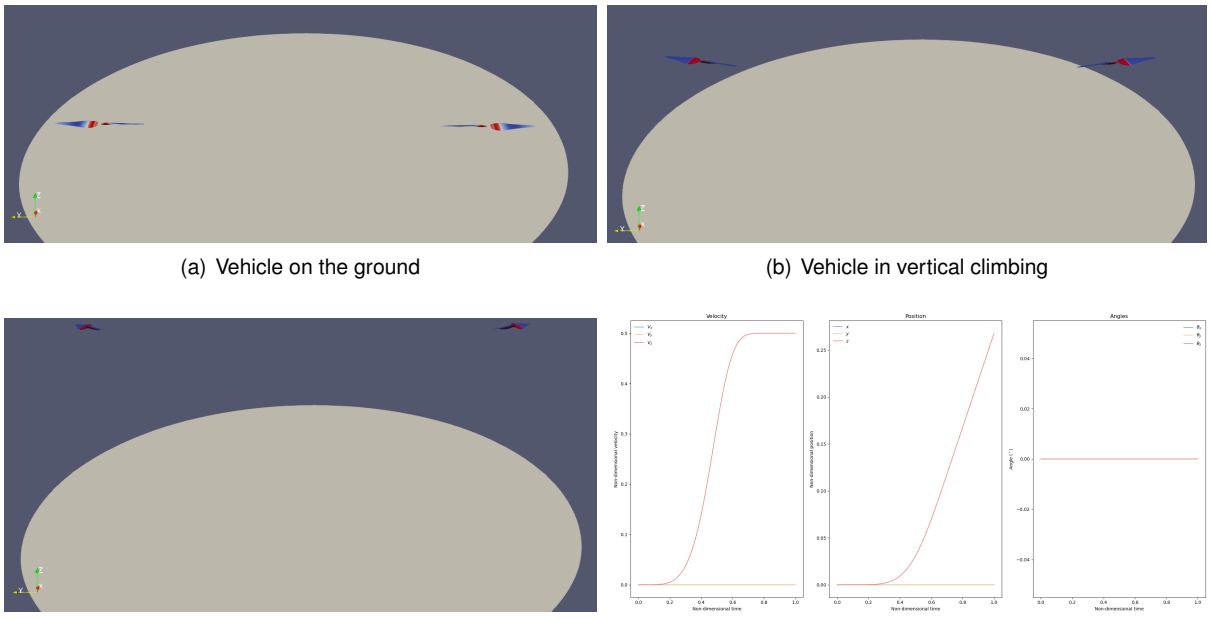

(a) Vehicle on the ground

(b) Vehicle in vertical climbing

(c) End of the simulation

(d) Velocity and position trend

Figure 3.6: Vertical climb of a double rotor model

3.4 Simulation

Once the 2D and 3D properties of the model are analysed and the maneuver is set up, it is possible to start the simulation and compute the aerodynamic loads acting along the structure and the induced velocities, as shown in figure 3.7.

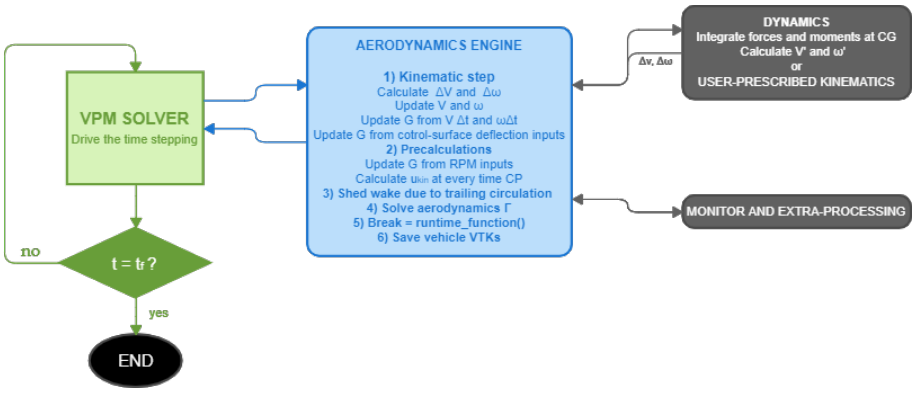

Figure 3.7: Flowchart of FLOWUnsteady framework

As it is possible to see, the first step is the green box on the left, which is the VPM solver that drives the time stepping of the simulation. VPM is a mid-fidelity approach for modeling complex wake interactions, in fact VPM is a useful approach to capture the unsteady wake behaviors occurring due to the rotor-to-wake or wake-to-wake interactional effects [68].

This method is a first-principles-based approach for modeling unsteady dynamics, mixing, and viscous decay of wakes. It discretizes the vorticity field into free particles, and solves the vorticity form of the Navier-Stokes equations in a Lagrangian scheme. In the study conduced for this project the VPM solver is not applied, only the BEM theory and VLM method are used to study the quasi-steady wakes, as already mentioned in section 3.2. In order to understand the entity of the wake-to-wake interaction analysed by VPM solver, the research conducted on quadrotor models of UAV, as shown in figure 3.8, by Hakjin Lee and Duck-Joo Lee in the article [68] and by Dhwanil Shukla and Narayanan Komerath in [69] are considered. They focused their study in the investigation of rotor-to-rotor, and so wake-to-wake, interactional effects with the mutation of the separation distance (d), as illustrated in figure 3.8, and for this reason some considerations and results will be cited hereafter:

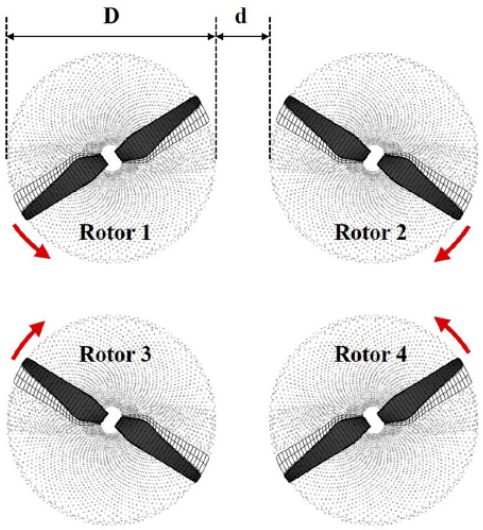

Figure 3.8: Multirotor configuration and definition of the separation distance (d), from [68]

- the average thrust coefficient of the quadcopter tends to be close to that of the isolated rotor with an increase in the separation distance between the pair of rotors, as shown in figure 3.9;

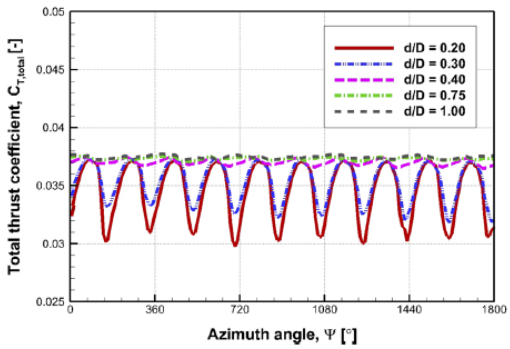

Figure 3.9: Time variation in the total thrust coefficient of the multirotor depending on the separation distances, from [68]

- when the separation distance becomes larger than $1.0D$, where D is the diameter of the rotor studied, the wake flow seems to have little influence on the wake evolution of the neighboring rotor and the recirculation wake region (upwash flow caused by the wake vortices trailed from the blade tip of adjacent rotors, that forces the wake vortices to move from the downstream to the upstream) completely disappears, as depicted by the difference between figure 3.10 with a separation distance of 0.2D and figure 3.11 with a separation distance of 1.0D;

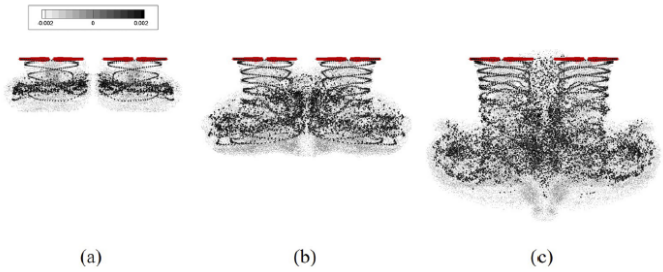

Figure 3.10: Wake evolution of the multirotor with d = 0.2D: (a) 5 rev., (b) 10 rev., and (c) 15 rev., from [68]

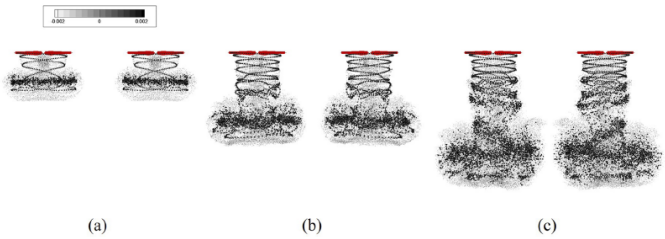

Figure 3.11: Wake evolution of the multirotor with d = 1.0D: (a) 5 rev., (b) 10 rev., and (c) 15 rev., from [68]

- the upwash flow, and so the upward velocity, becomes less pronounced with an increase in the separation distance, and the axial velocity distribution around the individual rotor of the multirotor

with the interval of 1.0D appears to be similar with that of the isolated rotor, as depicted in figure 3.12.

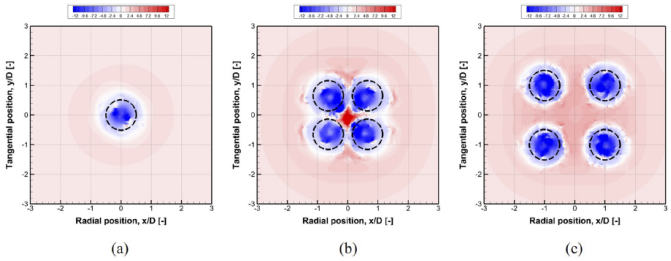

Figure 3.12: Comparison of the axial velocity contour on the horizontal plane (z = 1.0D): (a) isolated rotor, (b) multirotor with d = 0.2D, and (c) multirotor with d = 1.0D, from [68]

Through these considerations and conclusions it is possible to declare that the VPM solver, necessary to capture the unsteady wake behaviours occurring due to the rotor-to-wake or wake-to-wake interactional effects, becomes useful especially for the case of small separation distance model and at low Reynolds number; both conditions will not be part of our case of study. For this reason, the VPM solver continues to drive the time stepping of the simulation, but it is not direct implemented in the program.

In order to guarantee the correctness of the results obtain in this study case it is necessary to satisfy the condition analysed before.

3.4.1 Aerodynamics Engine

The green box, discussed in the previous section, calls another step of the flowchart in figure 3.7 represented by the light-blue box, which is called Aerodynamics engine and it is better depicted in figure 3.13.

At this step the structure is moved in the simulation space, following the kinematic or dynamic rules. Since in section 3.3.1 has been already described the Dynamic Maneuver, here will be explained the kinematic one: the geometry of the vehicle is shifted and rotated according to its translational and rotational velocity. First, velocities and vehicle angles changes, ΔV and $\Delta\omega$, are either calculated from the kinematics or prescribed by the user. The state variables V and ω are then updated, and the whole geometry is translated and rotated according to V and ω. Since this process is repeated for each time step the time is updated $t_{sim} = t_{sim} + \Delta t$.

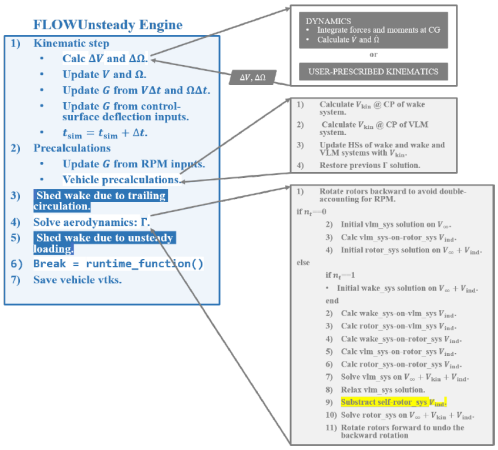

Figure 3.13: Flowchart of FLOWUnsteady framework, from [66]

In the precalculation step (2) of figure 3.13, rotors are rotated according to RPM control inputs and

the kinematic velocity V_{kin} of each control point (CP) of wake and VLM systems are calculated; then, the horseshoes are recalculated with kinematic velocity and the previous circulation (Γ) solution is pasted to new system position after translation. The step (3) "Shed wake due to trailing circulation" is not computed in this study since it is applied the Quasi-steady solver, as already mentioned. Then at the step (4) is finally applied the solver, which is itself divided into the following processes:

- the rotors are brought back to their initial positions at beginning of this time step before 'precalculations'. This is needed to avoid double accounting for the RPM when the solver is run;
- a initial solution of VLM systems is found using the free-stream velocity, V_∞, through the VLM method defined in section 2.4;
- the velocity induced, V_{ind}, by VLM systems on the rotor systems at each control point is calculated;
- the BEM theory is used to elaborate the circulation on each blade using the new $V_\infty + V_{ind}$ as velocity.

After this first step, where $n_t = 0$, it is calculated the solution of the wake system, treated as a VLM system, using $V_\infty + V_{ind}$ as velocity. Then, subsequently to these initialization of the systems used, the solver can continue with the following steps:

- the velocities induced by the wake-system on the VLM and rotor systems are elaborated;
- the velocities induced by the rotor systems on the VLM systems, and vice-versa, are calculated;
- it is elaborated the self-induced velocity by the rotor systems on themselves;
- The self-induced velocity of the rotor systems is subtracted from the total velocity, otherwise the solver will get on a positive-feedback instability;
- The VLM and rotor systems are solved, through VLM method and BEM theory, respectively, using the total velocity $V_\infty + V_{kin} + V_{ind}$;
- the rotors are rotated forward in order to undo the previous backward rotation.

All the solutions found are saved as previous solutions, since the whole light-blue box is repeated until the total time of the simulation is reached, and the vehicle is saved in vtk format to allow the user to visualize the simulation.

3.5 Aeroacoustic Solution – Tonal Noise

Once all the aerodynamic solution are obtained, it is possible to proceed through the aeroacoustic computation. The aerodynamic solution are used to feed PSU-WOPWOP, already described in section 2.5. At the hypothetical user it is requested to define the number of revolution, steps for each revolution, the position of the single microphone or of the grid of microphones with respect to the center of the hub.

In this last case it is also necessary to declare the number of microphones desired and the distance between each one in degrees. Before running the computation step, it is possible to select the output flags referring to the output files that are possible to get from PSU-WOPWOP:

- *acousticPressureFlag*: through this flag is gotten the file that contains the acoustic pressure, p', as a function of observer time, t. Two different sets of files are output depending on the number of observers. If only a single observer point was used the pressure from each component of the noise as function of time is the output. If a grid of observer locations was calculated the output is as two Plot3D whole, single-zoned, structured and binary files;
- *SPLdBFlag*: it allows to get the sound pressure level as a function of time for any number of frequency ranges; also in this case two different sets of files are output depending on the number of observers and the same considerations of the former point are valid;
- *SPLdBAFlag*: it allows to get the A-weighted sound pressure level as a function of time for any number of frequency ranges;
- *OASPLdBFlag*: sound pressure level for the entire frequency range of the FFT;
- *OASPLdBAFlag*: A-weighted sound pressure level for the entire frequency range of the FFT;
- *spectrumFlag*: PSU-WOPWOP can also directly output the results of the fast Fourier transform for either a single observer or grid of observers;
- *audioFlag*: PSU-WOPWOP can output an audio file of the calculated noise. These files are output for each component of noise calculated (thickness, loading and total), in .wav format, but they can be quite large.

3.6 Aeroacoustic Solution – Broadband Noise

As already aforementioned in the section 2.6, this model for the prediction of the self-generated noise of an airfoil blade encountering smooth flow was developed by Brooks, Pope and Marcolini in 1989. The BPM models includes five self-noise mechanisms for airfoil immersed in a flow due to the specific boundary-layer phenomena: boundary-layer turbulence passing the trailing edge (TBL-TE), separated-boundary-layer and stalled-airflow flow, vortex shedding due to laminar-boundary-layer instabilities, vortex shedding from blunt trailing edges, and the turbulent vortex flow existing near the tips of lifting blades. As happens for the Tonal Noise computation, also for this module, at the hypothetical user it is requested to define details regarding the single observer or about the grid of observers; and, as already mentioned in ”Trailing-Edge Bluntness – Vortex Shedding” paragraph 2.6.4, another important input is the trailing edge thickness defined in degrees, Ψ, to whom BPM solver is particularly sensitive. This solver can write four files: SPL (non-weighted), A-weighted SPL, OASPL and A-weighted OASPL.

Chapter 4

Experiental Setup and Results

This chapter will be dedicated to the description of laboratory activities conducted inside the Aeroacoustic Wind Tunnel located at the Aerospace Engineering Laboratory of Instituto Superior Técnico (IST) of Lisbon, shown in figure 4.1, in order to analyse experimentally the noise produced by a rotor inside the anechoic chamber. In this chapter the Equipment, the microphones calibration, the wiring layout, the data acquisition system will be described alongside the experimental results which will be compared with the numerical ones.

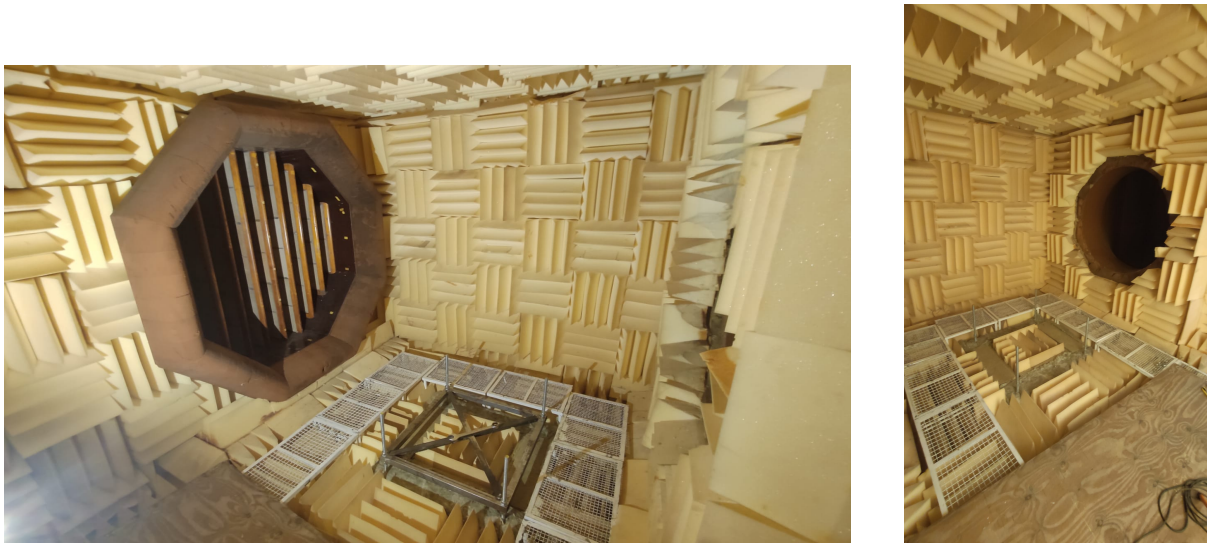

(a) Bottom side of the wind tunnel (b) Front side of the wind tunnel

Figure 4.1: Aeroacoustic Wind Tunnel located at the Aerospace Engineering Laboratory of Instituto Superior Técnico (IST)

4.1 Equipment

The workbench used in these experimental measurements is made of one Instrumented Tube (IT) connected to the electric motor at its free end, as shown in figure 4.2. For this experiment, other equipment is necessary and described here. The reference of each equipment is related to its datasheet

and/or its user manual:

- **Computer**: a desktop computer with labVIEW, described in section 4.1.1, installed and the necessary tool kits. The computer used has $8GB$ of RAM and a processor Intel core i5 with $3.5GHz$ of maximum working frequency;
- **DAQ board NI PCIe-6353**: it has 16 differential (reference and signal) or 32 single ended channels, offering analog I/O, digital I/O, four $32bit$ counters/timers for pulse-width modulation (PWM), encoder, frequency, event counting, and more. It has a sampling frequency of $2.5MHz/s$, sufficient for the acquisition of the microphone signal. This DAQ board is connected directly to the computer through a computer bus [70].
- **Connector block NI CB-68LP board**: An auxiliary connection board that allows to make the necessary physical connections to the acquisition system. This board is an unshielded I/O accessory with 68 screw terminals [71].
- **PCB Piezotronics 482C15 ICP Sensor Signal Conditioner**: it is used to power the pre-polarized microphones. Each conditioner has four channels and for this reason two devices are necessary, since 6 microphones are used in this experiment. It amplifies the signal from the senors, connecting them to the connector block [72].
- **Power Supply**: a $2000W$ power supply. It has an input of $220-240V$ DC and an output of $12-30V$ DC;
- **Cable Connector**: a 10 meters long (National Instruments) NI custom shielded cable model SHC68-C68-D4, used for high-speed digital devices. This cable connects the connector block to the PCIe-6353 DAQ board, already described;
- **BLDC motor EMP N2830/13**: The motor is used to attach and rotate the rotors. It has a maximum power of $300W$.

Moreover, together with all the equipment already described, several sensors are used:

- **RPM sensor**: the CNY70 is a reflective sensor which includes an infrared emitter and photo-transistor output, that changes with the intensity of the reflected light. The motor rotation speed is read by he photo-transistor, which is sensitive to the variation from black and white tape around the motor [73];
- **Voltage sensor**: The Pitlab voltage sensor, which also measures current, provides two analog voltage outputs: one for the current signal and the other for the voltage signal [74];
- **Current sensor**: The LTSR 25-NP model [75];
- **Temperature sensor**: LM35DZ sensor is positioned in order to monitor the temperature of the motor during the experiment. It has a supply voltage of $5V$ and a low absolute error [76];

- **Microphones**: 6 pre-polarized microphones type 4958, from Brüel & Kjær. These microphones have an excellent amplitude and phase-matching for a wide range of temperature and humidity [77].

Following the microphones are further described together with wiring layout and labVIEW. The equipment just introduced and the connections between them, that will be described further later, are shown in the scheme 4.2.

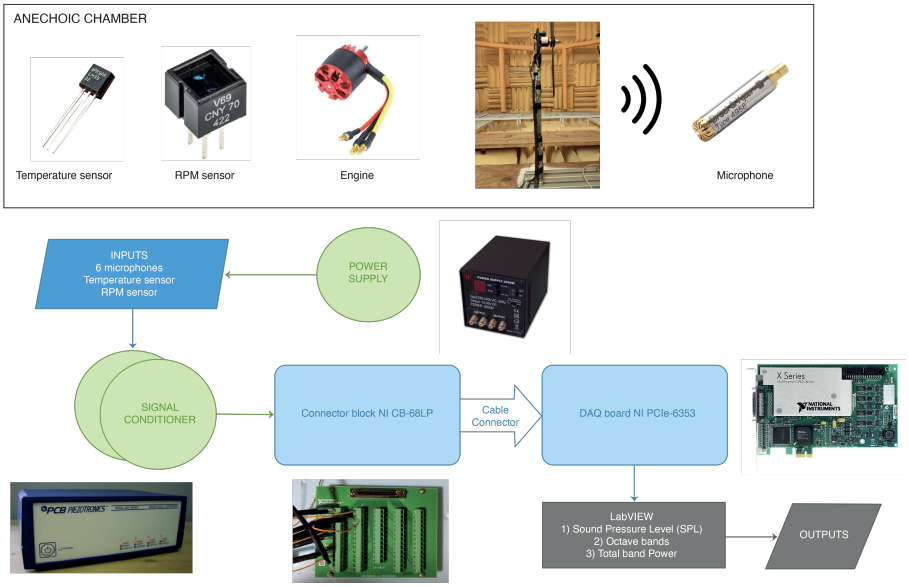

Figure 4.2: Equipment and connection of laboratory set up

4.1.1 Data Acquisition System-LabVIEW

Laboratory Virtual Instrument Engineering Workbench (labVIEW) is a systems engineering software for applications that require test, measurement, and control with rapid access to hardware and data insights. LabVIEW offers a graphical programming approach that helps to visualize every aspect of the application, including hardware configuration, measurement data and debugging. This visualization makes it simple to integrate measurement hardware from any supplier, represent complex logic on the diagram, develop data analysis algorithms, and design custom engineering user interfaces. This software is a programming environment in which programs are created using a graphical notation (functional nodes are connected via wires through which data flows). The programming language used in LabVIEW is called ”G”. It has extensive libraries of functions and subroutines to help with most programming tasks, without the typical problems in conventional programming languages. The program consists of one or more virtual instruments (VIs). The VI is composed by three main parts:

- Front panel: it is the interactive user interface of the VI and it simulates the instrument physical panel. The front panel can contain graphs, buttons, knobs, throttle and many other controls;
- Block Diagram: it consists of the source code, in fact it is the actual executable program. Block diagram objects include terminals, sub-VIs, functions, structures and wires that transfer data among

block diagram objects;

- Icon: it is the pictorial representation and it is used as an object in the block diagram of another VI.

The main characteristic of LabVIEW are summarized in table 4.1.

LabVIEW	Conventional Language
VI	program
function	funtion or metod
subVI	subroutine, subprogram, object
front panel	user interface
block diagram	program code
G	C, C++, Java, Pascal, etc.

Table 4.1: Comparison between the terms used in LabVIEW and other programming languages

4.1.2 Microphones

The Brüel & Kjær type 4958 microphone is an $1/4$" pre-polarized microphone, suitable for beamforming arrays requiring a large number of microphones. It has an excellent amplitude and phase-matching, with an operating range of temperatures from -10 to $+55$℃ and humidity range between 0% and 90% RH without condensation. Its sensitivity is $11.2\frac{mV}{Pa}$, with an upper limit of dynamic range of $140dB$ and a maximum output voltage swing of $14V_{pp}$. This kind of microphone is accompanied with BNC to SMB cables to be linked to the signal conditioners because it has a SMB coaxial plug as an output socket. It is well fit especially for free-field measurements conditions, where the sound waves are free to spread from the source without reflections or reverberations. For this reason the microphones work well in the anechoic chamber, which is projected to cancel all sound reflections and reverberations, simulating a free-field; in this way the microphones measure the sound pressure level as it existed before they were plunged into the sound field.

4.1.3 Wiring Layout

As already aforementioned, the microphones used in this experiment are 6 and each of them sends the signal to the signal conditioner, that in turn is linked to the NI CB-68LP board, which it is used for the physical connections. Each microphone is accompanied by a SMB to BNC cable to connect it to one of the four channels of the signal conditioner. The microphone signal is then amplified and transmitted to the connector block through a RG-58 coaxial cable. The signal conditioner is set to amplify the microphone signal 100x, as is recommended by the microphones manual [77], the procedure to operate with the signal conditioner is described in Appendix B. The NI CB-68LP board is finally connected to the NI PCI-6353 acquisition board through the cable connector. Figure 4.3a shows a diagram of the connector block, in which is represented the screw terminals and the 68-Pin I/O to where the cable connector is attached. Figure 4.3b shows all the wiring connections between the connector block and the other components. The signals received from the microphones are all in differential mode, so there

is the reference (in red) and the signal (in yellow) for each microphone in order to reduce the noise error that can be obtained using the same reference for all the signals received. The single output signal (in green and black) is sent to control the electric motor. The RPM sensor and the temperature sensor are powered by the power supply, as illustrated by the blue links in figure 4.3b. Table 4.2 is used to provide a more detailed description of where each wire is linked.

Input/Output Signals		
Ch0	Microphone 0	CH+ 68/yellow wire; CH- 34/orange wire
Ch1	Microphone 1	CH+ 33/yellow wire; CH- 66/orange wire
Ch2	Microphone 2	CH+ 65/yellow wire; CH- 31/orange wire
Ch3	Microphone 3	CH+ 30/yellow wire; CH- 63/orange wire
Ch4	Microphone 4	CH+ 28/yellow wire; CH- 61/orange wire
Ch5	Microphone 5	CH+ 60/yellow wire; CH- 26/orange wire
Ch6	RPM RS	CH+ 25/yellow wire; CH- 58/orange wire; +5V 14/blue wire
Ch7	Temperature TS	CH+ 57/yellow wire; CH- 23/orange wire; +5V 8/blue wire
ESC	PWM Output	a1 21/green wire; 54GND/black wire

Table 4.2: Connections between sensors and the PCIe-6353/CB-68LP terminals

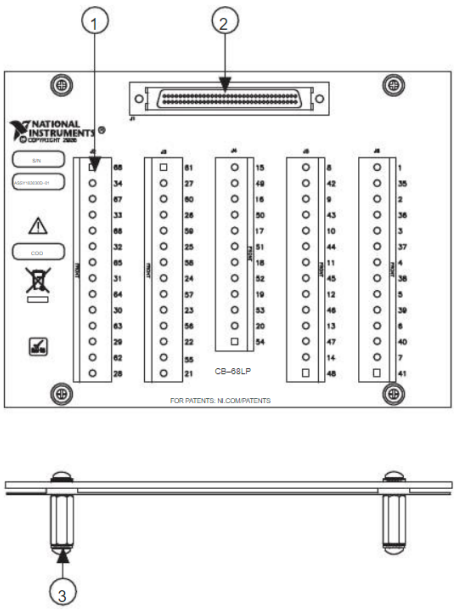

(a) NI CB-68LP parts locator diagram. **1)** Screw terminals; **2)** 68-Pin I/O Connector; **3)** Metal Standoff Foot

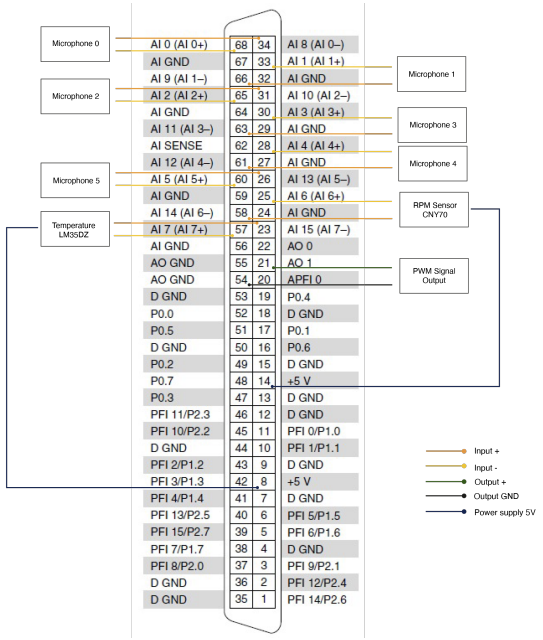

(b) Wiring connections to the PCIe-6353/CB-68LP terminals. **AI** Analog Inputs; **AO** Analog Outputs; **+5V terminal** supply voltage to the sensors. **PFI lines** Programmable Function Interface (Digital)

Figure 4.3: Schematic of the CB-68LP connector block and the NI PCIe-6353 pinout

Table 4.3 is used to describe the connections between the microphones, the signal conditioners and the NI CB-68LP board.

Input/Output Signals		
Microphone	Signal Conditioner [Channel, Conditioner]	Pinout connections
Mic0	Channel 2,1	(+) 68 [AI 0 (AI 0+)] (-) 34 [AI 8 (AI 0-)]
Mic1	Channel 3,1	(+) 33 [AI 1 (AI 1+)] (-) 66 [AI 9 (AI 1-)]
Mic2	Channel 4,1	(+) 65 [AI 2 (AI 2+)] (-) 31 [AI 10 (AI 2-)]
Mic3	Channel 2,2	(+) 30 [AI 3 (AI 3+)] (-) 63 [AI 11 (AI 3-)]
Mic4	Channel 3,2	(+) 28 [AI 4 (AI 4+)] (-) 61 [AI 12 (AI 4-)]
Mic5	Channel 4,2	(+) 60 [AI 5 (AI 5+)] (-) 26 [AI 13 (AI 5-)]

Table 4.3: Connections between the microphones, the signal conditioner and the connector block

4.1.4 Noise Measurement system

The microphones read the sound waves, turning them into an electric signal. This latter is amplified by the signal conditioner and reaches the computer through the DAQ device.

The LabVIEW software reads, records and processes the microphones signal. The LabVIEW program used to evaluate the noise in this thesis was adapted from the one created by Pereira [78]. This program was firstly created to evaluate the sound produced inside the wind tunnel. However, the program cannot only read the signals coming from the microphones, but it also needs to interact with the workbench, in particular with the motor and with the RPM sensor. So, the initial program was adapted and a throttle control was added to the motor to vary the rotation speed. Moreover, it was introduced a system to clear the previous data collected and restart all acoustic operations to allow changing the rotation speed between tests. The acoustic operations performed to the data collected from each microphone are the following:

- Fast Fourier Transform for converting the results from the time domain to a frequency domain, providing the variation of SPL with frequency;
- One-third Octave bands grouping of the SPL;
- Calculation of the L_{eq};
- Calculation of the total band power.

The voltage signal of the microphones varies in frequency and amplitude over time. This latter needs to be converted to pressure units, Pascal. As declared by the Nyquist's sampling theorem [79], the sampling rate has to be higher than, at least, two times the maximum frequency intended to record. Referring to the interval of frequencies captured by human hearing, from $20Hz$ to $20000Hz$, the sampling rate must be higher than $40000Hz$. Anyway, the recommended value is five times the maximum frequency, so the

sampling is set to $100000Hz$. So, the number of sample is set to 50000, with a collection time of $30s$ per test. The Fast Fourier Transform is applied using a Hanning window, with a number of averages of 1000, RMS averaging mode and linear weighting. This latter converts the data to SPL, over frequency, enabling to study and compare the noise produced by the rotor in the frequency spectrum. The one-third octave bands group the SPL in bands of frequency similar to how the human hearing distinguishes frequencies. Moreover, an important option available in LabVIEW program used is the application of a weighting filter, as A-weighting, B-weighting, C-weighting or no weighting filter. In this experiment the A-weighting filter is applied, which highlights the frequencies to which the human hearing is more sensitive to.

4.2 Calibration

Before starting with the experiment, the sensors (the microphones in this particular case) need to be calibrated in order to guarantee that the results obtained are trustworthy. For this reason the present section is used to explain the microphone calibration procedure.

4.2.1 Microphone Correction

As aforementioned, in order to get trustworthy results from the microphones, each one must be calibrated; this procedure is done using a calibrator of sound level-type 4231. This latter is a pocked-sized source of noise for the calibration of sound level meters and other instruments for the measurements of noise. This calibrator is compatible with Brüel & Kjær microphones of different size thanks to the removable adaptors used. The calibrator gives a continuous sound pressure level when fitted on a microphone and activated. This calibration pressure is equal to $94 \pm 0.2dB$, in case of calibration in noisy environments, or for checking linearity, it is used $114dB$ SPL. The calibration frequency is $1000Hz$, which is the standardized international weighted networks. The noise signal received from the microphone is shown thanks to the LAbVIEW interface, as illustrated in figure 4.4; its sensitivity can then be adjusted until it indicates the correct sound pressure level. This process is repeated for all the 6 microphones used and the calibration is not affected by changes in temperature and static pressure, or at least these can be negligible due to being very low. Following, in figure 4.5, is shown the calibrator of sound level-type 4231 used.

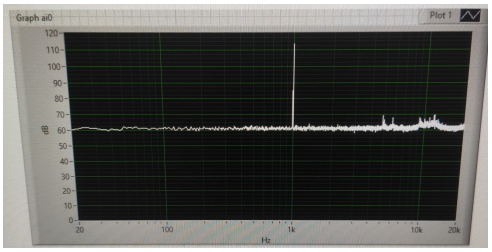

Figure 4.4: Signal detected by the microphone during the calibration

After the microphones corrections, the pregain values used are the ones presented in Table 4.4.

Once the calibration is concluded, the microphones are set in the anechoic chamber at a radial distance of $2.3m$ from the location of the rotor model, as illustrated in figure 4.6. This set-up is the one

(a) Sound Calibrator-Type 4231

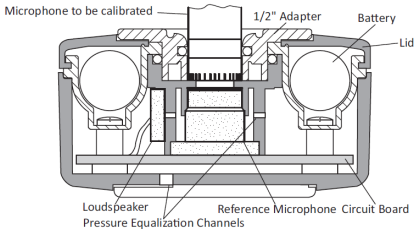

(b) Cross-sectional view of Sound Calibrator Type 4231. The feedback loop is based on a high-quality condenser microphone to ensure a very stable sound pressure level

Figure 4.5: Representation of the Sound Calibrator-Type 4231 used in the experiment, from [80]

Microphone	Final Pregain
Mic 0	-0.72 dB
Mic 1	-0.72 dB
Mic 2	+0.10 dB
Mic 3	-0.80 dB
Mic 4	-0.05 dB
Mic 5	+1.13 dB

Table 4.4: Microphones pregain values

used by Pedro Miguel de Barros e Silva Duarte, as it will be explained later, who implemented just 3 microphones for the noise measurements.

(a)

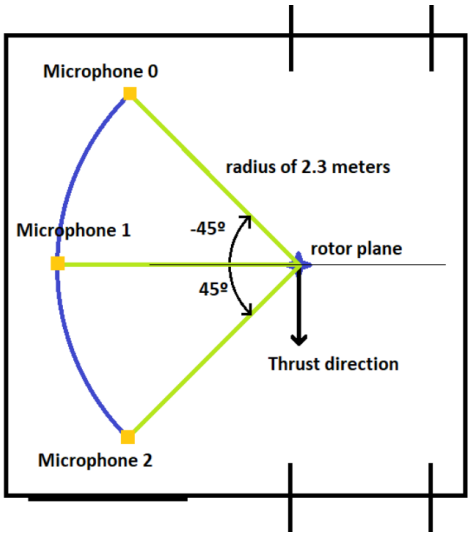

(b)

Figure 4.6: The microphones positions in the anechoic chamber, from [81]

4.3 The Anechoic Chamber Characterization

As already mentioned in section 4.1.2 the measurements are taken inside an anechoic chamber, which is an echoless room and for this reason its walls, floor and ceiling do not reflect any sound. In fact, this particular room is able to absorb 99% of sound or more through its walls, and, moreover, it is able to isolate the sound sources inside the room and eliminate totally any external sound.
For this experiment is used the anechoic chamber located at the Aerospace Engineering Laboratory of IST, which has a usable volume approximately of $4.3 \times 3.2 \times 2.7$ meters ($Length \times Width \times Height$) and it has a grid floor installed that allows to walk within. The chamber is covered by acoustic foam straight wedges, with a tip-to-base dimension of $0.285m$, which provides a cut-off frequency of $200Hz$; this means that, for higher frequencies, this room has a sound energy absorption of 99%, or that the reflected SPL is lower than 10%. It was used a single wooden board, covering part of the floor, in order to place the workbench and the rest of the equipment used. This wooden board was positioned the farthest away from the microphones in order to minimize its influence. Moreover, for reducing reflections from this board, the workbench was placed at the edge closer to the microphones. The other equipment, that produced noise, was covered with foam wedges and placed away from the microphones.

Unfortunately, given the short time frame for this thesis and the pandemic context, in this study are used the values collected by Pedro Miguel de Barros e Silva Duarte, who followed the same procedure aforementioned but applying just 3 microphones at $45°$, $0°$ and $-45°$ with respect to the rotation plane of the rotor, as already shown in figure 4.6. For this reason, all the measurements represented in this chapter are the results of his work conduced in 2020 and described in his master thesis [81].

Figure 4.7 presents the background noise measured by each microphone. From this graph it is possible to observe clearly that the cut-off frequency corresponds to the estimated one of $200Hz$. In fact, for lower frequencies the existence of sound reflection is perceptible. Furthermore, the background noise at frequencies above the cut-off one is rather low as expected. This condition is acceptable for the measurements conducted in this experiment.

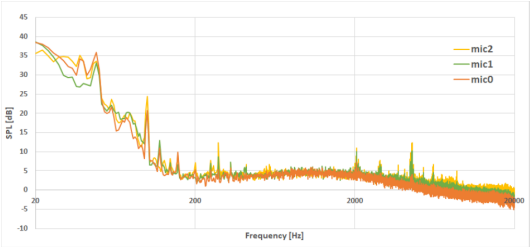

Figure 4.7: The background noise present at the anechoic chamber, from [81]

4.4 Numerical Results & Comparison

Before comparing the results with experimental ones obtained from the measurements at the laboratory of Instituto Superio Técnico, it was necessary to proceed with the modification and validation

of the FLOWUnsteady code. This validation is presented in this section, together with the comparison between results and the parametric study.

4.4.1 Code Validation

The code validation is done by compering the experimental measurements of the DJI9443 rotor model in hover reported by Zawodny [82] with the numerical results obtained from the FLOWUnsteady code. The rotor is tested at different RPM: 4800, 5400 and 6000. These conduce to different values of blade-passing frequency (BPF), $BPF = \frac{RPM*n}{60}$, where n is equal to the number of blades of the rotor analysed. This latter is equal to 2 in this particular model, which is shown in figure 4.8. The table 4.5 reported the RPM values and the respective BPF tested by Zawodny and used for the validation.

Figure 4.8: DJI 9443 propeller model

RPM	BPF
4800	160 Hz
5400	180 Hz
6000	200 Hz

Table 4.5: RPM and BPF values tested

The measurements are taken over a circular array of microphones located at distance of $7.9D$, where D is the diameter of the rotor, from the rotor hub. For validation purposes, the values recorded by the microphone at $-45°$ below the plane of rotation are taken under consideration, shown in figure 4.9, and compared to the tonal and broadband noise calculated through the FLOWUnsteady code. All the simulations successfully predict the sound pressure level produced at the different RPM values, unfortunately the prediction is underestimated at frequencies higher than 50 times the first BPF.
Furthermore, it was analyzed the agreement at the first BPF of the sound pressure level and the OASPL, for the case of 5400 RPM, between the experimental and predicted values, as shown in figure 4.10.
In these two plots it is possible to see that the experimental values are well predicted, there is just an underestimation of the OASPL values at the correspondence of the microphone aligned with the plane of rotation; this could be associated with an underestimation of the thickness noise and, as already explained in section 2.5.2, the HSI noise sources, which propagates in the rotation plane, are neglected since belonging to the quadrupole term

In the same way, the A-weighted results recorded by the same microphone at $-45°$, below the plane of rotation, were compared with the numerical values, as shown in figure 4.11, in order to analyse their trustworthiness.

From what was just analysed, it is possible to say that the prediction done by the FLOWUnsteady code, in the different cases considered, is adequate. A new comparison with the experimental data

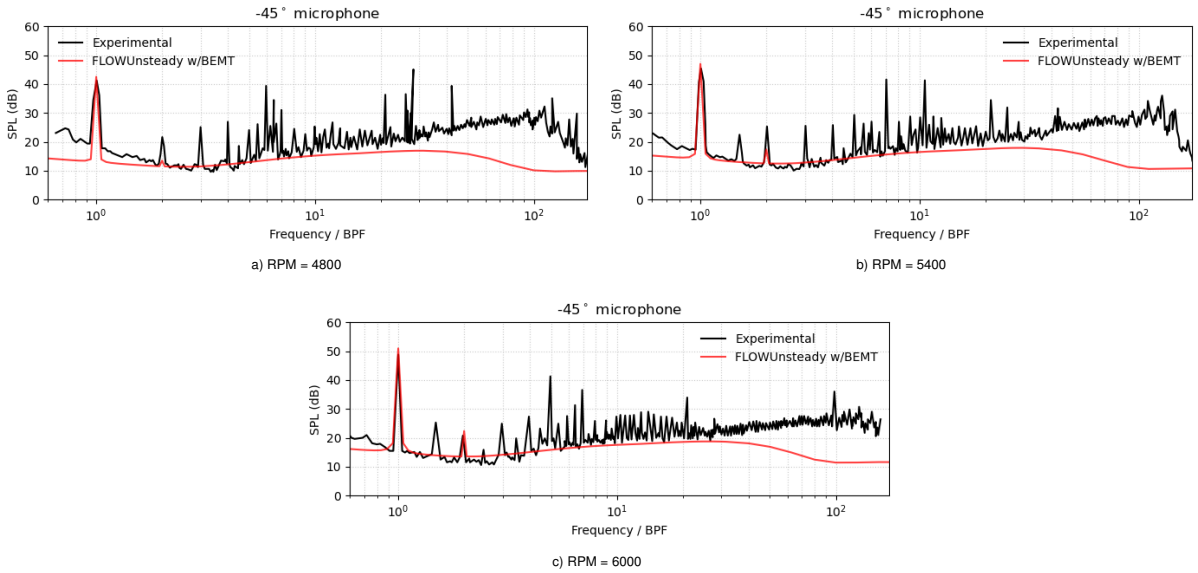

Figure 4.9: Experimental acoustic spectrum of the DJI 9443 single-rotor (measured at $-45°$ microphone) at 4800, 5400 and 6000 RPM compared to tonal predictions

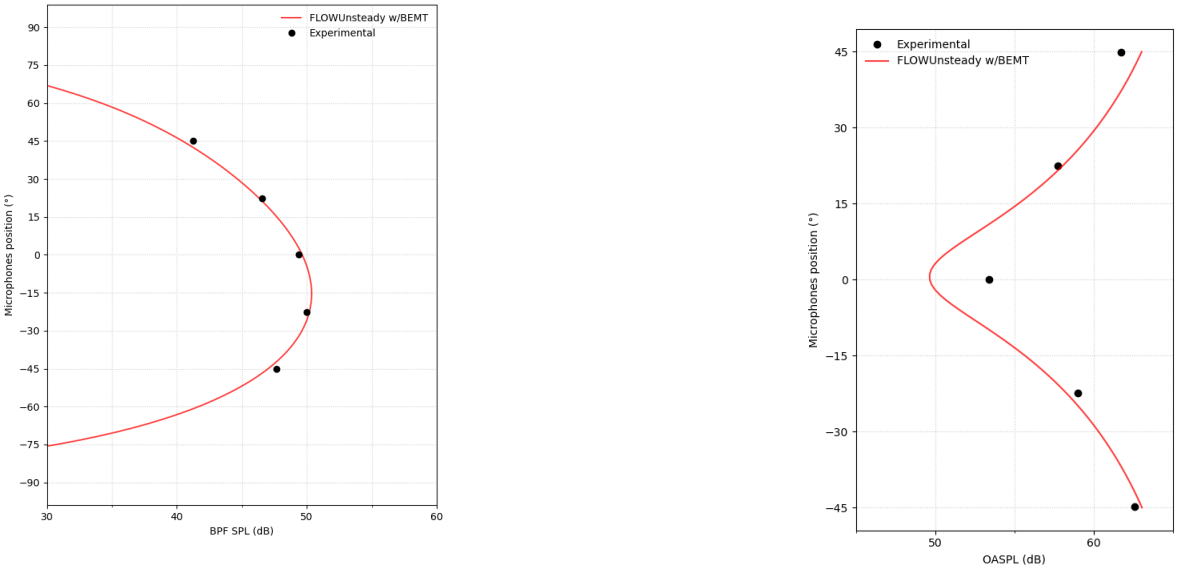

(a) Tonal directivity predictions at 5400 RPM compared to experimental measurements

(b) Overall sound pressure level at 5400 RPM compared to experimental measurements

Figure 4.10: Validation of FLOWUnsteady code for the DJI 9443 single-rotor case

collected by Pedro Duarte [81] is shown next.

4.4.2 Experimental Results and Comparison

The noise was collected from the microphones used in the experiments, which are located all around the rotor model in the anechoic chamber, as already shown in figure 4.6. The rotor tested in the experiment is called as ”baseline” and shown in figure 4.12. In order to prevent any vibration of the rotor support and workbench the interval of rotation speeds tested was set to $1000 - 4000$ RPM, with variation steps of 500 RPM. Along this section only few of the plots obtained by the several comparisons done be-

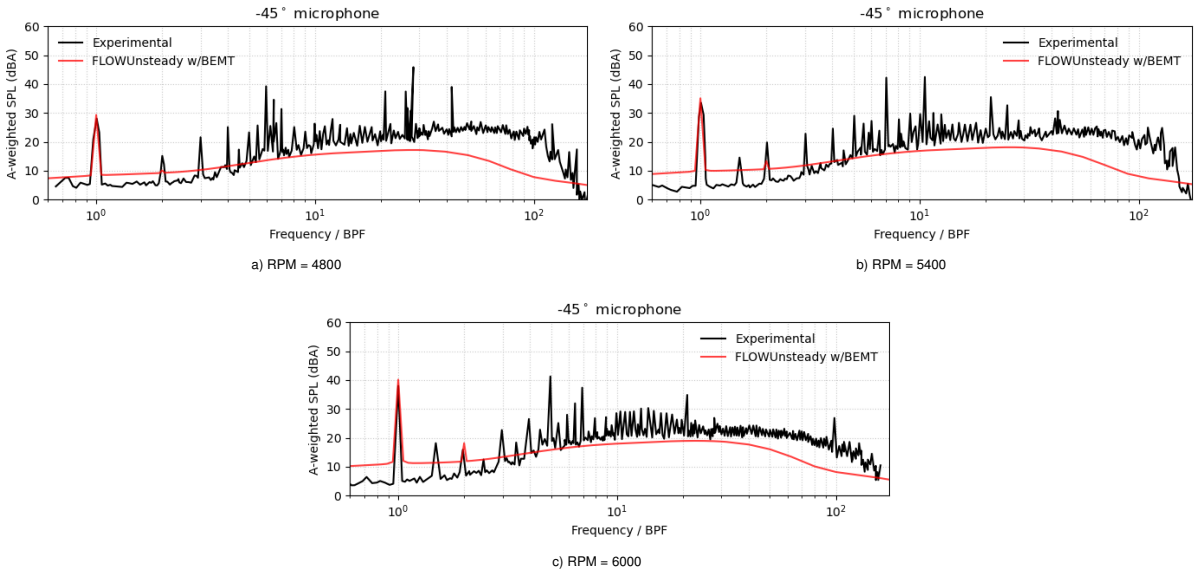

Figure 4.11: Experimental A-weighted acoustic spectrum of the DJI 9443 single-rotor (measured at $-45°$ microphone) at 4800, 5400 and 6000 RPM compared to tonal predictions

tween the experimental and the computational values are presented. The chosen graphs help to explain the observed noise and the agreement between experimental and numerical results.

Firstly are presented the plots relative to noise values captured by the microphone below the rotation plane of the rotor at $-45°$, showing the noise produced by the whole structure (Rotor, motor and the effect of the background), by the motor alone and by the background alone, in the range from 1000 to 4000 RPM. The other plots relative to the noise level measured by the microphones located at $0°$ and $45°$ are illustrated in Appendix D and in Appendix E respectively. Analysing these graphs of figure C.1, it is easily possible to state that the motor and background have a substantial impact on the noise level received by the microphones, located at 2.3 meters from the hub of the rotor, for all the cases analysed below 2500 RPM. In order to understand the noise contribution given by the single rotor was made the difference between the noise values referring to the whole structure and motor ones, as shown in figure C.2. Also in this case, in this section are illustrated the results for the microphone located at $-45°$, the others are shown in Appendix D.1 and in Appendix E.1, for them the same considerations can be listed. These graphs, especially for low RPM values (1000, 1500, 2000), show a weird trend on the far left, this is due to the low value of the first BPF that leads to a high zoom in that area; for this reason, the graphs appear like in missing of resolution, but the step frequency of analysis is always the same. In table 4.6 are shown the RPM values considered and the corresponding BPF values, in order to understand what was just explained.

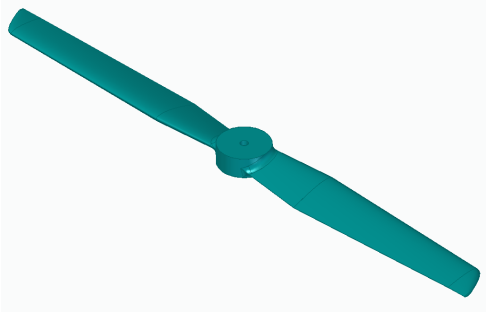

Figure 4.12: Rotor model tested experimentally

The graphs shown in figure C.2 highlight some possible resonance effects that happen between the

RPM	BPF
1000	33.3 Hz
1500	50 Hz
2000	66.6 Hz
2500	83.3 Hz
3000	100 Hz
3500	116.6 Hz
4000	133.3 Hz

Table 4.6: RPM and BPF values tested

sound waves produced by the motor and rotor, in fact for some frequencies the motor SPL value measured is higher than the whole structure, so through the difference the resultant rotor SPL value is lower than zero. The number of frequencies for which this effect happens decrease by increasing the RPM. For this reason, for the purpose of comparison of this thesis are taken under consideration only the results obtained from the tests conduced at RPM values higher than 2500, where the percentage of negative rotor SPL cases is lower than 11% referring to the sampling frequency range of $20 - 20000$ Hz with a step of 2 Hz, so 9991 frequencies analysed in total. Finally, in figure C.3 are shown the comparison conducted between the SPL spectrum predicted through the FLOWUnsteady code and the experimental ones for RPM higher than 2500, as already justified, where the cases with a negative rotor SPL values are neglected. As it is possible to observe in figure C.3 the first BPF is well predicted and in general the trend of the SPL spectrum is followed at every frequency of the range considered. In each graph, for every rotation speed, a considerable peak always appears, between 7560 and 7570Hz , but it is not produced by the blades themselves; in fact, observing the orange lines in the figures presented in C.1, it is reasonable to think that this noise peak is mainly generated by the motor when it is being powered to rotate and it was not possible to delete it completely, even through the difference conducted between the noise level associated to the whole structure and the motor one. In Appendix D.2 and in Appendix E.2 are listed the other comparison plots for the microphones located at $0°$ and $45°$ with respect to the rotation plane. As already mentioned, commenting the figure 4.10b, reference to the microphone located at $0°$ (Appendix D.2) it is possible to observe an underestimation of the noise predicted with respect to the experimental one, this could be associated to a lower prediction of the thickness and High-speed Impulsive noise sources. Meanwhile, for the other angles it is reasonable to say that the FLOWUnsteady code is able to predict with a good agreement both the deterministic and non-deterministic sources of noise.

4.5 Parametric study

So far it was possible to verify the suitability of the predictions conducted using FLOWUnsteady code for the analysed rotors. At this point, it is important to control the sensitivity and the main characters in the production of noise. For this reason, in this section, it is conducted a parametric study in order to evaluate the acoustic effects of varying the design and operating conditions of UAV rotors in hover. For

this study the same model of blade already used in the validation process, DJI9443, and shown in figure 4.8 was taken under consideration.

In order to conducted this parametric study was necessary to modify some of the main parameters that describe the rotor itself; after that, the whole simulation was run for all the cases analysed with 360 microphones located at $1.905m$ from the rotor hub, and compared with the baseline for seeing how the variation influenced the noise emission. The analysis performed and the results obtained for each one of them are described next.

4.5.1 Chord Distribution Variation

The chord distribution of the original DJI9443 model was varied linearly along the span, firstly with a reduction, more precisely halving it, then applying an increment, doubling it; all these changes were applied keeping the other design parameters constant and at the same rotation speed of 5400 RPM. The effects of these changes are shown in figure 4.13a. This figure illustrates the difference of the noise emission between the different configuration taken under consideration in reference to the first BPF, that is equal since it depends only on the number of blades (n) and on the rotational speed (RPM). It is evident that there is a significant difference when compared to the noise associated to original shape of the blade which is represented by the black line; this latter shows the values predicted by FLOWUnsteady code and, as already observed in the validation process, they approach well the experimental values that are pictured by the black dots. In fact, it is possible to see that the double size of the chord (blue line) leads to a substantial increment of the noise produced in correspondence of the microphone located at the same level of the rotation plane of the rotor, almost $7dB$ higher, which have a thickness noise origin associated to a higher displacement of fluid due to the blade motion, meanwhile the deviation is lower increasing the angular distance below this plane. This latter observation is also justified by the plots shown in figures 4.14a-b, that represent the contribution of the thickness and loading noise at the first BPF. As it is possible to observe the main increment is given by the thickness noise sources, which radiates symmetrically above and below the rotor plane, meanwhile the loading noise sources act mainly in oblique direction, specially below the plane. Even though the sources of loading noise are dipoles, this asymmetry is caused by the constructive interference between loading perpendicular to the rotor plane (which radiates equally above and below the rotor plane, but with opposite phase) and the loading in the plane of the rotor (which, driven by the motion of the source, radiates with equal amplitude and the same phase above and below the rotor plane). At the same time the reduction of the chord size along the span of the blades of the rotor leads to a lower noise emission; the deviation is almost constant for the most of the microphones taken under consideration, about $7dB$. Also in this case, the main reduction is associated to the thickness noise sources.

In order to consider the influence of these changes along all the frequency spectrum considered, the OASPL values has been analysed for the microphones localized in the range $[-45°, 45°]$, shown in figure 4.13b. As already observed, it is evident that the highest deviation for the blue line is localized at the microphone correspondent to the rotation plane. This respects the behaviour met for the first BPF

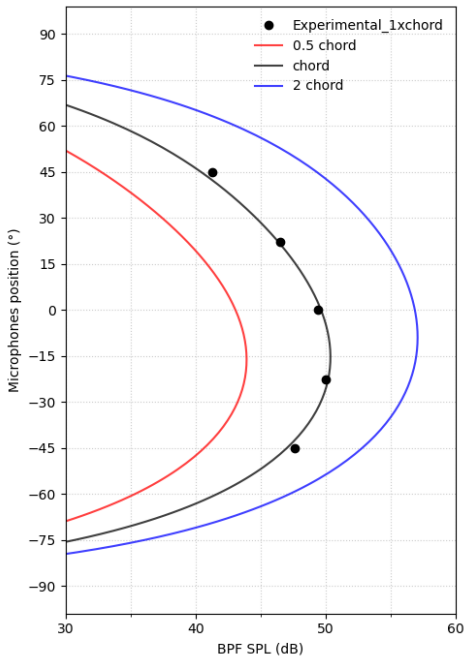

(a) First BPF directivity comparing the effects of varying the chord distribution

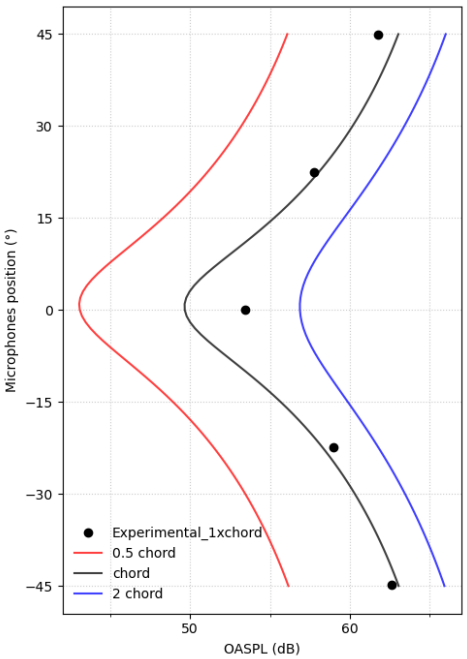

(b) Overall sound pressure level directivity comparing the effects of varying the chord distribution

Figure 4.13: Effect of the chord distribution variation on the noise emission

and justified by the graphs in figures 4.14c-d, which show the thickness and loading contribution on the OASPL directivity. The same behaviour is respect also by the red line, which shows a constant deviation from the prediction obtained for the original parameters (black line) that predicts well the experimental values, except for the microphone localized at $0°$ where the noise emission is underestimated.

4.5.2 Twist Distribution Variation

The twist distribution of the original DJI9443 model was varied linearly along the span, firstly with a reduction, three quarter of the original one, then applying an increment, doubling it; all these changes were applied keeping the other design parameters constant and at the same rotation speed of 5400 RPM. The effects of these changes are shown in figure 4.15a. This figure illustrates the difference of the noise emission between the different configurations taken under consideration with respect to the first BPF. Also in this case of study an increment of the twist parameters, blue line, defines an increment of the noise emission of about $7dB$ with respect to the black line, which shows the FLOWUnsteady prediction for the original configuration of the blade. Meanwhile, the reduction to three quarter of the original twist distribution along the span defines a $2dB$ abatement of the noise emission. The origin of these deviations is verifiable in loading noise sources; in fact the figures 4.16a-b show the contribution of thickness and loading noise respectively, in reference to the first BPF analysed. It is evident that the thickness influence is neglectable, in reverse the loading noise plays a main role.

The same behaviour is observed from the OASPL graph, pictured in figure 4.15b. Also in this case, the main contribution at the deviation from the baseline values is given by the loading noise sources, as evident in the graphs of figure 4.16c-d. The thickness noise deviations is almost null changing the twist

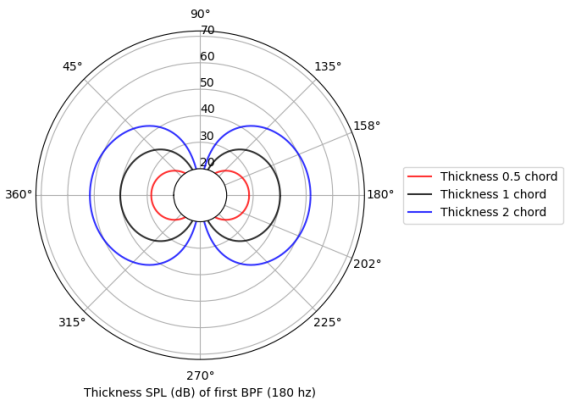

(a) First BPF directivity comparing the contributions of thickness noise as the chord distribution is varied

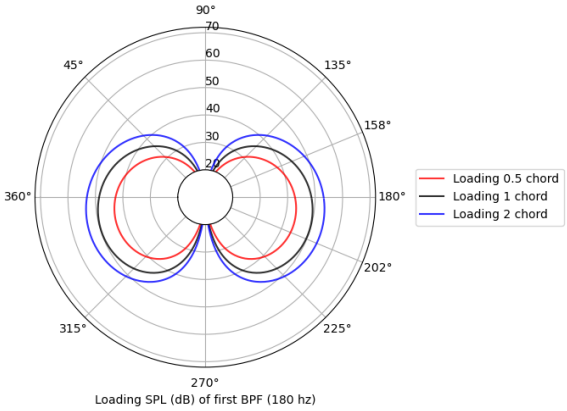

(b) First BPF directivity comparing the contributions of loading noise as the chord distribution is varied

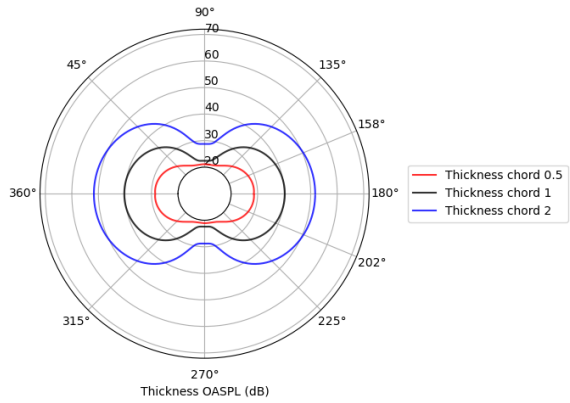

(c) OASPL directivity plots comparing the contributions of thickness noise as the chord distribution is varied

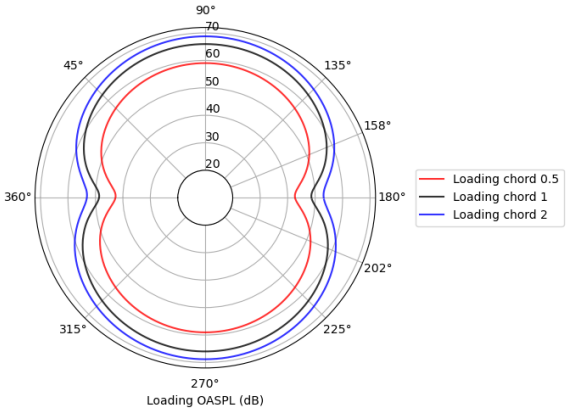

(d) OASPL directivity plots comparing the contributions of loading noise as the chord distribution is varied

Figure 4.14: Thickness and loading noise directivity varying the chord distribution

distribution of the blades.

4.5.3 RPM Sweep

A rotational rate sweep was performed on the baseline rotor design in order to observe its influence on noise emission. The rotor thrust was held constant by adjusting the collective pitch angle to compensate for the changes in RPM. The effects of these changes are shown in figure 4.17. In this particular parametric study, three different values of RPM are taken under consideration: 4000, 4800 and 5400. The blade model is always the same, DJI9443. As it is possible to observe the main contribution to the

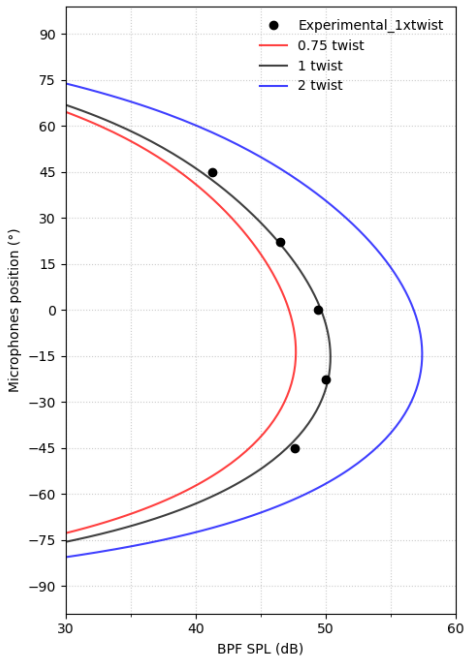

(a) First BPF directivity comparing the effects of varying the twist distribution

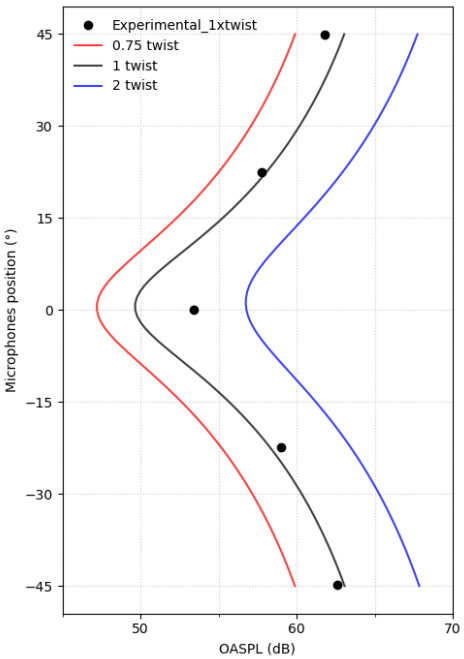

(b) Overall sound pressure level directivity comparing the effects of varying the twist distribution

Figure 4.15: Effect of the twist distribution variation on the noise emission

variation in the noise emission is given by the loading sources, whereas the thickness contribution is almost the same when varying the RPM values, except for the 4800 RPM case where thickness noise level is lower than the 4000 RPM. This behaviour was unexpected, but the reduction of the tip speed requires a higher torque to be applied to the rotor system for the same thrust, and increases the relative contribution of the in-plane rotor loads to the near-in-plane noise radiation. Anyway, the tip speed reduction is advantageous in all directions and operating points, as testified by the plot of the total OASPL noise, which shows a general increasing of noise emission at higher RPM values.

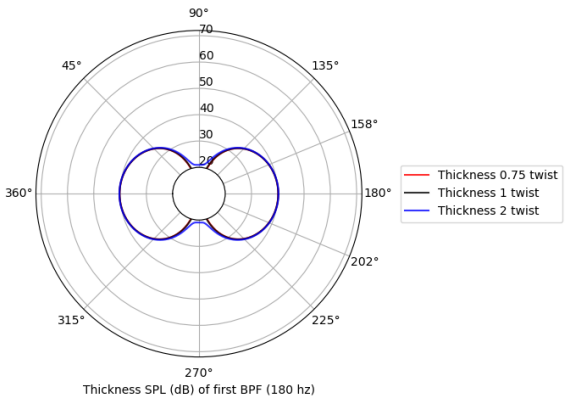

(a) First BPF directivity comparing the contributions of thickness noise as the twist distribution is varied

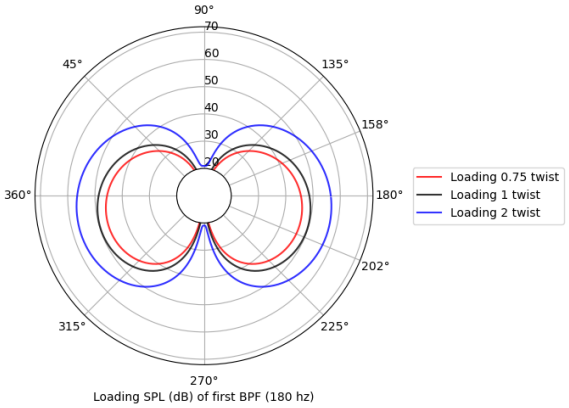

(b) First BPF directivity comparing the contributions of loading noise as the twist distribution is varied

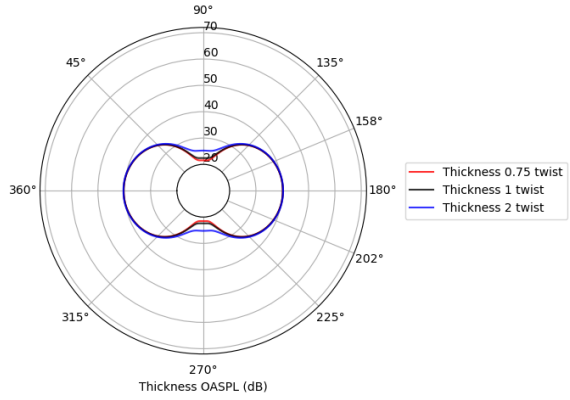

(c) OASPL directivity plots comparing the contributions of thickness noise as the twist distribution is varied

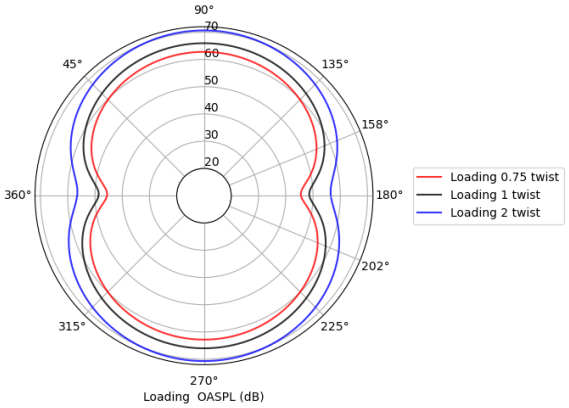

(d) OASPL directivity plots comparing the contributions of loading noise as the twist distribution is varied

Figure 4.16: Effect of the twist distribution variation on the noise emission

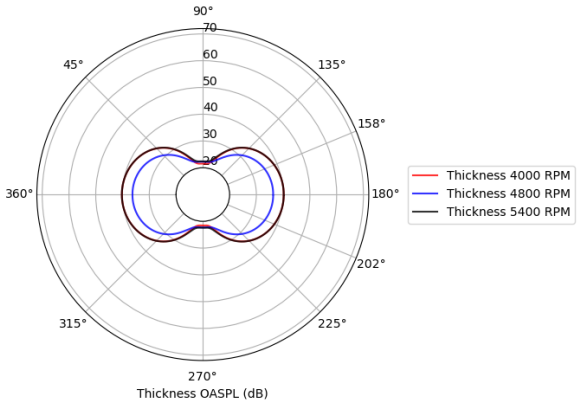

a) OASPL directivity plots comparing the contributions of thickness noise as the RPM is varied

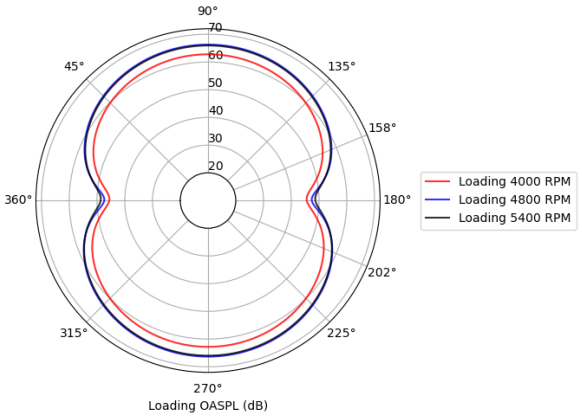

b) OASPL directivity plots comparing the contributions of loading noise as the RPM is varied

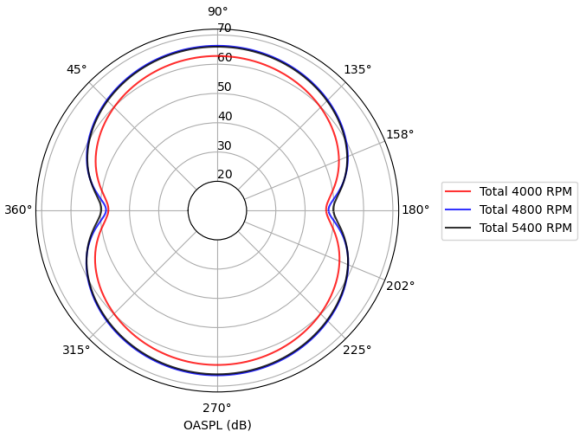

c) Total OASPL directivity plots comparing the influence of RPM variation

Figure 4.17: Effect of the RPM variation on the noise emission, considering 4000, 4800 ad 5400 RPM cases

Chapter 5

Optimization Framework

This chapter of the thesis is dedicated to a brief explanation of two of the main optimization algorithms used in different applications field of science and technology; subsequently it is introduced a description of the specific algorithm used in this work, most suitable for the task at hand, and the results obtained with respect to the starting configuration. Generally, a global numerical optimization problem aims to optimize an objective function, which depends on a set of design variables and restrictions (constrains). The problem, then, develops in the direction of optimizing the value of the objective function, either by minimizing or maximizing its value, by adjusting the values that the variables take while satisfying the restrictions. Mathematically, the optimization problem can be expressed in the following form:

$$\begin{aligned} &minimize && f(x) \\ &by\ varying && x \in \mathbb{R}^n \\ &subject\ to && g_j(x) \leq 0, \qquad j = 1, 2, ..., M \\ & && h_k(x) = 0, \qquad k = 1, 2, ..., L \\ & && x_i^L \leq x_i \leq x_i^U, \qquad i = 1, 2, ..., N \end{aligned} \tag{5.1}$$

where the objective function is $f(x)$, x is a vector containing the design variables $x_i, ..., x_N$ (N variables), and $g_j(x)$ and $h_k(x)$ are inequality (M inequality constrains) and equality constrains (L equality constrains) respectively. Each variable is bounded by its lower, x_i^L, and upper, x_i^U, limits referred to as side constrains. The design space region in where the variables satisfy all equality, inequality and side constrains is called feasible search region.

5.1 Numerical optimization methods

With the development of science and technology, there are more and more global optimization problems arising in almost every application field. Since numerical optimization problems are extremely versatile, these can be used for several scientific applications in a specific way, resulting in one op-

timization procedure for each problem. Optimization methods can be divided into two main different approaches: deterministic and heuristic [83]. Deterministic methods take advantage from the analytical properties of the problem to generate a sequence of points that converge to a local optimal solution [84]. Examples of deterministic methods are Linear, Nonlinear or Sequential Quadratic Programming [83]. On the other side, heuristic methods use concepts found in nature to discover the global optimal solution [84]. This last category includes Genetic Algorithms (GA), Ant Colonies, Differential Evolution (DE), Particle Swarm, etc. Heuristic methods are more flexible than the other category in general. However, heuristic category requests an high computational cost and the probability of finding the global optimum decreases with the increasing of the problem size. Usually, these two methods are used together: the deterministic method for refining the solution obtained by the heuristic one [85]. A brief analysis of the most popular heuristic optimization method, for efficiency and robustness, is listed following.

5.1.1 Genetic Algorithms

Genetic algorithms are heuristic search methods based on the mechanisms of natural selection and biological evolution. This algorithm was developed by Caroll [86]. GA algorithm is able to explore wide, non-linear and discontinuous domains and to be less sensitive to the initial condition when compared to the GB algorithms. The several evolutionary mechanisms included in this genetic method are briefly summarized following:

- *Selection*: In this step a tournament selection scheme is used and random pairs are selected from the population and the most fit of each pair is allowed to mate. The offspring of these mates have some mix of the two parents chromosomes according the method of crossover. The process keeps going until a new generation of n individuals is generated;
- *Crossover*: Randomly part of the genes of the two parents, string of the generation $G(t)$, are exchanged to generate two child solution strings of generation $G(t+1)$;
- *Mutation*: genes of the solution string are selected randomly and, then, changed in the range of permissible values in order to increase the variability;
- *Immigration*: The fitter individuals of the new generation replace some less fit members of the current genetic pool.

When an approximate solution respect the stopping criterion or when the maximum number of generations is met the optimization procedure is terminated. Hence, GA algorithms are reliable for global optimizations and multi-objective problems.

5.2 Optimization strategy and procedure

The strategy used in this thesis for optimizing the blade geometry consists in using a global optimization package for Julia, called Blackboxoptim, which supports a new branch of genetic algorithm,

called Differential Evolution (DE) algorithm, which shares a similar structure with GA. In particular way, in the mutation step, it generates the mutation vectors to explore the search space which mainly affects the evolutionary direction [87]. There are different DE mutation strategies that can be applied, such as DE/rand/1, DE/rand/2, DE/best/1, DE/best/2, DE/current-to-best/1, DE/current-to-rand/1 and other variation of them. DE/best/1, DE/best/2, DE/rand-to-best/1 and DE/current-to-best/1 are demonstrated to have fast convergence speed and very good performance; anyway, they could lead to premature convergence when tackling multimodal problems [87]. On the contrary, DE/rand/1 and DE/rand/2 have a slow convergence speed but strong exploration capability to prevent premature [87]. For this reason, in this optimization work was applied a variation of the mutation strategies, called DE/rand/1/bin.
In particular the optimization problem procedure is explained next.

5.2.1 Framework description

As aforementioned, in order to define the optimization problem it is necessary to state the objective function, the initial population, the stopping criteria and the constrains, that must be respected in order to obtain the results desired.
Since, the target is the minimization of the noise as objective function was chosen the definition of the Estimated Average OASPL, also called EAOASPL and defined as

$$EAOASPL = 10log \sum_{i=1}^{N} 10^{\frac{OASPL(i)}{10}} \tag{5.2}$$

This value is the logarithmic average of the OASPL values captured by the microphones located all around the rotor hub studied. In order to start the process is mandatory the definition of the first design parameters, that in this case of study, are defined by the values of the geometric variables: R_{TIP}, chord distribution, twist distribution, position of leading edge with respect to the x and z axis. Then, as already mentioned, for stopping the optimization procedure, the stopping criteria has to be defined; here, this role is covered by the selection of the number of iterations. Meanwhile, at each iteration the constrain of minimum thrust coefficient must be respected, in order to guarantee the hovering condition.

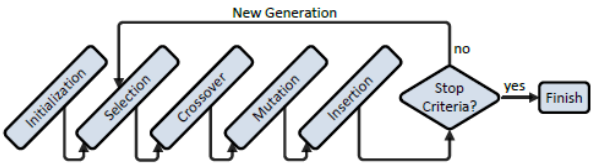

Figure 5.1: Optimization framework, from [84]

At each interaction, the design parameters of the step before are subjected to the crossover and mutation mechanisms, giving new geometric values that allow the elaboration of the EAOASPL (objective function), even respecting the upper and lower limits defined for each of these parameters, together with the constrain of C_T. Once, the maximum number of interactions is reached, the fittest blade geometry obtained is chosen as optimized blade. A more detailed description of the process followed can be found in the thesis of my colleague, Olívia Pinto, [88]. A good representations of the procedure followed is shown in figure 5.1

5.3 Optimization Results

In this section are illustrated some results obtained from the optimization run by Olívia Pinto [88] of the baseline rotor, already met in section 4.4.2. These results are compared with the noise values obtained from the initial shape of the blades, at the same atmospheric condition and rotational speed. The fittest optimized blade obtained by the application of the differential evolution algorithm to the original blade has been simulated, at the rotational speed of 4000 RPM in hover condition, in order to compare the noise SPL spectrum captured by the microphones located at $-45°$, $0°$ and $45°$ with respect to the plane of rotation, as shown in figure 5.2.

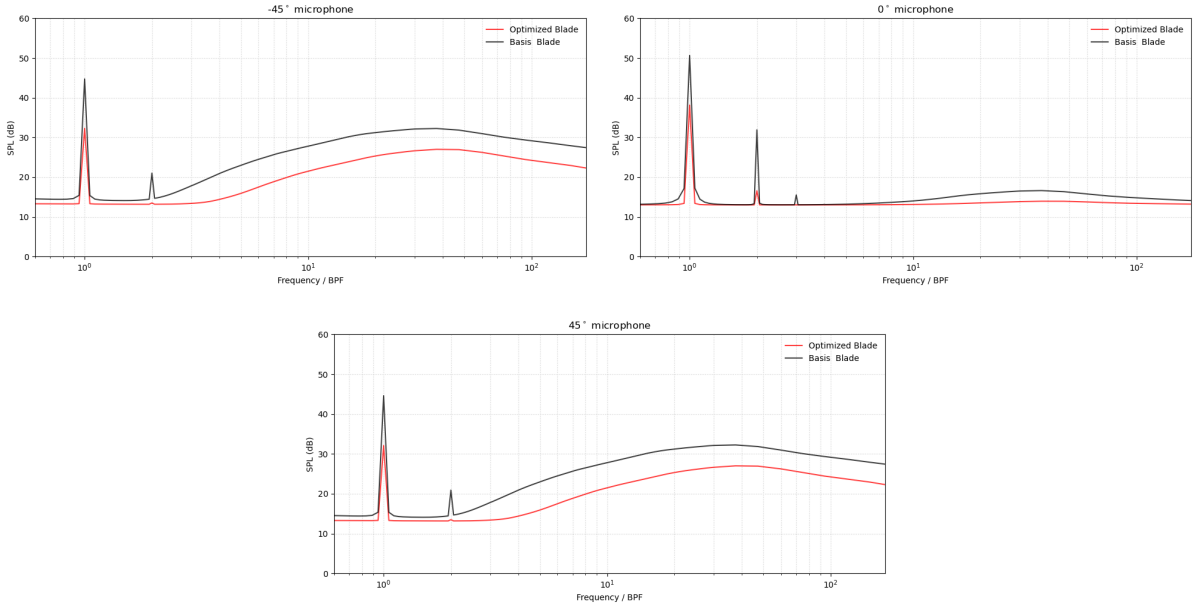

Figure 5.2: SPL spectrum comparison between original and optimized blade at $-45°$, $0°$ and $45°$ at 4000 RPM

In all the three cases taken under consideration it is possible to state that the optimized blade leads to a substantial noise reduction, especially in oblique direction ($-45°$ and $45°$), mitigating, in this way, the noise received by the hypothetical human observer located below the rotor. The optimization conducted in this project could be a good start point for the mitigation of the noise produced by the next common way of transport, the Urban Air Vehicles.

Chapter 6

Conclusions

In this chapter, a summary of what was achieved along this thesis is presented, followed by some suggestions on how to improve the noise prediction and, hence, future work.

6.1 Achievements

In the present work, the simulation engine FLOWUnsteady, developed at BYU's FLOW Lab and modified during the execution of the project, was used to predict the noise produced by the rotor of an unmanned aerial vehicle, since the size limitations of the 3D printer and wind tunnel of the Instituto Superior Técnico do not allow to test UAV rotor model, the main subject of this work. The computational values obtained from the several simulation runs at different conditions of rotational speed and with different blades model were compared with the experimental ones in order to validate the software and analyse the agreement between them. The experimental tests, cited in this work, were conducted firstly by Zawodny, used in the validation process, then by Pedro Miguel de Barros e Silva Duarte for the comparison step, collected in 2020. The single component of the vehicle was tested in a controlled acoustic environment to characterize the primary noise generation mechanisms of the rotor, removing the noise generated by the presence of the electric motor and background noise. Computational results obtained for the simulation conduced at different rotation speed and captured from different microphones, located all around the rotation plane of the rotor in static hover conditions, revealed that the code performed well at predicting the first BPF acoustic amplitudes and SPL spectrum for these hover conditions, except for an underestimation of the noise captured by the microphone located in the rotation plane of the rotor ($0°$) due to a possible underestimation of the thickness noise and the neglection of the High-Speed Impulsive noise sources; both propagating in the rotational plane. The code used is flexible, with various possible inputs and options to select for running the computation, allowing the control of the simulations in detail. The rotor studied can be re-created in this virtual space defining its geometry inputs, position settings and atmospheric conditions. Then, the hypothetical user can define the simulation conditions and run the most disparate missions obtaining the deterministic and non-deterministic noise components from PSU-WOPWOP and BPM methods, respectively. In this way, it is possible to predict with a good agree-

ment the noise pollution and optimize the blades in order to reduce it; contributing to the acceptance of the use of Urban Air Vehicle in the urban areas.

6.2 Future Work

As already mentioned in the conclusions section, even if the main subject of this thesis was the prediction of the noise produced by Urban Air Vehicles and in particular their main sources of noise, their rotors, the code was just applied to rotors of smaller size such that it is possible to compare with experimental results taken directly in the anechoic chamber of Instituto Superior Técnico. For this reason, for future work, it would be interesting the application of the code to larger rotors and compared them with experimental values correctly taken for the same models.

Moreover, as analysed in sections 2 and 3.2 a quasi-steady solver approach was applied and wings and rotors are solved through the application of VLM and BEMT, respectively; so, it was not possible to study the instability transaction, vortex breakdown and model the effects of wake interactions. A possible implementation could be the application of an unsteady solver which is able to reproduce the wake shed not as rigid and semi-infinite filaments, and is able to study the interaction effect of rotors wake on the other components of the vehicle.

Another improvement that would be interesting to see is the implementation of the dynamic simulation in the anechoic chamber of the whole structure of the UAV or a bigger vehicle in order to capture the noise produced in flight and then compare the numerical results with the experimental ones, guaranteeing the validation of the dynamic module and of the noise prediction in condition different from the hover one.

One last suggestion is to perform a test of relative movement of the observers with respect to the vehicle movement in order to analyse the capacity of the program to simulate these conditions and observe the agreement between the prediction results and real ones of noise perceived by the observers.

Bibliography

[1] Airbus. Urban air mobility: safe, sustainable and convenient. https://www.airbus.com/innovation/zero-emission/urban-air-mobility.html, Accessed on: 15 April 2021.

[2] Joint DOT-NASA Civil Aviation Research and Development Policy Study. Concept studies for future intracity air transportation systems. *Cambridge, MA: Massachusetts Institute of Technology, Flight Transportation Laboratory*, 1970.

[3] Parker D. Vascik. *Systems analysis of Urban Air Mobility Operational Scaling*. PhD thesis, MIT International Center for Air Transportation (ICAT), Department of Aeronautics & Astronautics, Massachusetts Institute of Technology, Cambridge, MA 02139 USA, Nov 2019.

[4] Viken, S. A., Brooks, F. M., and Johnson, S. C. Overview of the small aircraft transportation system project four enabling operating capabilities. *Journal of Aircraft*, 43:1602–1612, 2006. doi: 10.2514/1.20595.

[5] Editorial Team. The future of urban air mobility in europe: These companies could change the way we travel. https://siliconcanals.com/news/future-of-urban-air-mobility-in-europe/, Accessed on: 8 July 2021.

[6] Cityairbus, our four-seat evtol demonstrator. https://www.airbus.com/innovation/zero-emission/urban-air-mobility/cityairbus.html, Accessed on: 8 July 2021.

[7] Antonio J. Torija, Zhengguang Li, Rod H. Self. Effects of a hovering unmanned aerial vehicle on urban soundscapes perception. *Transportation Research*, 78(102195), January 2020. doi:10.1016/j.trd.2019.11.024.

[8] Hinnerk Eißfeldt. Sustainable urban air mobility supported with participatory noise sensing. *Department of Aviation and Space Psychology, DLR German Aerospace Center, 22335 Hamburg, Germany*, 12(8), April 2020. doi:10.3390/su12083320.

[9] EU Commission. Horizon 2020—work programme 2018–2020 part 11: Smart, green and integrated transport. https://ec.europa.eu/research/participants/data/ref/h2020/wp/2018-2020/main/h2020-wp1820-transport_en.pdf, Accessed on: 8 July 2021.

[10] G. Scalabrin, W. Negm, P. Brier, C. Bataille, F. Bonicel, N. Camara, Jean-Luc Chabaudie, C. Chouard, I. Ezquerra, A. M. Fernandez, S. Garg, V. JI, L. Labracherie, H. J. Calderon Luchini,

S. Pal, D. Pappas, M. Rodriguez, T. Taylor, D. Tortochaux, M. A. Villanueva. En-route to urban air mobility, on the fast track to viable and safe on-demand ir services. *Altran*, 2020.

[11] P. Planing and Y. Pinar. Acceptance of air taxis—a field study during the first flight of an air taxi in a european city. *OSF Preprints*, December 2019. doi:10.31219/osf.io/rqgpc.

[12] *Guidance on the Balanced Approach to Aircraft Noise Management*. International Civil Aviation Organization, `https://www.icao.int/environmental-protection/Documents/Publications/Guidance_BalancedApproach_Noise.pdf`, doc 9829 an/451 edition. Accessed on: 8 July.

[13] A. Filippone. Aircraft noise prediction. *Progress in Aerospace Sciences*, 68:27–63, March 2014. doi:10.1016/j.paerosci.2014.02.001.

[14] W. J. E. Ffowcs and D. Hawkings. *Sound Generation by Turbulence and Surfaces in Arbitrary motion*. Philosophical Transactions of the Royal Society of London, Series A, Mathematical and Physical Sciences, 264(1151) edition, 1969. doi:10.1098/rsta.1969.0031.

[15] M. J. Lighthill. *On sound generated aerodynamically - I. General theory*. Philosophical Transactions of the Royal Society of London, Series A, Mathematical and Physical Sciences, 211(1107) edition, 1951. doi:10.1098/rspa.1952.0060.

[16] JP. Raney. Development of a new computer system for aircraft noise prediction. *J Sound Vib*, 75: 536, 1975. doi:10.2514/6.1975-536.

[17] BJ. Clark. Computer program to predict aircraft noise levels. Technical Report TP-1913, NASA, 1981. Doc ID:19810025404.

[18] W. Zorumski. *Aircraft noise predictio nprogram (ANOPP) theoretical manual—Part 1*. NASA, Technical report TM-83199 edition, February 1982. Doc ID:19820012072.

[19] W. Zorumski. *Aircraft noise predictio nprogram (ANOPP) theoretical manual—Part 2*. NASA, Technical report TM-83199 edition, February 1982. Doc ID:19820012073.

[20] K. Kontos, B. Jardan and P. Gliebe. Improved nasa-anopp noise prediction computer code for advanced subsonic propulsion systems. Technical Report CR-195480, NASA, August 1996. Doc ID:19960048499.

[21] JW Hough and DS Weir. Aircraft noise prediction program (anopp) fan noise prediction for small engines. Technical Report CR-198300, NASA, 1996. Doc ID:19960042711.

[22] S.R. Liu and M.A. Marcolini. The acoustic results of a united technologies scale model helicopter rotor tested at dnw. Technical report, In: Proceedings of AHS 46th Annual Forum, Washington D.C, May 1990. doi:10.2514/6.1990-4035.

[23] F. Farassat. *Derivation of Formulation 1 and 1A Farassat*. NASA, March 2007. Doc ID:20070010579.

[24] F. Farassat. Linear acoustic formulas for calculation of rotating blade noise. *AIAA Journal*, 19(9): 1112–1130, 1996. doi:10.2514/3.60051.

[25] G. Brès, K. S. Brentner, G. Perez, and H. Jones. Maneuvering rotorcraft noise prediction. *Journal of Sound and Vibration*, 275:719–738, 2004. doi:10.1016/j.jsv.2003.07.005.

[26] S. Ianniello. Algorithm to integrate the ffowcs williams-hawkings equation on supersonic rotating domain. *AIAA Journal*, 37(9):1040–1047, 1999. doi:10.2514/2.831.

[27] K. S. Brentner, G. A. Brès, G. Perez, and H. E. Jones. Maneuvering rotorcraft noise prediction: A new code for a new problem. *Technical report, In Proceedings of AHS Aero- dynamics, Acoustics,and Test and Evaluation Technical Specialists Meeting*, January 23-25 2002. San Francisco, CA, USA.

[28] L. V. Lopes and C. L. Burley. Design of the next generation aircraft noise prediction program: Anopp2. Technical Report NF1676L-11643, NASA, Hampton, VA United States, June 2011. Doc ID:20110012482.

[29] A. Diedrich, J. Hileman, D. Tan, K. Willcox and Z. Spakovszky. Multidisciplinary design and optimization of the silent aircraft. In: 44th AIAA Aerospace sciences meeting and exhibit, January 2006. AIAA 2006-1323. doi:10.2514/6.2006-1323.

[30] J. Hileman, M. Drela, M. Sargeant and Z. Spakovszky. Airframe design for silent aircraft. In: AIAA Aerospace sciences meeting. Reno, NV, January 2007. AIAA 2007-0453. doi:10.2514/1.46545.

[31] JR.Stone, EA. Krejsa, BJ. Clark and Z. Spakovszky. Philosophy and evolution of a semi-empirical model for jet noise prediction. In: 42th AIAA Aerospace sciences meeting. Reno, NV, January 2004. AIAA 2004-0361. doi:10.2514/6.2004-361.

[32] Y. Liu, P. Anusonti-Inthra, and B. Diskin. Development and Validation of a Multidisciplinary Tool for Accurate and Efficient Rotorcraft Noise Prediction (MUTE). *NASA/CR–2011-217057*, February 2011. Hampton, Virginia.

[33] A. Filippone. Flight Performance Software FLIGHT. *AF-AERO-UNIMAN-2014-10*, January 2006. School of Mechanical, Aerospace and Civil Engineering, The University of Manchester, United Kingdom.

[34] A. Filippone. Theoretical Framework for the Simulation of Transport Aircraft Flight. *Journal of Aircraft,*, 47(5):1669–1696, September 2010. doi: 10.2514/1.C000252.

[35] U. Isermann, K. Matschat, and EA. Müller . Prediction of aircraft noise around airports by a simulation procedure. *Institute of Noise Control Engineering, Cambridge, MA*, 1(A87-27101 10-71): 717–722, July 1986.

[36] Stephen A. Rizzi, D. Douglas Boyd Jr, and Kyle Pascloni. Urban air mobility noise: Current practice, gaps, and recommendations. Technical Report TP–2020-5007433, NASA, Hampton, VA United States, October 2020. Doc ID:20205007433.

[37] Nikolas S. Zawodny, D. Douglas Jr. Boyd, and Casey L. Burley. Acoustic characterization and prediction of representative, small-scale rotary-wing unmanned aircraft system components. pages 1–2, West Palm Beach, FL, 17 May 2016. Helicopter Society (AHS) Annual Forum. DOC ID: 20160009054.

[38] K. S. Brentner and F. Farassat. Modeling aerodynamically generated sound of helicopter rotors. *Progress in Aerospace Sciences*, 39:83–120, April 2003. doi:10.1016/S0376-0421(02)00068-4.

[39] R. K. Amiet. Noise produced by turbulent flow into a propeller or helicopter rotor. *Final Report United Technologies Research Center, East Hartford, CT*, 15(3), March 1977. doi:10.2514/3.63237.

[40] Thomas F. Brooks and Casey L. Burley. Blade wake interaction noise for a main rotor. *Journal of the American Helicopter Society*, 49(1):11–27, January 2004. doi:10.4050/JAHS.49.11.

[41] Thomas F. Brooks, D. Stuart Pope, and Michael A. Marcolini. Blade wake interaction noise for a main rotor. NASA Reference Publication, NASA, Hampton, VA United States, July 1989. DOC ID: 19890016302.

[42] Thomas F. Brooks and Casey L. Burley. Rotor broadband noise prediction with comparison to model data. *Journal of the American Helicopter Society*, 49(1):28–42, January 2004. doi:10.2514/6.2001-2210.

[43] E. Alvarez and A. Ning. Development of a vortex particle code for the modeling of wake interaction in distributed propulsion. Atlanta,GA, June 2018. AIAA Applied Aerodynamics Conference. doi:10.2514/6.2018-3646.

[44] E. Alvarez, A. Schenk, T. Critchfield, and A. Ning. Rotor-on-rotor aeroacoustic interactions of multirotor in hover. *Faculty Publications*, July 2020. 4053.

[45] W. J. M. Rankine. On the mechanical principles of the action of propellers. *Transactions of the Institution of Naval Architects*, 6:13–30, 1865.

[46] F. Lanchester. A contribution to the theory of propulsion and the screw propeller. *Transactions of the Institution of Naval Architects*, 57:98–116, 1915.

[47] A. Betz. Das maximum der theoretisch möglichen ausnutzung des windes durch windmotoren. zeitschrift für das gesamte turbinenwesen. *Zeitschrift für das gesamte Turbinenwesen*, 26:307–309, 1920.

[48] N. Joukowsky. Windmill of the nej type. transactions of the central institute for aerohydrodynamics of moscow. Collected Papers VI:405–409 1937, The Joukowsky Institute for AeroHydrodynamics, Moscow, 1920.

[49] N. Joukowsky. Windmill of the NEJ type. Joukowsky NE. Collected Papers VI:405–409 1937, The Joukowsky Institute for AeroHydrodynamics, Moscow, 1937.

[50] G. A. M. Van Kuik. The lanchester-betz-joukowsky limit. *Wind Energy*, 10(3):289–291, 2007. doi:10.1002/we.218.

[51] H. Glauert. *The Elements of Aerofoil and Airscrew Theory*. Cambridge University Press, 1983. doi:10.1017/CBO9780511574481.

[52] Bertin, John J. and Cummings, Russell M. *Aerodynamics for Engineers*. Pearson Education International, 6^{th} edition, 2021. doi:10.1017/9781009105842.

[53] Christopher C. Hennes, Leonard V. Lopes, Justin Shirey, Rui Cheng, James Erwin, Seongkyu Lee, Benjamin A. Goldman, Mrunali Botre, Damaris R. Zachos, Ze Feng (Ted) Gan, Robert Rau, Eric Greenwood, and Kenneth S. Brentner. *PSU-WOPWOP 3.4.4 User's Guide*. The Pennsylvania State University, January 2021.

[54] A. E. A. Vieira. Helicopter rotor noise: Development of an acoustic software tool. Master thesis, Instituto Superior Técnico, November 2013.

[55] M. R. R. Dias. Aeroacoustical module development for the novemor mdo software. Master thesis, Instituto Superior Técnico, July 2017.

[56] J. W. Cooley and J. W. Tukey. An algorithm for the machine calculation of complex fourier series. *Mathematics of Computation*, 19(90):297–301, April 1965. doi:10.1090/S0025-5718-1965-0178586-1.

[57] J. Hammond and K. Shin. Fundamentals of signal processing for sound and vibration engineers. *Wiley*, February 2008. ISBN 978-0-470-51188-6.

[58] K. S. Brentner. Numerical algorithms for acoustic integrals with examples for rotor noise prediction. *AIAA Journal*, 35(a):625–630, April 1997. doi:10.2514/2.182.

[59] B. A. Goldman. Modifications to psu-wopwop for enhanced noise prediction capabilities. Master thesis, The Pennsylvania State University, May 2013.

[60] P. Bortolotti, E. Branlard, A. Platt, P. J. Moriarty, C. Sucameli, and C. L. Bottasso. Aeroacoustics noise model of openfast. Nrel/tp-5000-75731, NREL, Golden, CO: National Renewable Energy Laboratory, August 2020. doi:10.2172/1660130.

[61] Brooks, Thomas F., Pope, D. Stuart and Marcolini, Michael A. Airfoil self-noise and prediction. Nasa reference publication 1218, NASA, National Aeronautics and Space Administration, USA, July 1989. Doc ID:19890016302.

[62] L. Clark. Faculty profile: Mark drela's research and his teaching. *AeroAstro*, pages 41–46, April 2005-2006. The Massachusetts Institute of Technology Department of Aeronautics and Astronautics.

[63] Du, Z., and Selig, M. A 3-d stall-delay model for horizontal axis wind turbine performance prediction. *ASME Wind Energy Symposium, American Institute of Aeronautics and Astronautics, Reston, Virigina*, 1998. doi:10.2514/6.1998-21.

[64] Viterna, L. A., and Janetzke, D. C. Theoretical and experimental power from large horizontal-axis wind turbines. *Washington Procurement Operations Office, Washington, DC (United States)*, September 1998. doi:10.2172/6763041.

[65] Eduardo Alvarez, and Andrew Ning. High-fidelity modeling of multirotor aerodynamic interactions for aircraft design. Technical report, Brigham Young University, Provo, Utah, 84602, 2020.

[66] Eduardo J. Alvarez. Quasi-steady aerodynamics solver for a high-fidelity controls framework. Technical report, Brigham Young University, Provo, Utah, 84602, 2020.

[67] A. Gibiansky. Quadcopter dynamics and simulation. `https://andrew.gibiansky.com/blog/physics/quadcopter-dynamics/`, Accessed on: 8 July 2012.

[68] H. Lee and D.-J. Lee. Rotor interactional effects on aerodynamic and noise characteristics of a small multirotor unmanned aerial vehicles. *Physics of Fluids 32*, April 2020. doi:10.1063/5.0003992.

[69] D. Shukla and N. Komerath. Multirotor drone aerodynamic interaction investigation. *School of Aerospace Engineering, Georgia Institute of Technology, Atlanta, GA 30332, USA*, November 2018. doi:10.3390/drones2040043.

[70] *NI 6353 Device Specifications*. National Instruments, `https://www.ni.com/pdf/manuals/374592d.pdf`, 2016. Accessed on: 25 October 2021.

[71] *NI CB-68LP/CB-68LPR User Guide*. National Instruments, `ni.com/pdf/manuals/373853a.pdf`, 2013. Accessed on: 25 October 2021.

[72] *Model 482C15 Four-Channel, ICP Sensor Signal Conditioner Installation and Operating Manual*. PCB Piezotronics, `https://www.pcb.com/contentStore/docs/pcb_corporate/electronics/products/manuals/482c15.pdf`, 2017. Accessed on: 25 October 2021.

[73] V. Intertechnology. Reflective optical sensor with transistor output. `https://www.vishay.com/docs/83751/cny70.pdf`, Accessed on: 19 September 2021.

[74] Current and voltage sensor specifications. `https://www.pitlab.com/fpv-system/current-sensor.html`, Accessed on: 19 September 2021.

[75] Current transducer ltsr 25-np. `http://docs-europe.electrocomponents.com/webdocs/06c4/0900766b806c43de.pdf`, Accessed on: 19 September 2021.

[76] N. S. Corporation. Lm35 precision centigrade temperature sensors. `https://www.engineersgarage.com/sites/default/files/LM35.PDF`, Accessed on: 19 September 2021.

[77] *Brüel & Kjær 20 kHz Precision Array Microphone — Type 4958*. Product Manual Data, https://www.bksv.com/-/media/literature/Product-Data/bp2173.ashx, 2011. Accessed on: 25 October 2021.

[78] F.Pereira. Development and testing of an acoustic measurement system for the ist aeroacoustic wind tunnel. Master thesis, Instituto Superior Técnico, November 2017.

[79] R. Oshana. *DSP Software Development Techniques for Embedded and Real-Time Systems*. Elsevier Ltd, Online edition, 2006. doi:10.1016/B978-0-7506-7759-2.X5000-5.

[80] *Brüel & Kjær Sound Calibrator Type-4231*. Product Manual Data, https://www.bksv.com/media/doc/bp1311.pdf, 2021. Accessed on: 25 October 2021.

[81] P. M. de Barros and S. Duarte. Novel concepts for noise mitigation of small uav rotors. Master thesis, Instituto Superior Técnico, October 2020.

[82] Zawodny, N. S., and Boyd, Jr., D. D. Acoustic characterization and prediction of representative, small-scale rotary-wing unmanned aircraft system components. *72nd American Helicopter Society (AHS) Annual Forum*, 2016.

[83] J. Nocedal. *Numerical Optimization*. Springer Nature, 2^{nd} edition, 2006. doi:10.1007/978-0-387-40065-5.

[84] S. S. Rodrigues. Aeroacoustic optimization of wind turbine blades. Master thesis, Instituto Superior Técnico, November 2012.

[85] N. Rodríguez, A. Gupta, P. L. Zabala, and G. Cabrera-Guerrero. Optimization algorithms combining (meta)heuristics and mathematical programming and its application in engineering. *Mathematical Problems in Engineering*, 2018, August 2018. doi:10.1155/2018/3967457.

[86] Yang, G., Reinstein L.E., Pai S., Xu Z., and Carroll D.L. A new genetic algorithm technique in optimization of permanent 125-i prostate implants. *Medical Physics*, 25(12):2308–2315, December 1998. doi:10.1118/1.598460.

[87] L. Cui, G. Li, Q. Lin, J. Chen, and N. Lu. Adaptive differential evolution algorithm with novel mutation strategies in multiple sub-populations. *Computers & Operations Research*, 67:155–173, 2016. doi:10.1016/j.cor.2015.09.006.

[88] O. Pinto. On rotor noise optimization for urban air mobility. Master thesis, Instituto Superior Técnico, November 2021.

Appendix A

Scale of 1/3 Octave Bands

Number of the band	f^{lower}	f^{higher}
1	14,1	17,8
2	17,8	22,4
3	22,4	28,2
4	28,2	35,5
5	35,5	44,7
6	44,7	56,2
7	56,2	70,8
8	70,8	89,1
9	89,1	112,0
10	112,0	141,0
11	141,0	178,0
12	178,0	224,0
13	224,0	282,0
14	282,0	355,0
15	355,0	447,0
16	447,0	562,0
17	562,0	708,0
18	708,0	891,0
19	891,0	1122,0
20	1122,0	1413,0
21	1413,0	1778,0
22	1778,0	2239,0
23	2239,0	2818,0
24	2818,0	3548,0
25	3548,0	4467,0
26	4467,0	5623,0
27	5623,0	7079,0
28	7079,0	8913,0
29	8913,0	11220,0
30	11220,0	14130,0
31	14130,0	17780,0
32	17780,0	22390,0

Appendix B

Procedure for using the Signal Conditioner

The signal conditioners used in the experiment were first checked in order to guarantee their trustworthiness. Thank to the collaboration of the professor Agostinho Fonseca , both signal conditioners available were tested, using an oscilloscope, a signal generator and just one microphone. The scope of this instrument is getting the voltage signal from the microphone and sending an amplified one to the DAQ board. The signal conditioner used (model PCB Piezotronics 482C15 sensor ICP), have two amplifying modes: the ICP mode and the Voltage mode. In order to amplify the signal of the microphones was chosen the ICP mode. Moreover, there are three different signal gains available: X1, X10 and X100. For the proposed experiment, the gain was set to X100, that is recommended for the microphones because this value makes the signal easier and cleaner to be read in the LabVIEW program.

B.1 The Signal Conditioner Signal

The signal transmitted by the signal conditioners was verified for the four channels of both of them. The voltage signal transmitted has two components, a continuous one and an alternating one, where this latter is the one transmitted by the microphones. The objective is to amplify only the alternating component and neglect the continuous one. When the signal conditioner is powered on there is a voltage overflow, and the oscilloscope could only read the continuous component, with no signal from the alternating one. Using the gains value of x100 this overflow reaches voltages up to $\pm 20V$. Waiting 1 minute and 12 seconds of powering the signal conditioner, the oscilloscope was able to read the microphones signal; however, the continuous component was still the dominant one. Then, after 2 minutes and 30 seconds, the continuous component was fluctuating up to $\pm 1V$. This continuous component is lower than $\pm 0.1V$ only after 5 minutes, and finally the alternating signal was clearly bigger than the other one. In short, to use the signal conditioner, the user needs to wait 5 minutes before taking measurements. In order to prevent any possible experimental error it was waited at least 10 minutes after powering on the signal conditioner.

Appendix C

Microphone at -45°

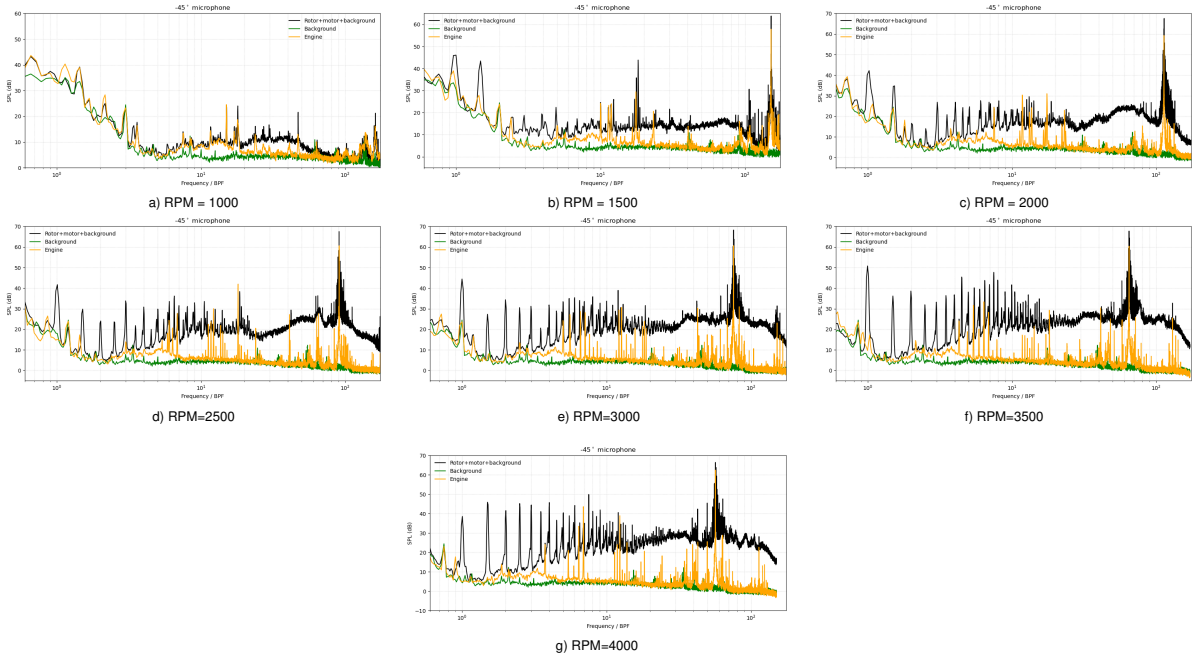

a) RPM = 1000 b) RPM = 1500 c) RPM = 2000

d) RPM=2500 e) RPM=3000 f) RPM=3500

g) RPM=4000

Figure C.1: Whole structure, motor and background SPL spectrum at $-45°$ at $1000, 1500, 2000, 2500, 3000, 3500,$ and 4000 RPM

C.1 Difference between whole structure and motor at -45°

C.2 Comparison between numerical and experimental values at -45°

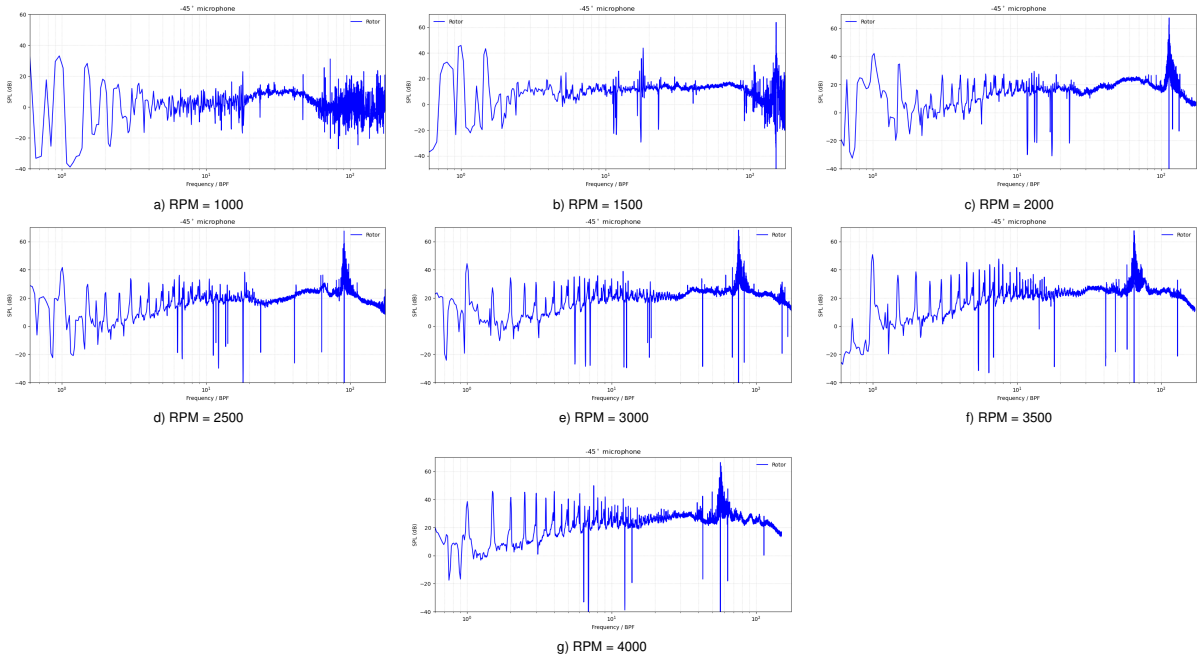

a) RPM = 1000 b) RPM = 1500 c) RPM = 2000

d) RPM = 2500 e) RPM = 3000 f) RPM = 3500

g) RPM = 4000

Figure C.2: Difference between whole structure and motor SPL spectrum at $-45°$ at $1000, 1500, 2000, 2500, 3000, 3500,$ and 4000 RPM

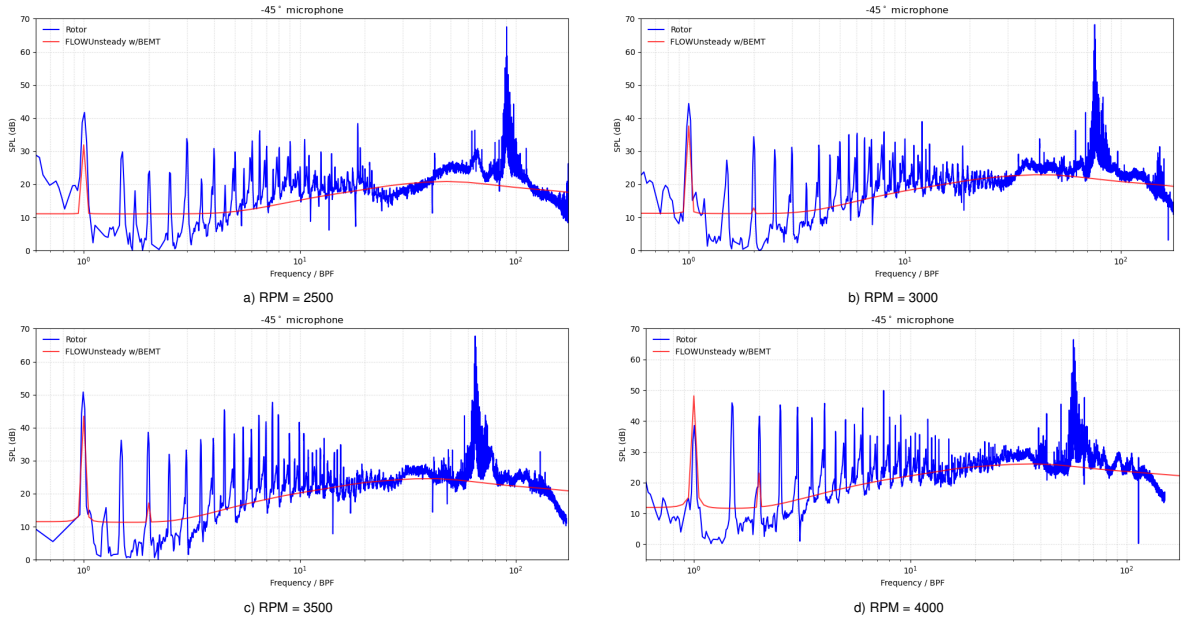

a) RPM = 2500 b) RPM = 3000

c) RPM = 3500 d) RPM = 4000

Figure C.3: SPL spectrum comparison between FLOWUnsteady and experimental values at $-45°$ at $2500, 3000, 3500,$ and 4000 RPM

Appendix D

Microphone at 0°

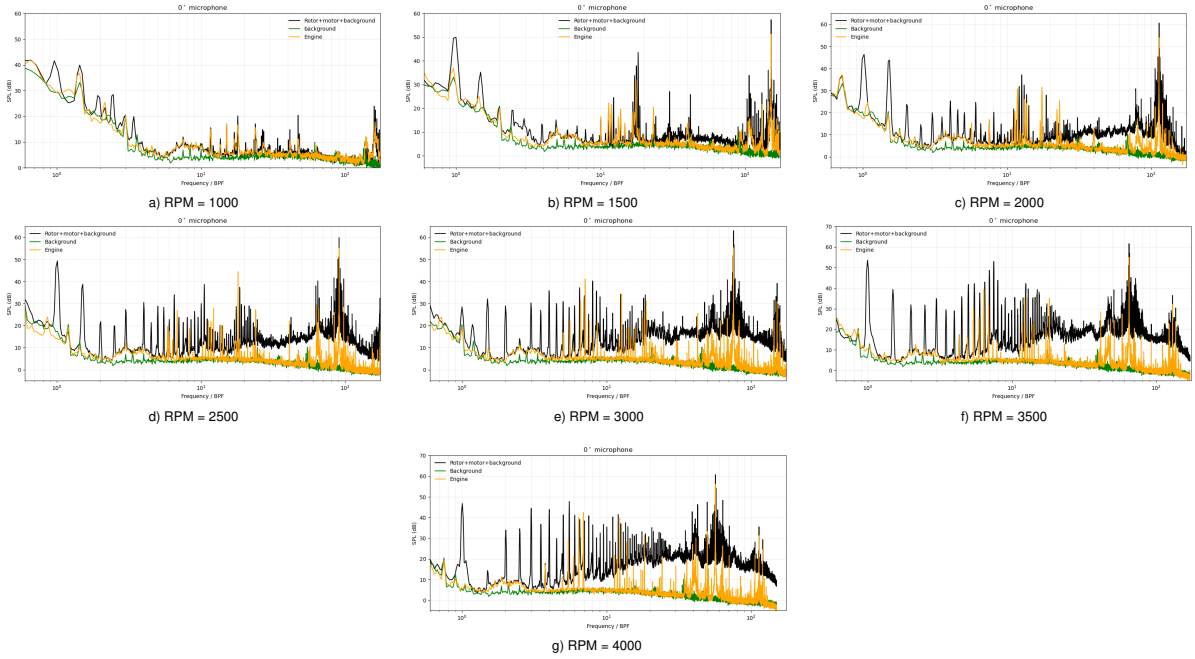

a) RPM = 1000 b) RPM = 1500 c) RPM = 2000

d) RPM = 2500 e) RPM = 3000 f) RPM = 3500

g) RPM = 4000

Figure D.1: Whole structure, motor and background SPL spectrum at $0°$ at $1000, 1500, 2000, 2500, 3000, 3500,$ and 4000 RPM

D.1 Difference between whole structure and motor at 0°

D.2 Comparison between numerical and experimental values at 0°

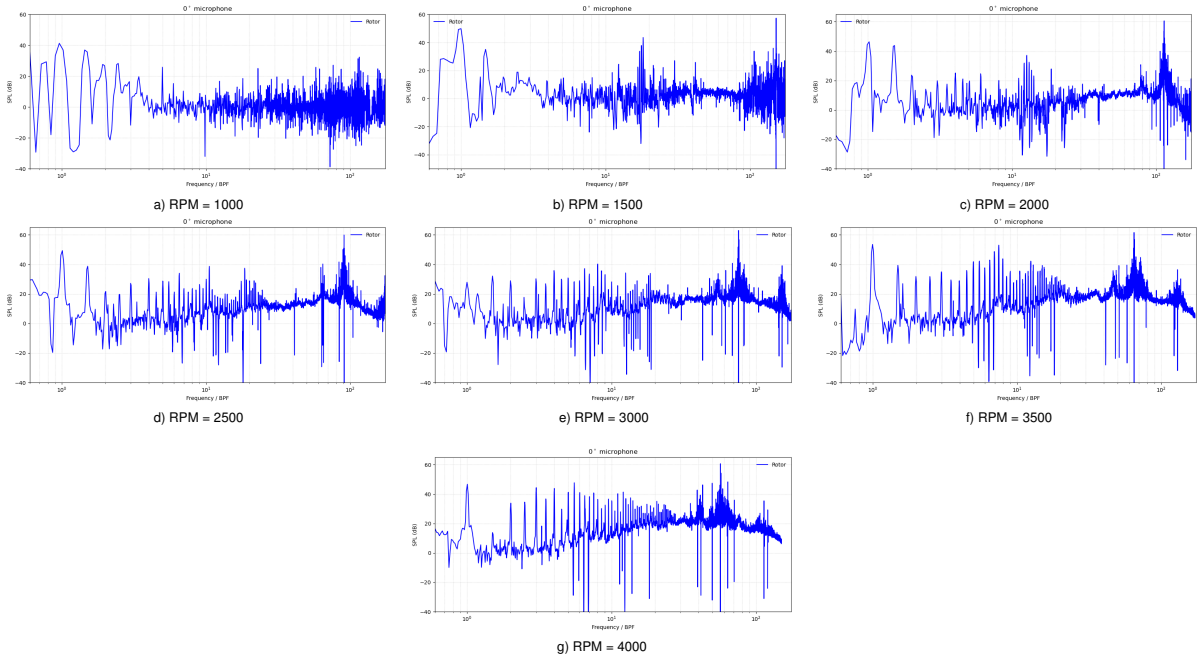

a) RPM = 1000 b) RPM = 1500 c) RPM = 2000

d) RPM = 2500 e) RPM = 3000 f) RPM = 3500

g) RPM = 4000

Figure D.2: Difference between whole structure and motor SPL spectrum at $0°$ at $1000, 1500, 2000, 2500, 3000, 3500,$ and 4000 RPM

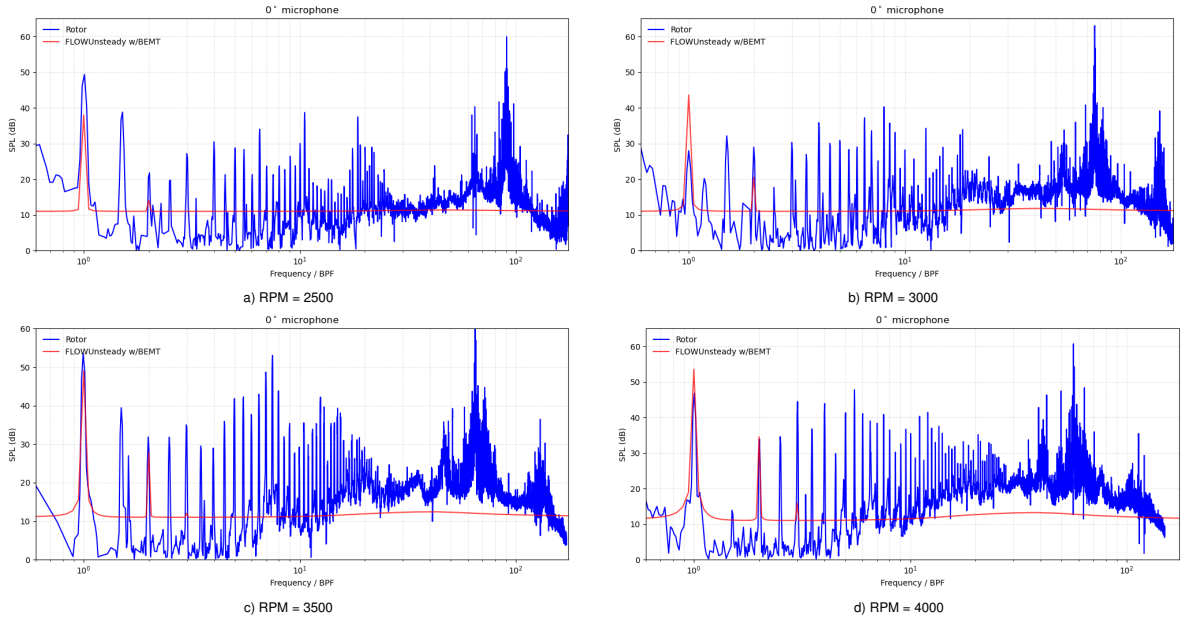

a) RPM = 2500 b) RPM = 3000

c) RPM = 3500 d) RPM = 4000

Figure D.3: SPL spectrum comparison between FLOWUnsteady and experimental values at $0°$ at $2500, 3000, 3500,$ and 4000 RPM

Appendix E

Microphone at 45°

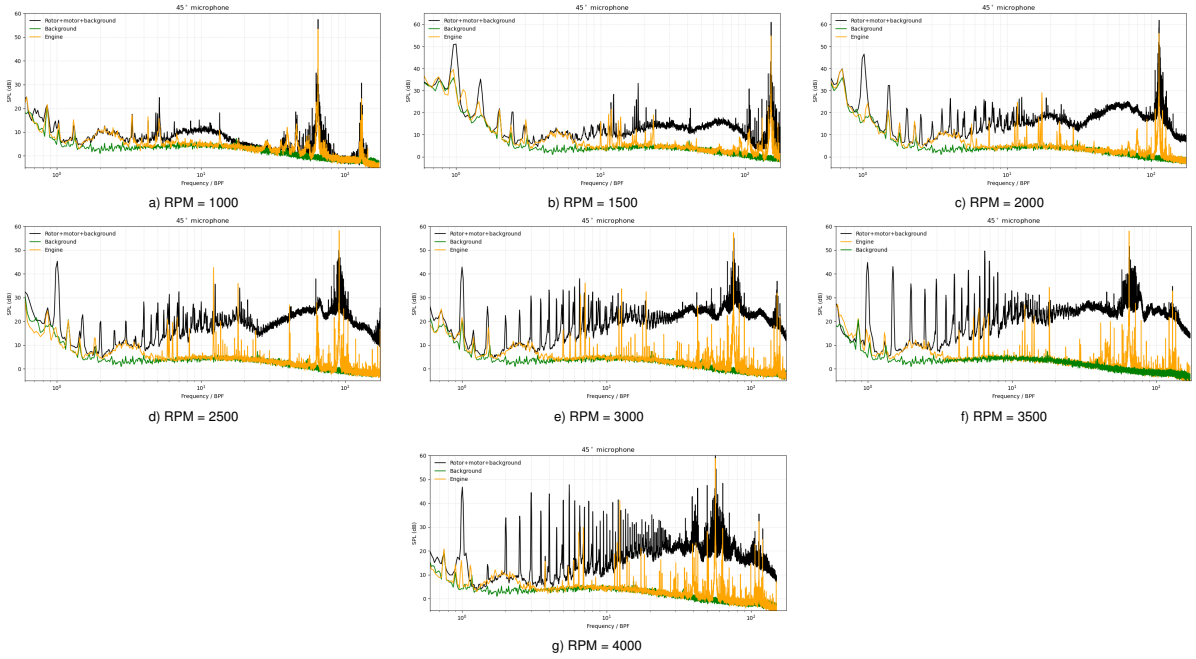

a) RPM = 1000 b) RPM = 1500 c) RPM = 2000

d) RPM = 2500 e) RPM = 3000 f) RPM = 3500

g) RPM = 4000

Figure E.1: Whole structure, motor and background SPL spectrum at $45°$ at $1000, 1500, 2000, 2500, 3000, 3500,$ and 4000 RPM

E.1 Difference between whole structure and motor at 45°

E.2 Comparison between numerical and experimental values at 45°

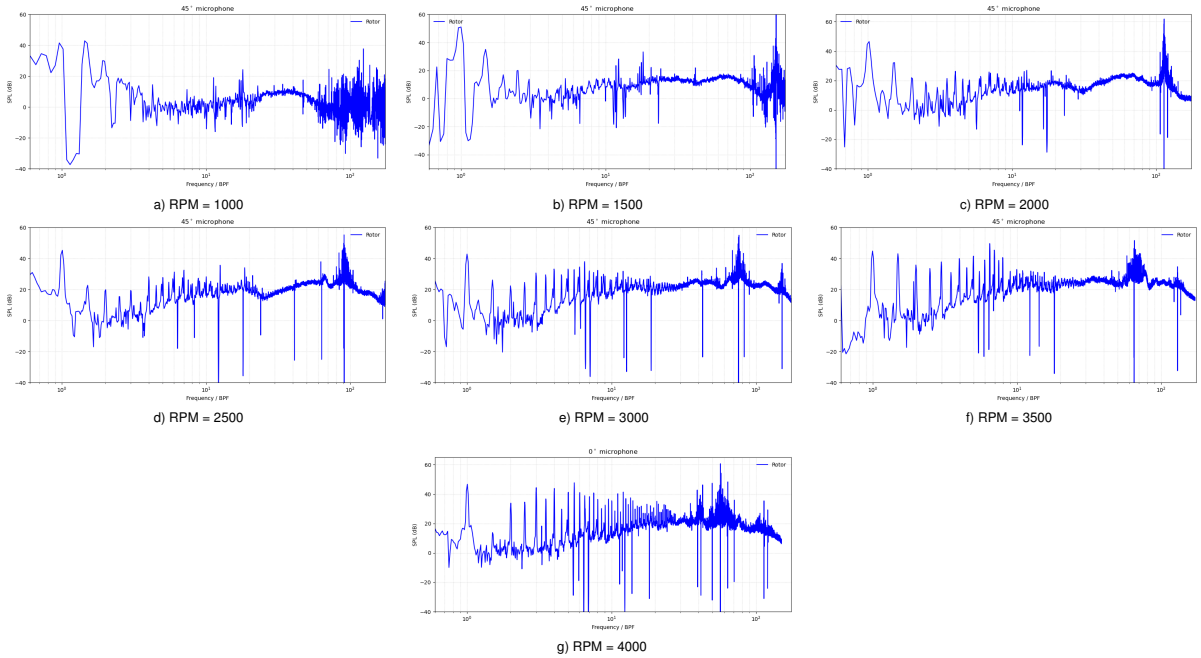

Figure E.2: Difference between whole structure and motor SPL spectrum at $45°$ at $1000, 1500, 2000, 2500, 3000, 3500,$ and 4000 RPM

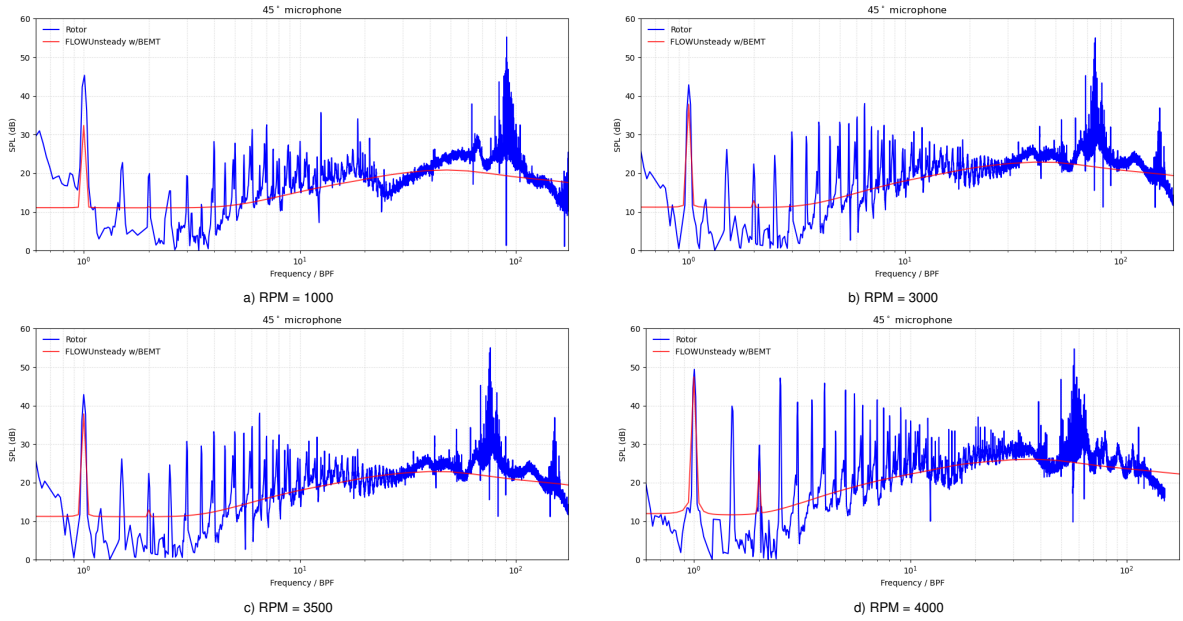

Figure E.3: SPL spectrum comparison between FLOWUnsteady and experimental values at $45°$ at $2500, 3000, 3500,$ and 4000 RPM